Aqueous OH^-/H^+ Dual-ion Gradient Energy Assisted Electrochemical Energy Storage and Conversion Devices

A Thesis Submitted in Partial Fulfilment of the Requirements for the Degree of

Doctor of Philosophy

By

Mr. Soumodip Sur

(ID: 20152029)

Department of Chemistry

Indian Institute of Science Education and Research

Pune, India – 411008

Indian Institute of Science Education and Research (IISER),

Pune – 411 008

Dr. Musthafa O. T

Associate Professor

Chemistry Division and Centre for Energy Science

Date 30/12/2022

CERTIFICATE

This is to certify that this thesis entitled "**Aqueous OH^-/H^+ Dual-ion Gradient Energy Assisted Electrochemical Energy Storage and Conversion Devices**" towards the partial fulfilment of Ph.D. programme at Indian Institute of Science Education and Research, Pune represents original research carried out by **Mr. Soumodip Sur** at Indian Institute of Science Education and Research, Pune under the supervision of **Prof. Muhammed Musthafa O.T.**, Associate Professor, Department of Chemistry and Centre for Energy Science, IISER Pune during the academic years 2017-2022 and that no part of it has been included in any other thesis submitted previously for the award of any degree.

Signature of Thesis Supervisor

Dr. Muhammed Musthafa O.T.

Associate Professor,

Department of Chemistry and Centre for Energy Science,

IISER Pune

Indian Institute of Science Education and Research (IISER),
Pune – 411 008

Date 30/12/2022

DECLARATION

I hereby declare that the matter embodied in the thesis entitled "**Aqueous OH^-/H^+ Dual-ion Gradient Energy Assisted Electrochemical Energy Storage and Conversion Devices**" are the results of the investigation carried out by me at the Department of Chemistry and centre for Energy Science of the Indian Institute of Science Education and Research, Pune under the supervision of **Prof. Muhammed Musthafa O.T.**, Associate Professor, Department of Chemistry and Centre for Energy Science, IISER Pune during the academic years 2017-2022 and that no part of it has been included in any other thesis submitted previously for the award of any degree.

Soumodip Sur

Signature of the Student
Soumodip Sur
Reg no. 20152029
IISER Pune

Dedicated to my beloved Parents

ACKNOWLEDGEMENT

Before commencing my thesis, I would like to thank everybody who have helped me in the journey of my PhD directly or indirectly.

First of all, I want to express my deepest gratitude to my supervisor Dr. Muhammed Musthafa O.T. for providing constant support and motivation throughout the last five years. I have learnt a lot from him.

I would like to express my sincere gratitude to my research advisory committee (RAC) members, Dr. P.A. Joy (N.C.L. Pune) and Dr. Partha Hazra (IISER Pune) for their valuable suggestions during the RAC meetings every year during my PhD. Their insightful suggestions have immensely aided in improving the quality of this thesis.

I would like to thank all the faculty members of chemistry department for mentoring me during my coursework in M.S. Their teaching provided me the knowledge and skills which helped me to successfully complete my research work.

I want to deeply acknowledge my current labmates namely Neethu, Sanchayita, Ritwik, Rahul, Muskan, Shifali, Bhojkumar and Suhail who have provided me a healthy lab atmosphere. Their supportive and caring behaviour made my journey easier and enjoyable. I would also like to express my gratitude towards my senior lab members namely Dr. Mruthyunjayachari. C. D, Dr. Alagar Raja Kottaichamy, Dr. Manu Gautam and Dr. Zahid Manzoor Bhat from whom I learnt a lot about various electrochemical techniques and instruments. I also want to thank the project students like Pramod, Swapnil, Deepraj. Digvijay and Abdul with whom I have worked for short periods during my PhD tenure and have learned a lot of things.

I also want to thank the non-teaching staffs of chemistry department, Mahesh, Sandeep, Anil, Yatish, Sandeep (NMR) for providing me instrumental facility whenever I needed.

Last but not the least, I want to thank my parents and family members who always helped me enormously during my PhD journey.

Soumodip Sur

Table of Contents

Synopsis of the thesis entitled "**Aqueous OH^-/H^+ Dual-ion Gradient Energy Assisted Electrochemical Energy Storage and Conversion Devices**"

The aim of this thesis is to directly utilize the hidden electromotive force available with the OH^-/H^+ dual-ion gradients to improve the performance of state-of-the-art electrochemical energy storage and conversion devices. Towards this, a two compartment electrochemical cell was constructed, by decoupling the direct acid alkali chemistry by a proton conducting membrane (Nafion117). This electrochemical cell is named as OH^-/H^+ dual-ion electrolyte cell. This thesis is divided majorly into two parts. **Part I** explores, how this OH^-/H^+ dual-ion gradient energy can be utilized to increase the energy density of energy storage and conversion devices like aqueous supercapacitors by expanding the voltage window from 1.23 V to nearly 2 V. **Part II** deals with the energy conversion devices like electrolytic cells, wherein the OH^-/H^+ dual-ion gradient energy is employed to reduce the required input potential in electrodesalination, photo electrochemical water splitting and electro-organic synthesis. The thesis encompasses the following chapters:

Chapter 1. This Chapter provides justification for the exploration of alternative and renewable energy resources in the context of paramount pollution and global climate change. Nevertheless, a complete shifting to a carbon neutral energy chain is challenged by the temporal and geographic fluctuations of renewables. This demand electrochemical energy storage and conversion devices to bridge the gap between the peak of energy availability and the peak of energy demand. However, the performance of electrochemical energy devices is often limited by their threshold energy storage capability, available voltage window, possibilities of parasitic chemistry, electricity ineffective electrolysis etc. To address these classical challenges, we have employed a two compartment electrochemical device by decoupling the direct acid alkali chemistry by a proton conducting membrane. This OH^-/H^+ dual-ion gradient has a hidden electromotive force of 0.82 V under standard

conditions; however, its non-redox nature completely prevents its direct interconversion as electrical driving force. In the working Chapters to follow, we demonstrate how the performance metrics of state-of-the art-energy storage and conversion devices can be remarkably improved by harvesting the hidden electromotive force available with OH^-/H^+ dual-ion gradients.

Part I

Chapter 2. This Chapter deals with the classical challenge of improving the energy density of electrochemical rcapacitors without compromising their power capability by utilizing the hidden electromotive force available with OH^-/H^+ dual-ion gradients. Since the energy of an electrochemical capacitor is quadratically related to the

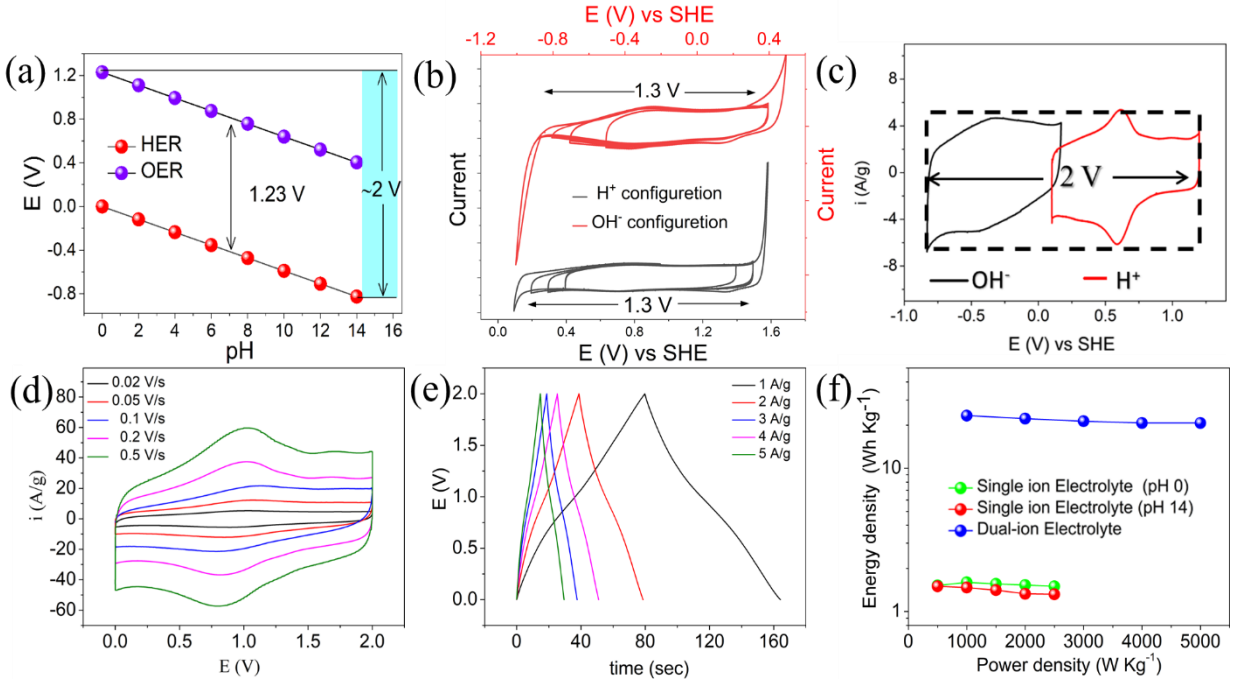

Figure 1: (a) The Pourbaix diagram for the water splitting half-cell reactions, (b) cyclic voltammograms of carbon material in H^+ and OH^- single ion configuration. (c) Combined cyclic voltammograms of the carbon electrodes in H^+ and OH^- single ion configurations. (d) Cyclic voltammetry and (e) charge discharge curves in two electrode configurations when H^+ and OH^- ions are decoupled by a Nafion 117

membrane. (f) Ragone plots for activated carbon electrode in OH^-/H^+ dual-ion and H^+ and OH^- single ion configurations.

working voltage window, the most beneficial strategy to boost the energy density is to target the operating voltage window. However, expanding the voltage window beyond 1.23 V in aqueous systems is thermodynamically challenged due to parasitic water splitting reaction. We show that the parasitic chemistry can be arrested by decoupling the direct acid-alkali chemistry by employing the hidden electromotive force in OH^-/H^+ dual-ion gradient electrolyte, and consequently, the voltage window in aqueous supercapacitors can be expanded to 2 V while boosting the energy density up to ~230% (Figure 1).

Part II

Chapter 3. This Chapter deals with the integrating bifunctional functionality in a single electrochemical device by harvesting the hidden electromorive force available with OH^-/H^+ dual-ion gradients.

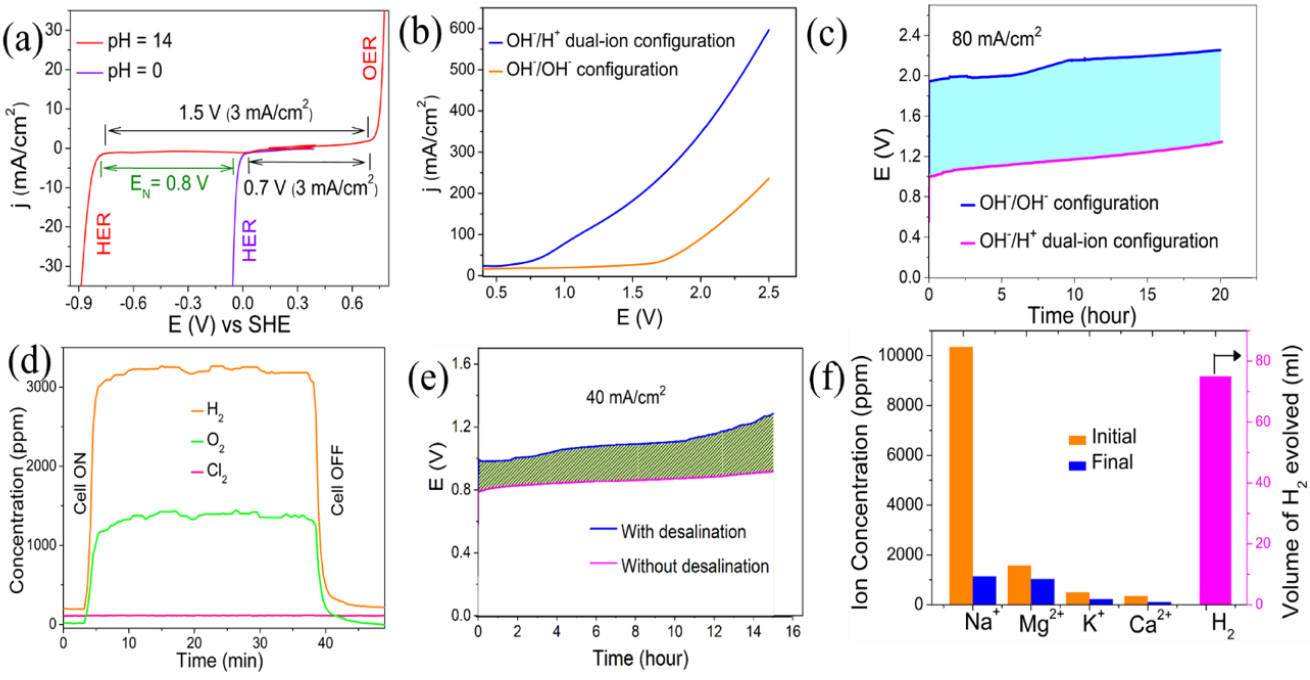

Figure 2 (a) Hydrogen evolution reaction (HER) in pH = 0 and pH = 14 electrolytes and oxygen evolution reaction (OER) in pH = 14 electrolyte. (b) Current–voltage (I–V) curves for the OH^-/H^+ dual-ion

and OH^-/OH^- single ion water electrolyzers. (c) Chronopotentiometry of OH^-/H^+ dual-ion and OH^-/OH^- single ion water electrolyzer at 80 mA/cm^2 for 20 hours, (b) in-situ electrochemical mass spectrometry of cathodic and anodic species of OH^-/H^+ dual-ion water electrolyzer at 80 mA/cm^2 and (e) chronopotentiometry of the device with and without the saline middle compartment. (f) Na^+, Mg^{2+}, K^+, and Ca^{2+} ion concentrations obtained from MP-AES analysis along with the amount of H_2 released after 6 h when the middle compartment of the OH OH^-/H^+ dual-ion cell housed seawater from Arabian Sea.

With OH^-/H^+ dual ion gradient electrolytic cell, an electrochemical device capable for simultaneous electro desalination and H_2 generation in an electricity-effective manner is demonstrated. The OH^-/H^+ dual ion gradient electrolytic cell at a current density of 40 mA/cm^2 performs electrodesalination with minimal parasitic chemistry while generating ~33 ml/h of H_2 at a terminal voltage of ~1 V, which is only half of the voltage required in a symmetric single ion configuration. Contrary to conventional desalination process, the low-voltage electrodesalination in OH^-/H^+ dual ion gradient electrolytic cell noticeably improves the energy efficiency and prevents competitive parasitic chemistry.

Chapter 4. This Chapter discusses electricity effective photoelectrochemical (PEC) water splitting to store the solar energy in the chemical bonds of molecular hydrogen. Among several photo electrodes used for PEC water splitting, α-Fe_2O_3 is a promising material due to its suitable bandgap, chemical stability, and abundance. Despite these, the position of its conduction band does not allow spontaneous movement of photo-generated electrons to cause the water reduction. In single-ion configuration, this demands the application of a minimum electrical bias of ~1.5 V vs. SHE to increase the energy of the conduction band such that it will be energetically above the H_2O/H_2 redox level. By utilizing the the hidden electromotive force available with OH^-/H^+ dual-ion gradients, the minimum electrical voltage

required for PEC water splitting can be brought down to ~0.8 V. OH^-/H^+ dual-ion assisted PEC water splitting required only 0.95 V to produce a current density of 10 mA/cm^2, and for achieving the same current density in a conventional symmetric ion configuration requires at least a doubling of the applied electrical bias (~1.8 V).

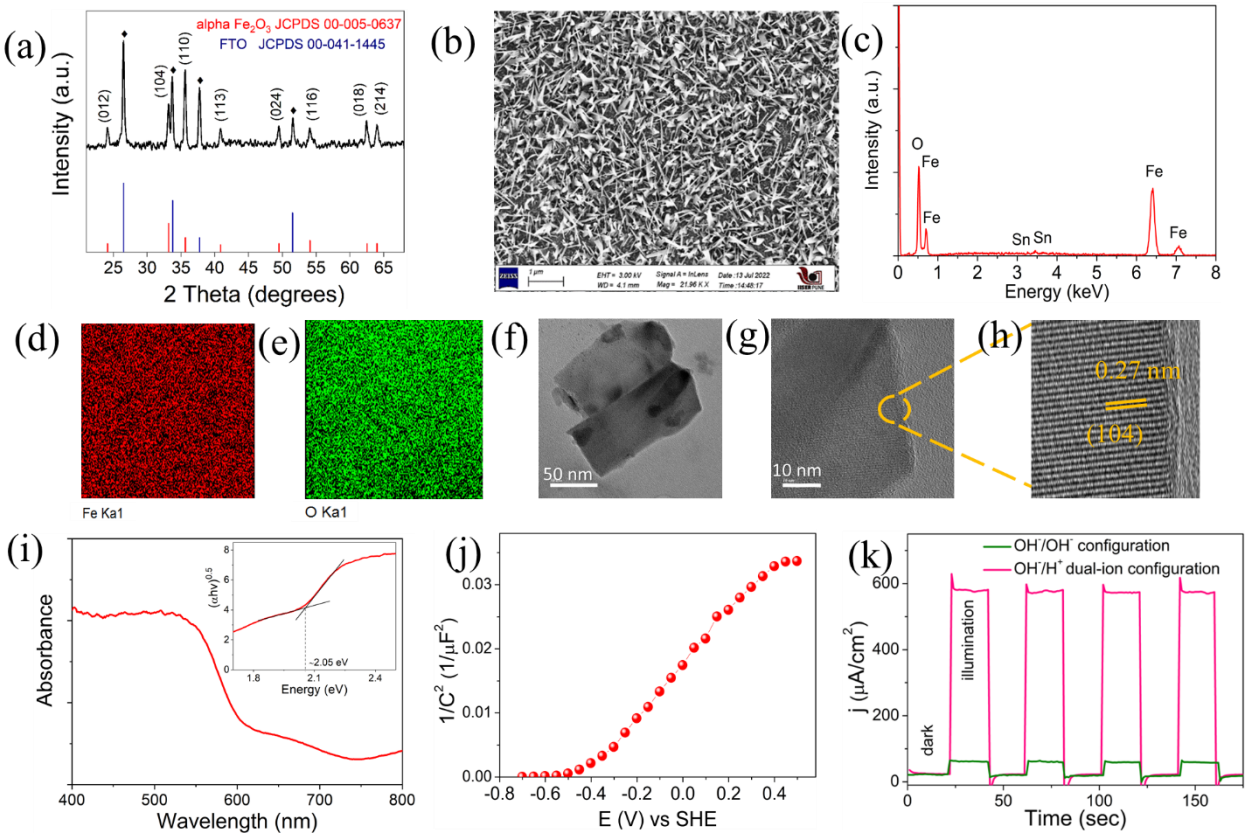

Figure 3 (a) X-Ray diffraction (XRD) of as-prepared α-Fe_2O_3 on FTO. (b) Scanning electron microscopy (SEM) image and (c) energy dispersive spectroscopy (EDS) of as prepared α-Fe_2O_3. (d) and (e) corresponds to elemental mapping of iron (Fe) and oxygen (O). (f) Transmission electron microscopy (TEM) image of α-Fe_2O_3. (g) and (h) corresponds to high resolution TEM (HRTEM) images. (i) Solid state UV-Vis spectroscopy of as prepared α-Fe_2O_3 on FTO and Tauc plots for showing the indirect bandgap. (j) Mott-Schottky plots of α-Fe_2O_3 electrode obtained in 0.1 M NaOH electrolyte at 5 kHz AC frequency with a 10 mV AC amplitude (peak to peak). (k) Transient

photo-response in OH^-/H^+ dual-ion and OH^-/OH^- single ion configurations at 0.75 V.

Chapter 5. This Chapter shows how the hidden electromotive force of 0.82 V available with OH^-/H^+ dual-ion gradient cell can be directly harvested as electrical driving force for performing simultaneous electro-organic synthesis and hydrogen fuel production in an electricity effective manner. To demonstrate this dual-ion gradient assisted electro-organic synthesis, 5-hydroxymethylfurfural (HMF) is chosen as the model molecule because of the immense techno commercial applications of its oxidized products. This dual-ion assisted device only required ~1 V to provide a current density of 50 mA/cm^2 and for achieving the same rate; the traditional state-of-the-art electrolytic cell required a doubling of the applied potential. The dual-ion gradient assisted device can convert biomass-derived HMF to economically important FDCA with ~90 % yield and ~87 % Faradaic efficiency with simultaneous H_2 fuel production at a potential as low as 1 V.

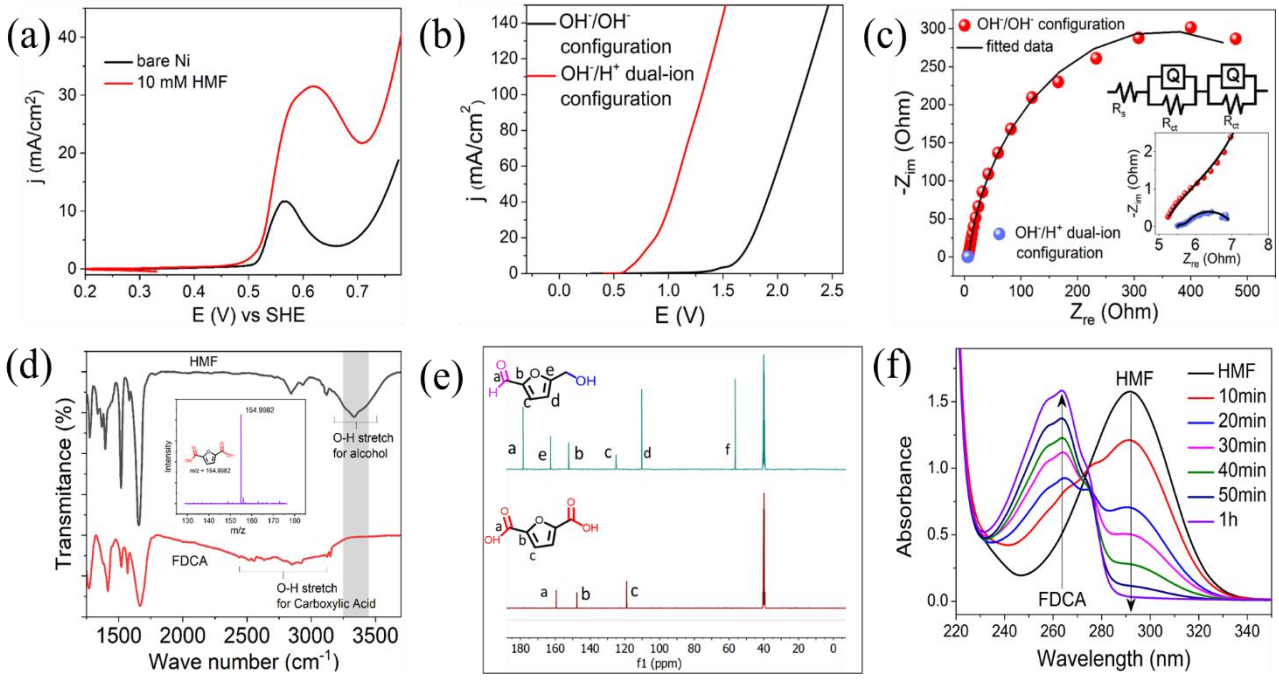

Figure 4 (a) Linear sweep voltammogram (LSV) of a Ni foam electrode in pH 14 solution with and without HMF (10 mM) at 5 mV/s

scan rate. (b) Current-Voltage curves for the OH^-/H^+ dual-ion configuration and OH^-/OH^- symmetrical configurations. (c) Impedance spectra of symmetric cell and asymmetric cell at 1 V of applied potential in the AC frequency range of 100 kHz to 10 mHz with an AC excitation of 10 mV. Inset contain the equivalent circuit and zoomed high frequency region. (d) FTIR spectra of reactant (HMF) and product (FDCA). (b) ^{13}C NMR spectra of the anolyte before and after one hour of electro-organic synthesis. (e) Ex-situ UV-vis spectra of the anolyte with regular time interval during continuous electro-organic synthesis.

Chapter 6. This Chapter provides a summary and a road map for future directions.

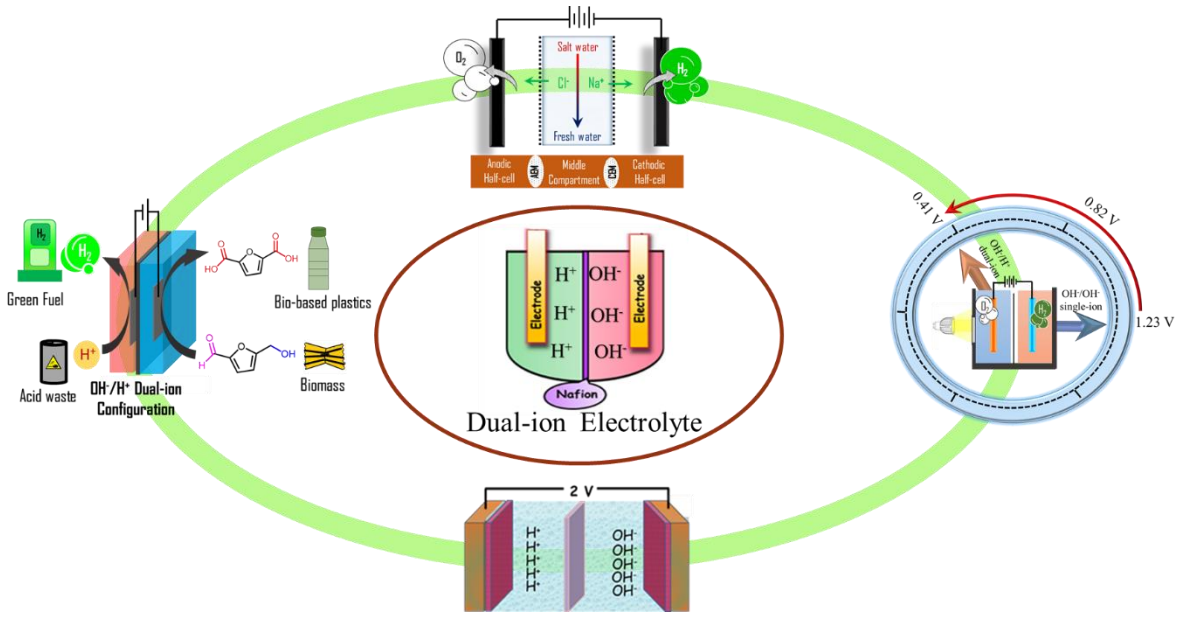

Figure 5 OH^-/H^+ dual-ion gradient energy in deferent electrochemical energy storage and conversion devices.

Chapter 1

Introduction

Abstract

The substantial increase in demands of energy for the social order trigger the exploitation of different renewable energy resources for energy conversion and storage. However, renewables exhibit temporal and geographic fluctuations which demand electrochemical energy storage and conversion devices to bridge the gap between the peak of energy availability and the peak of energy demand. Notwithstanding, the performance of electrochemical energy devices is often limited by their threshold energy storage capability, voltage window, parasitic chemistry, electricity ineffective electrolysis etc. Towards this direction, the major aim of this thesis is to demonstrate how the OH^-/H^+ dual-ion gradient energy can be utilized in electrochemical devices to introduce novel functionalities as well as to significantly improve their performance. To fulfill these targets, an electrochemical neutralization device is constructed by decoupling the direct acid-alkali chemistry by an ion conducting membrane. In the remaining Chapters to follow, it will be shown that, by harvesting the hidden electromotive force in OH^-/H^+ dual-ion gradient electrolyte, the voltage output of galvanic cells can be enhanced and the voltage input of electrolytic devices can be significantly decreased.

1.1 World energy scenario

The world's population is expected to increase by 2 billion in the next 30 years; from 7.7 billion currently to 9.7 billion in 2050. [1-3] Due to this exponential rising of population and industrial growth, the energy demand around the globe is also increasing concomitantly. According to the U.S. energy information administration (EIA), world energy consumption will increase from ~20 TW (2021) to ~30 TW in 2050, i.e. it will rise by 50% and a large amount of that energy is catered by fossil fuels such as coal, oil and natural gas etc.[4]

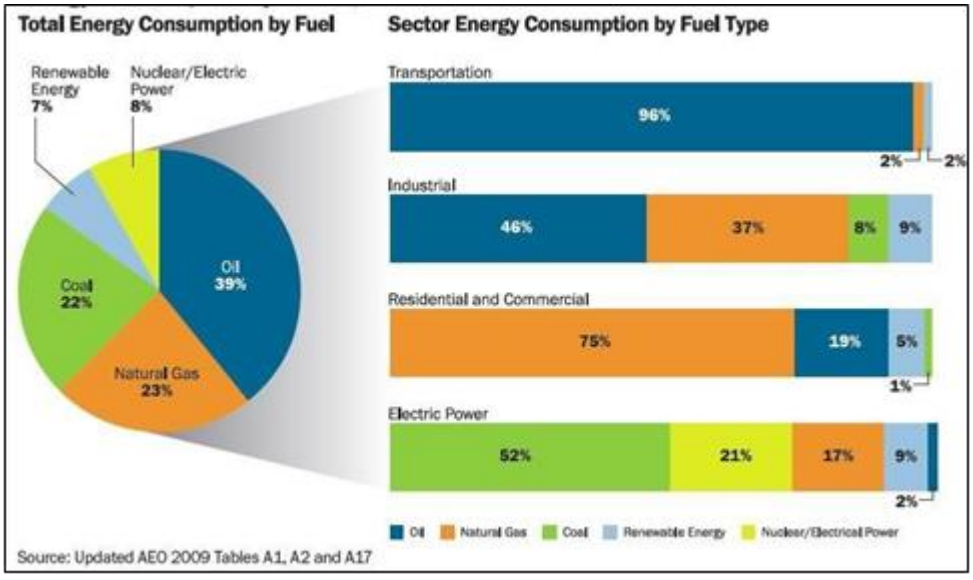

Figure1.1 Energy consumption percentage in different sectors. (Source: https://www.bitlanders.com/blogs /comparison-of-energy-sources-with-our-daily-uses).

As of 2016, 79.5% of total energy consumed was from conventional energy resources such as coal, petroleum oil and natural gas whereas the rest (20.5%) came from renewable energy resources including

hydropower, wind, biopower and solar photovoltaics.[5-6] However, these latter resources of energy have got seasonal and geographical variations which demand their storage at the time of availability and conversion at the time of demand.

1.2 Non-renewable Energy

Non-renewable energy sources cannot be replenished after use and eventually will be consumed in the long run. Carbon based fuels like coal, oil, natural gas etc., are the main examples of non-renewable energy resources. Energy is generated by combusting of those carbon based fuels in the presence of air. In that process, carbon dioxide (CO_2) is produced which is detrimental to the environment. The amount of CO_2 produced is dependent upon the amount the carbon present in the fuel and the atmosphere where the fuel is burned. Typically, the amount of carbon content varies from fuel to fuel and 99 % of carbon in a fuel is converted to CO_2 after burning.[7-8] Very less amount of fuel is converted to other hydrocarbons and carbon monoxide which are eventually converted to CO_2 in the atmosphere. Generation of the more greenhouse gases like CO_2 is a threat to the environment as they are involved in rising of global mean temperature.[9-10] Several studies have reported that the glacier is melting which will eventually increase the sea levels all over the world, due to which several coastal regions of our planet will disappear. Apart from this, the huge demand for alternative fuel is due to the limiting storage of this carbon based fuel in earth as it was speculated that recent fossil fuels reservoir can only

support up to 40 years for petroleum, 60 years for natural gas and 156 years for coal.[11-12] Therefore, finding out an alternating source of energy is the need of the hour for a sustainable world.

Figure 1.2 Renewable vs non-renewable resources.
(Source:https://www.picemaps.com/ images-of-non- renewable-resources/)

1.3 Renewable Energy

Due to these unaffordable drawbacks and limitations of fossil fuels, we need to pay attention to other flawless natural resources like solar energy, wind energy, biomass energy, geothermal energy etc., to meet our requirements without compromising the environment. However, it will be challenging in terms of exploitation at the modest cost. The overview of various renewable sources along with their pros and cons is briefly described here.

(a) Solar energy: According to the US Department of Energy, planet earth is receiving 430 quintillion Joules of energy in each hour from the

Sun, which is more than the entire world population consuming in a year.[13-14] But, developing strategic materials, which can harvest that huge energy is a classical challenge.

(b) Wind energy: In 2021 alone, wind supplied over 1800 TWh of electricity, which was over 6% of world's electricity consumption and about 2% of world's energy consumption. It is considered as one of the pillars of future energy sources. However, the installations of turbine and maintenance are formidable tasks.[15]

(c) Biomass energy: Biomass is plant-based materials used as fuels to produce heat or electricity.These are inexpensive and easily producible renewable energy sources. But, in order to produce 10 TW electric power, we need to cover 10% of earth's surface with switch grass.[16]

(d) Hydroelectric energy: It is one of the oldest and largest resources of renewable energy, where energy of moving water flow is converted to electricity. However, it has relatively low power capacity.

(e) Tidal energy: This energy is generated due to periodic tide of oceans. Although, it is a clean and an innovative energy source, it has a low potential.

In spite of several advantages, renewable energy sources have its own limitations. The main limitation is that renewable energy is not available round the clock. They have strong dependence on weather fluctuations. For example, sunlight is an impeccable source of energy with ample potential. However, the intermittent nature of Sun has

raised the concern of its compatibility with electricity network. There are two types of variations associated with solar energy: daily variation (day and night cycle) and second is seasonal variation (when Sun is not intense in winter and in wet season). Therefore, it is difficult to cope up with our need in the off cycle time via electricity conversion route.

In case of wind energy, the kinetic energy of the wind is converted into electricity or mechanical power. But like solar energy, wind supply is very much dependant on weather fluctuations. The exact availability and speed of wind is not predictable and therefore it is unreliable. The foregoing discussion highlight the need for efficient electrochemical energy storage and conversion modules to bridge the gap between the peak of energy availability and the peak of energy demand.

1.5. Types of Electrochemical Energy Devices

The major electrochemical energy storage technologies are batteries and supercapacitors, Figure 1.3. There are also attempts to store the energy in the chemical bonds of fuel molecules like hydrogen and hydrocarbons, however they belong to energy conversion technologies. Fuel cells, water electrolysers, solar cells, electro-organic synthesis etc., are the major electrochemical energy conversion pathways (Figure 1.3). These devices play important roles in the sustainable energy landscape as these can bridge the existing gap between energy availability and energy demand.

Generally, these electrochemical energy devices offer high efficiency with low pollution to the environment and are also flexible with their construction. The electrode and electrolyte architectural components of these devices are integral for efficient energy storage and conversion. Electrodes are primarily responsible for electron transfer whereas electrolytes mainly act as a medium and host for redox couples and ion transport. Based on their energy and power capabilities, these devices have been classified as shown in the Ragone plot, Figure 1.4.

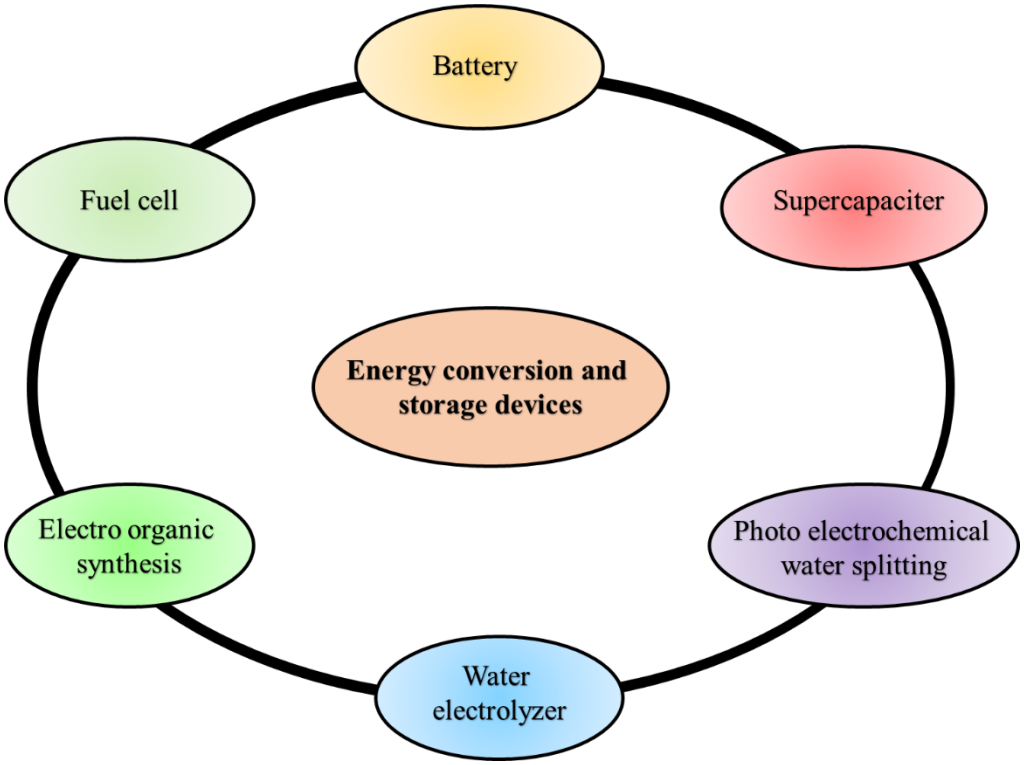

Figure 1.3 Types of electrochemical energy devices.

From the Ragone plot, it is clear that supercapacitors have higher power density whereas fuel cell, batteries possesses higher energy density. However, there are situations which demand high energy and high

power requirements and that can be accomplished by combining a device with high power with another device with high energy. The energy and power densities are the important parameters to define the output performance of any electrochemical device.

1.5.1. Supercapacitors

Supercapacitors are electrochemical device that store the charge in electrode electrolyte interface, and it release that store charge whenever it is required. it consists of electrode, electrolyte and separator. when a supercapacitor is connected with external power source then charge will store in electrode electrolyte interface and after that when it connected with external load, then it releases that charge in the out circuit.[17-18] Figure 1.5. Generally, supercapacitor possess high power density but low energy density. There are generally two type of supercapacitor one is electrochemical double layer supercapacitor (EDLC) and another is pseudocapacitor.

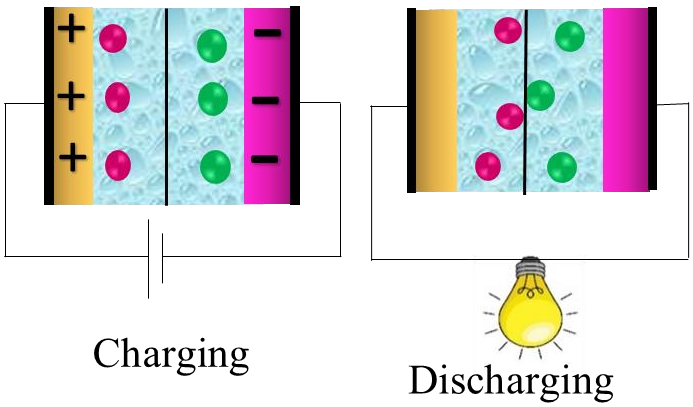

Figure 1.5 Schematic representation of components of a supercapacitor.

1.5.1.1. Electrochemical Double layer capacitors (EDLCs)

These types of supercapacitors store the charge via non-Faradaic process in the electrochemical double layer. Charging and discharging of these EDLCs are based on the ion adsorption and desorption on electrodes surface, Figure 1.6(a). These devices generally possess higher rate capability and longer number of cycles without encountering phase transitions. Nano carbon materials possessing high surface area like Ketjen black, Vulcan carbon, carbon nano tubes (CNTs), graphene etc., are classical examples for EDLC electrodes.[19-20]

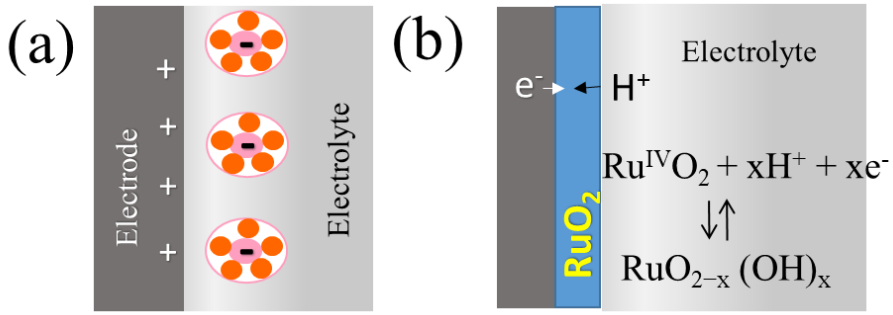

Figure 1.6 Schematic representation of (a) Electrochemical Double layer capacitors (EDLCs) and (b) Pseudocapaciter.

1.5.1.2 Pseudocapacitors

Unlike EDLCs, it stores the charge via a reversible surface confined Faradaic process along with the charge storage in the electrochemical double layer, Figure 1.6(b). Pseudocapacitor follow both Faradaic and non-Faradaic processes. The pseudocapacitors have higher capacitance than EDLCs, however they generally have lower rate capability and

shorter life cycles. Transition metal oxides like RuO_2, IrO_2 etc., are typical examples for pseudocapacitive materials. [21-22]

1.5.2. Batteries

A battery is an electrochemical energy storage device (Figure 1.7), which store electrical energy in the form of chemical energy during the charge process and its interconversion during the discharge process. The distinction between supercapacitor and battery originates mainly from the charge storage mechanism, it is mainly surface confined in the former as opposed to the bulk storage in the latter. [23-24]

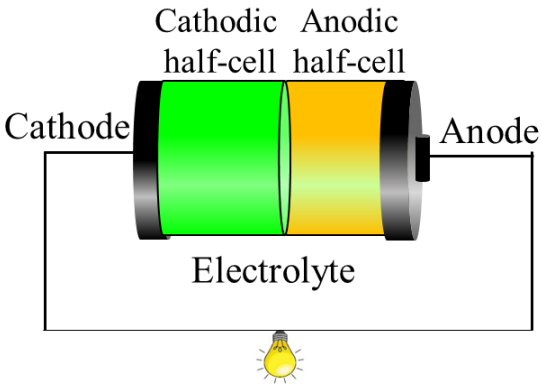

Figure 1.7 Schematic representation of components of Battery.

As secondary batteries are rechargeable, the cells convert chemical energy to electrical energy during the discharge chemistry and the process will be reversed during the charge chemistry. The cells consist of cathode and anode immersed in aqueous or non-aqueous electrolytes, Figure 1.7. Typically, the charge is stored in the bulk of electrode instead of on the surface of the electrode as in supercapacitors. In the case of primary batteries only discharge chemistry is possible and charge chemistry under practical

circumstances is hindered. However, in secondary batteries, the chemical reaction can be reversed by applying an external electrical bias. Major primary batteries are zinc carbon battery and Daniel cells and major secondary batteries are Li-ion battery and Pb-acid battery. [25-26]

1.5.3. Fuel Cells

Fuel cells are electrochemical energy conversion devices that convert chemical energy into electricity. Typically, a proton exchange membrane fuel cell (PEMFC) converts the chemical energy of H_2 and O_2 into electricity, Figure 1.5. As shown in equations 1.1, H_2 enters the anodic compartment gets ionized and the electrons released travel through external circuit to the cathode where it combines with O_2 and hydrogen ion travelling through proton exchange membrane forming water as shown in equation 1.2.[27-28] State of the art PEMFC uses Pt based electrocatalysts to drive the reactions.

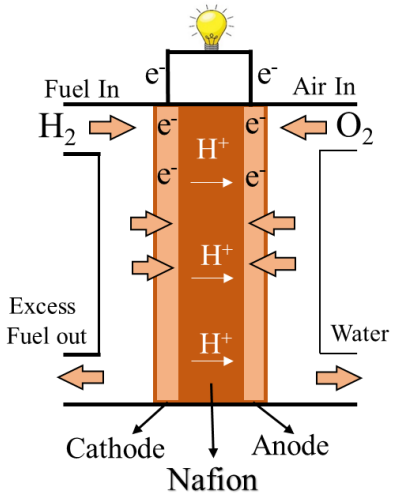

Figure1.8 Schematic representation of components of a PEM Fuel Cell.

At anode: $H_2 \rightarrow 2H^+ + 2e^-$ ($E^0 = 0$ V vs. SHE) ...1.1

At cathode: $\frac{1}{2} O_2 + 2H^+ + 2e^- \rightarrow H_2O$ ($E^0 = 1.23$ V vs. SHE) …1.2

Along with PMFC, there are several type of fuel cells, which are summarise in Table 1.

Fuel Cell types	Anode Reaction	Cathode Reaction	Operating Temperature	Mobile Ion
Proton exchange membrane (PEM) fuel cell	$H_2 \rightarrow 2H^+ + 2e^-$	$1/2O_2 + 2H^+ + 2e^- \rightarrow H_2O$	75	H^+
Direct methanol fuel cell (DMFC)	$CH_3OH + H_2 \rightarrow CO_2 + 6H^+ + 6e^-$	$1/2O_2 + 2H^+ + 2e^- \rightarrow H_2O$	75	H^+
Alkaline fuel cell (AFC)	$H_2 + OH^- \rightarrow 2H_2O + 2e^-$	$1/2O_2 + 2H_2O + 2e^- \rightarrow 2OH^-$	80	OH^-
Phosphoric acid fuel cell (PAFC)	$H_2 \rightarrow 2H^+ + 2e^-$	$1/2O_2 + 2H^+ + 2e^- \rightarrow H_2O$	200	H^+
Solid oxide fuel cell (SOFC)	$H_2 + O^{2-} \rightarrow H_2O + 2e^-$	$1/2O_2 + 2e^- \rightarrow O^{2-}$	800-1000	O^{2-}

1.5.4. Electro-organic synthesis

Electro-organic synthesis is an emerging electrolytic technology where electricity is used as an oxidizing or reducing agent for energy conversion. This technology has several advantages over traditional organic reactions. For example, it requires no reducing reagent or oxidizing agent; thereby, minimal chemical waste occurs, which leads to high atomic efficiency. Moreover, electricity is relatively affordable compared to reducing or oxidizing reagents. A zero carbon footprint can be achieved when electricity originates from renewable energy sources, which makes the organic reaction pathway highly sustainable.[29-31]

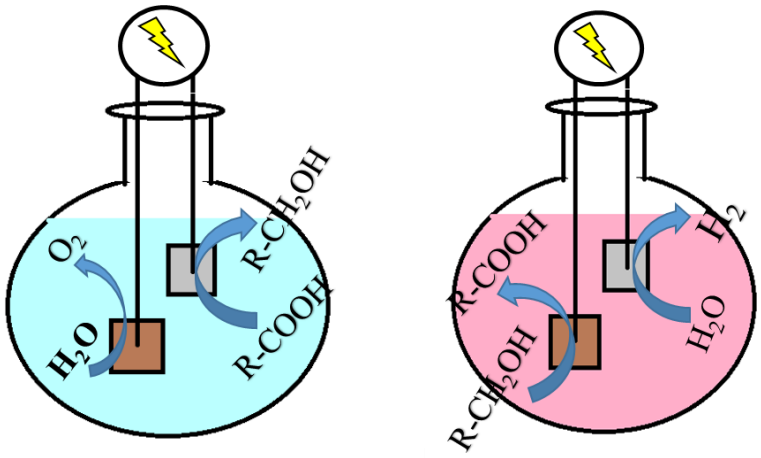

Figure 1.9 Schematic representations of electro-organic oxidation and reduction reactions.

1.5.5. Water electrolyzer and electrodialysis

In water electrolyzer electricity is used to split the water into pure hydrogen and oxygen. Electrochemical water splitting consists of the two half reactions of hydrogen evolution reaction (HER) and oxygen evolution reaction (OER). Overall reaction involves water splitting as shown in equation

$$H_2O \rightarrow 2H_2 + O_2 \quad \ldots.1.3$$

Water splitting can be in either acidic or alkaline medium where acid or alkali is used as catalyst.

In acidic medium the half-cell reactions are

At cathode $2H^+ + e^- \rightarrow H_2$ $E^0 = 0.0$ V ….1.4

At anode $2H_2O \rightarrow O_2 + 4H^+ + 4e^-$ $E^0 = 1.23$ V ….1.5

In alkaline medium the half-cell reactions are

At cathode $2H_2O + 2e^- \rightarrow H_2 + 2OH^-$ $E^0 = -0.8$ V ….1.6

At anode $4OH^- \rightarrow O_2 + 2H_2O + 4e^-$ $E^0 = 4.1$ V ….1.7

The overall electrode potential required for water splitting is in acidic medium

$E^0 = E^0_{cathode} - E^0_{anode}$

$E^0 = 0$ V $- 1.23$ V

$E^0 = -1.23$ V

In alkaline medium

$E^0 = E^0_{cathode} - E^0_{anode}$

$E^0 = 0$ V $- 1.23$ V

$E^0 = -1.23$ V

The energy can be calculated into the standard cell voltage with the following equation:

$$\Delta G^0 = - nFE^0 \qquad \ldots\ldots 1.8$$

$$\Delta G^0 = - 4*96500*(-1.23)$$

$$= 286 \text{ kJ/mol}$$

where E^0 is the standard cell voltage and n is the number of electrons, F is the Faradays constant and ΔG^0 is the standard Gibbs free energy required to carry out the reaction. Equation 1.1 is a thermodynamically uphill reaction and it needs energy of 286 kJ/mol to carry out the reaction at room temperature and pressure. The total enthalpy change for water splitting is ΔH^0 = 286 kJ/mol whereas Gibbs free energy is ΔG^0 = 237 kJ/mol respectively.[32-34] Based on this free energy change, the total voltage which is required to carry out the overall water splitting is 1.23 V, whereas, the overall required thermo-neutral voltage

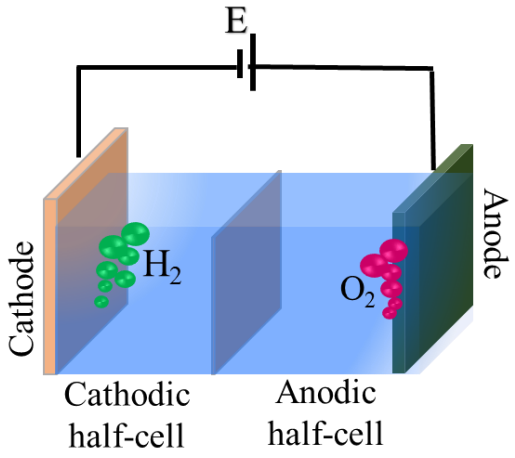

Figure 1.10 Schematic representation of components of a water electrolyzer.

Based on enthalpy change corresponds to 1.48 V.[35-36] It is observed that it is quite challenging to carry out the reaction at the theoretical voltage and maximum efficient water splitting occurred in the potential range much beyond 1.48 V. For the overall water splitting, oxidation half reaction of OER is the bottleneck reaction which involves the transfer of four electrons to produce one molecule of O_2. The reduction half reaction of HER involves two electrons to produce one molecule of H_2.

Desalination is an energy-demanding process commonly powered by nonconventional energy sources which are unsustainable. Electro-desalination is the process of removing salts or other minerals and contaminants from seawater, brackish water, and wastewater effluent by the use of electricity and it is an increasingly common solution to obtain fresh water for human consumption and for domestic/industrial utilization. Renewable energy sources (RES) such as solar, wind, and geothermal sources can serve as alternative energy sources for desalination processes.

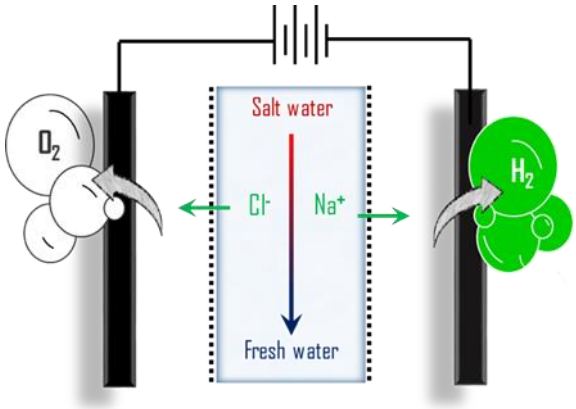

Figure 1.12 Schematic representation of components of an Electro desalination.

1.5.6. Photoelectrochemical (PEC) water splitting

Due to similarity of working mechanism of photoelectrochemical (PEC) water splitting with photosynthesis, it is also known as artificial photosynthesis. In 1972, Fujishima and Honda demonstrated the photoelectrolysis of water for first time with TiO_2 electrode.[40] In principle when a semiconductor (typically n-type) photo electrode immersed in an electrolyte is illuminated with light, then electron and hole pairs are generated and get separated due to presence of internal electric field. Electrons from the conduction band are drifted towards the counter electrode where they involve in the reduction half-cell of counter water reduction reaction. The holes in the valence band participate in the oxidation half-cell reaction at the semiconductor electrolyte interface to produce O_2 gas, (Figure 1.11). In acidic medium, the redox half reactions of water can be written as follows:

$$2H^+ + 2e^- \rightarrow H_2 \qquad E^0 = 0.0\ V \qquad \text{.....1.9}$$

$$2H_2O + 4h^+ \rightarrow 4H^+ + O_2 \qquad E^0 = -1.23\ V \qquad \text{....1.10}$$

For alkaline medium, the reduction and oxidation half reactions can be written as follows:

$$4h^+ + 4OH^-(aq) \rightarrow O_2(g) + 2H_2O \qquad E^0 = -0.828\ V \qquad \text{....1.11}$$

$$2H_2O(aq) + e^- \rightarrow H_2(g) + 2OH^-(aq) \qquad E^0 = -0.401\ V \qquad \text{....1.12}$$

The complete water splitting reaction can be written as:

$$2H_2O \rightarrow 2H_2 + O_2 \qquad \text{....1.13}$$

Water splitting requires a voltage supply of 1.23 V, which corresponds to a Gibb's free energy of +237 kJ/mol. For a semiconductor to be used as a photoelectrode, water redox levels should lie between band edges of the semiconductor. If not its alignment by band engineering or applied will be required to shift the band energy levels.[41-43]

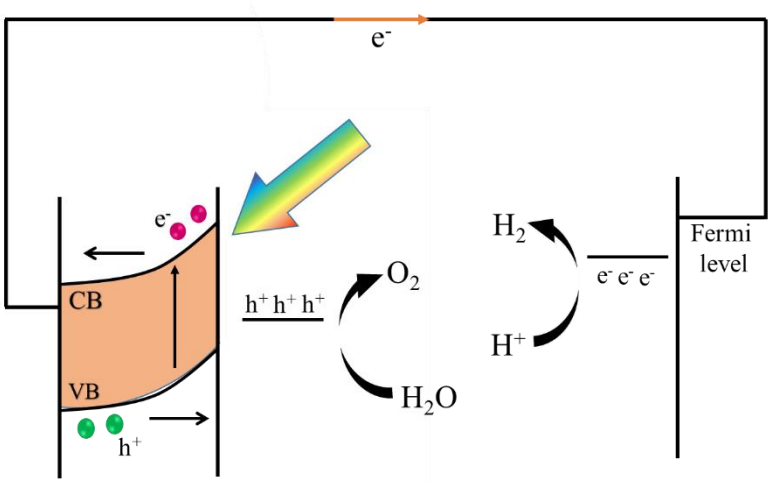

Figure 1.11 Schematic representation of PEC water splitting using an n-type semiconductor as the photo anode and a metal electrode as the cathode.

1.7 Challenges of Electrochemical Devices

The above mentiond electrochemical devices have several challenges and issues. For instance, increasing the energy density without compromising the power capability is a classical challenge in supercapacitors and batteries. It is mainly because the potential window of energy storage devices is limited by the available potential range of the electrolyte. Several strategies are adopted in the literature to improve the energy density which include the employment of non-aqueous electrolytes, water in salt electrolytes and ionic liquids. These

strategies have expanded the potential window beyond the conventional limits of 1.23 V,[44] however there are several disadvantages. For example, non-aqueous electrolytes generally suffer from low ionic conductivity, higher toxicity and flammability whereas water in salt and ionic liquids strategies suffer from low ionic conductivity and lower gravimetric energy density. [45,46]

In electrolytic systems like electrodialysis, there are two major shortcomings. On one hand, it suffers from large ohmic (iR) losses since the salt removal happens against the concentration gradient. On the other hand, the OER occurring in the anodic half-cell has sluggish electrode kinetics leading to serious energy losses. For these reasons, the minimum voltage required for electrodialysis at a reasonable rate is much larger than the thermodynamic voltage of water splitting (1.23 V).[47–49]

In photochemical water splitting, the water oxidation and reduction potential must lie within the bandgap of the semiconductor material. But in most of the cases the valence band or conduction band does not properly align with the water redox levels. Sometimes, the conduction band have the lower energy than the reduction potential of water. In such a case, additional external potential has to be applied to move the conduction band to the energetically higher side, so that the electrons can have sufficient energy to reduce the water.[50-52] Several strategies are used in the literature to decrease the required potential in PEC water splitting, like making heterojunctions, doping with other metal ions and

making composite materials. But all these strategies still demand the application of a substantial electrical bias thereby making the process electricity ineffective.

In the case of electro organic synthesis, the over potential for the counter reaction often limit the overall performance metrics of the device. This is addressed in the literature by preparing more efficient electrode materials including nanomaterials, employing dopants, making composites, exposing reactive crystal planes etc. While all these strategies contribute to improved performance, the process still remain electricity ineffective due to the large overpotential requirement associated with the counter reaction. The foregoing discussion highlight that it is the need of the hour to introduce strategies and methodologies that can pave the way for energy storage devices with enhanced voltage output and energy conversion devices with lower electrical power input.

1.8. Unconventional Pathway to Improve the Performance of Electrochemical Energy Devices

In this thesis, it will be demonstrated that the OH^-/H^+ dual-ion gradient energy can be harvested to overcome the challenges and issues associated with state of the art electrochemical devices. Specifically, the hidden electromotive force available in the OH^-/H^+ dual-ion gradient electrolyte is utilized to improve the performance metrics of aqueous supercapacitors, electrodialysis cells, PEC water splitting device and electrochemical cells for electroorganic synthesis.

1.9. OH^-/H^+ Dual-ion Gradient Energy

The acid-base neutralization energy or the OH^-/H^+ dual-ion gradient energy is the energy released when the said dual ions combine to form water and a salt. During this process, an enormous amount of heat is produced. The neutralization reaction is an exothermic and a spontaneous process with a standard molar enthalpy change (ΔH^0) of 55.84 kJ mol^{-1} and a standard entropy change (ΔS^0) of 80.66 J mol^{-1} K^{-1}. Therefore, acid–base neutralization has a standard molar Gibbs free energy change (ΔG^0) of 79.9 kJ mol^{-1}.

$$H^+ + OH^- \rightarrow H_2O \qquad \ldots.1.14$$

The total cell reaction for a pH gradient cell is,

$$H^+(aq) + OH^-(aq) \rightarrow H_2O(l) \qquad .....1.15$$

The free energy change for the reaction can be written as follows:

$$\Delta G = \Delta G^o + RT \ln \frac{product}{reactant}$$

$$\Delta G_{\text{ Neutralization}} = \Delta G^o_{\text{ Neutralization}} + RT \ln \frac{[H2O]}{[H+][OH-]}$$

$$\Delta G_{\text{ Neutralization}} = \Delta G^o_{\text{ Neutralization}} - RT \ln [H^+] - RT \ln [OH^-]$$

$$\Delta G_{\text{ Neutralization}} = \Delta G^o_{\text{ Neutralization}} - RT\ 2.303\ (\log[H^+] + \log[OH^-])$$

$$\Delta G_{\text{ Neutralization}} = \Delta G^o_{\text{ Neutralization}} - RT\ 2.303\ (-pH - pOH)$$

$$\Delta G_{\text{ Neutralization}} = \Delta G^o_{\text{ Neutralization}} + RT\ 2.303\ (pH + pOH)$$

$$\Delta G_{\text{ Neutralization}} = \Delta G^o_{\text{ Neutralization}} + RT\ 2.303\ (pH_A + 14 - pH_B),$$

where pH_A = pH of acidic compartment and pH_B = pH of alkaline compartment

$$\Delta G_{Neutralization} = \Delta G^{o}_{Neutralization} + RT\ 2.303\ (pH_A - pH_B) + RT\ 2.303*14\ (pH_B > pH_A)$$

$$\Delta G_{Neutralization} = \Delta G^{o}_{Neutralization} - RT\ 2.303\ \Delta pH + RT\ 2.303*14$$

$$\Delta G_{Neutralization} = -79.8 - 5.7\Delta pH + 79.8$$

$$\Delta G_{Neutralization} = -5.7\ \Delta pH \qquad \ldots. 1.16$$

According to the equation 1.16, the free energy change of neutralization reaction ($\Delta G_{Neutralization}$) depends on the pH difference (ΔpH) of the two electrolytes. As the ΔpH increases the $\Delta G_{Neutralization}$ becomes more negative. With time, pH difference of both the compartment should decrease (as the pH tending towards 7), and $\Delta G_{Neutralization}$ for the reaction should also decrease. When ΔpH is zero, $\Delta G_{Neutralization} = 0$, Figure 1.15. Even though the OH^-/H^+ dual ion gradient cell has an electromotive force, it is difficult to directly harvest it for electrical power generation as the reaction is non redox in nature. Thus, the major focus of this thesis is to utilize this hidden electromotive force to enhance the voltage output of galvanic devices and to decrease the voltage input of electrolytic devices.

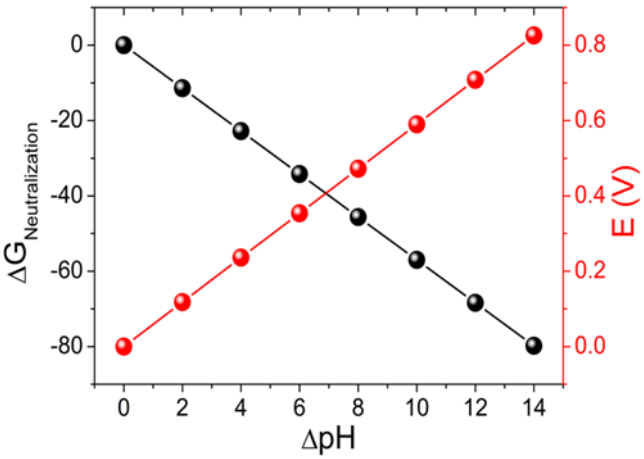

Figure 1.15 Gibbs free energy change and potential plot with respect to OH^-/H^+ dual-ion gradients.

1.10. Aim and scope

The major aim of this thesis is to utilize the hidden electromotive force available with the OH^-/H^+ dual-ion gradients to improve the performance of state-of-the-art electrochemical devices. It is broadly divided into two sections. First aspect of the thesis is the harvesting of the OH^-/H^+ dual-ion gradient energy to enhance the voltage output of galvanic devices. Second aspect of the thesis is related to electrolytic devices wherein the hidden electromotive force of OH^-/H^+ dual-ion gradient is utilized to substantially decrease the input electric power. The thesis has the following running Chapters.

Chapter 1. This Chapter provides justification for the exploration of alternative and renewable energy resources in the context of paramount pollution and global climate change. Nevertheless, a complete shifting to a carbon neutral energy chain is challenged by the temporal and

geographic fluctuations of renewables. This demand electrochemical energy storage and conversion devices to bridge the gap between the peak of energy availability and the peak of energy demand. However, the performance of electrochemical energy devices is often limited by their threshold energy storage capability, available voltage window, possibilities of parasitic chemistry, electricity ineffective electrolysis etc. To address these classical challenges, we have employed a two compartment electrochemical device by decoupling the direct acid alkali chemistry by a proton conducting membrane. This OH^-/H^+ dual-ion gradient has a hidden electromotive force of 0.82 V under standard conditions; however, its non-redox nature completely prevents its direct interconversion as electrical driving force. In the working Chapters to follow, we demonstrate how the performance metrics of state-of-the art-energy storage and conversion devices can be remarkably improved by harvesting the hidden electromotive force available with OH^-/H^+ dual-ion gradients.

Part I

Chapter 2. This Chapter deals with the classical challenge of improving the energy density of electrochemical capacitors without compromising their power capability by utilizing the hidden electromotive force available with OH^-/H^+ dual-ion gradients. Since the energy of an electrochemical capacitor is quadratically related to the working voltage window, the most beneficial strategy to boost the energy density is to target the operating voltage window. However,

expanding the voltage window beyond 1.23 V in aqueous systems is thermodynamically challenged due to parasitic water splitting reaction. We show that the parasitic chemistry can be arrested by decoupling the direct acid-alkali chemistry by employing the hidden electromotive force in OH^-/H^+ dual-ion gradient electrolyte, and consequently, the voltage window in aqueous supercapacitors can be expanded to 2 V while boosting the energy density up to ~230% (Figure 1).

Part II

Chapter 3. This Chapter deals with the integrating bifunctional functionality in a single electrochemical device by harvesting the hidden electromotive force available with OH- /H+ dual-ion gradients. With OH^-/H^+ dual ion gradient electrolytic cell, an electrochemical device capable for simultaneous electro desalination and H_2 generation in an electricity-effective manner is demonstrated. The OH^-/H^+ dual-ion gradient electrolytic cell at a current density of 40 mA/cm^2 performs electrodesalination with minimal parasitic chemistry while generating ~33 ml/h of H_2 at a terminal voltage of ~1 V, which is only half of the voltage required in a symmetric single ion configuration. Contrary to conventional desalination process, the low-voltage electrodesalination in OH^-/H^+ dual-ion gradient electrolytic cell noticeably improves the energy efficiency and prevents competitive parasitic chemistry.

Chapter 4. This Chapter discusses electricity effective photoelectrochemical (PEC) water splitting to store the solar energy in

the chemical bonds of molecular hydrogen. Among several photo electrodes used for PEC water splitting, α-Fe_2O_3 is a promising material due to its suitable bandgap, chemical stability, and abundance. Despite these, the position of its conduction band does not allow spontaneous movement of photo-generated electrons to cause the water reduction. In single-ion configuration, this demands the application of a minimum electrical bias of ~1.5 V vs. SHE to increase the energy of the conduction band such that it will be energetically above the H_2O/H_2 redox level. By utilizing the hidden electromotive force available with OH^-/H^+ dual-ion gradients, the minimum electrical voltage required for PEC water splitting can be brought down to ~0.8 V. OH^-/H^+ dual-ion assisted PEC water splitting required only 0.95 V to produce a current density of 10 mA/cm^2 , and for achieving the same current density in a conventional symmetric ion configuration requires at least a doubling of the applied electrical bias (~1.8 V).

Chapter 5. This Chapter shows how the hidden electromotive force of 0.82 V available with OH^-/H^+ dual-ion gradient cell can be directly harvested as electrical driving force for performing simultaneous electro-organic synthesis and hydrogen fuel production in an electricity effective manner. To demonstrate this dual-ion gradient assisted electro-organic synthesis, 5-hydroxymethylfurfural (HMF) is chosen as the model molecule because of the immense techno commercial applications of its oxidized products. This dual-ion assisted device only required ~1 V to provide a current density of 50 mA/cm^2 and for

achieving the same rate; the traditional state-of-the-art electrolytic cell required a doubling of the applied potential. The dual-ion gradient assisted device can convert biomass-derived HMF to economically important FDCA with ~90 % yield and ~87 % Faradaic efficiency with simultaneous H_2 fuel production at a potential as low as 1 V.

1.11. References

[1] Hubacek, K.; Guan, D.; Barua, A.; Changing lifestyles and consumption patterns in developing countries: A scenario analysis for China and India. *Futures* **2007**, *39*, 1084-1096.

[2] Jess, A. what might be the energy demand and energy mix to reconcile the world's pursuit of welfare and happiness with the necessity to preserve the integrity of the biosphere? *Energy Policy*, **2010**, *38*, 4663-4678,

[3] Zsogon1, A.; Peres, L. E. P.; Xiao, Y.; Yan J.; Fernie, A. R.; Enhancing crop diversity for food security in the face of climate uncertainty *The Plant Journal*, **2022**, *109*, 402–414.

[4] Lewis, N. S.; Nocera, D. G.; Proceedings of the National Academy of Sciences. **2006**, *103*, 15729-15735.

[5] Jacobson, M. Z.; Krauland, A.K.V.; Coughlin, S. J.; Dukas, E.; Nelson, A. J. H.; Palmer, F. C.; Rasmussen, K. R.; Low-cost solutions to global warming, air pollution, and energy insecurity for 145 countries. *Energy Environ. Sci.* **2022**, *15*, 3343-3359.

[6] Zhu, J.; Hu, L.; Zhao*, P.; Lee, L.U.S.; Wong, K.Y. Recent Advances in Electrocatalytic Hydrogen Evolution Using Nanoparticles. *Chem. Rev.* **2020**, *120(2)*, 851–918.

[7] Demirbas, A.; Combustion characteristics of different biomass fuels. *Prog. Energy Combust. Sci.*, **2004**, *30*, 219-230.

[8] Mark, E.; Dry Fischer–Tropsch reactions and the environment. Appl Catal A: Gen **1999**, *189*, 185-190.

[9] Kaygusuz, K.; Energy and environmental issues relating to greenhouse gas emissions for sustainable development in Turkey. Renewable Sustainable Energy Rev. **2009**, *13*, 253-270.

[10] Omer, A.M.; Energy, environment and sustainable development. *Renewable Sustainable Energy Rev*. **2008,** *12***,** 2265-2300.

[11] Statistical Review of World Energy, http://www.bp.com/statisticalreview.

[12] Midilli, A.; Ay, M.; Dincer, I.; Rosen, M. A.; *Renewable Sustainable Energy Rev*. **2005**, *9*, 255-271.

[13] Zamani, M.; Kordrostami Z.; Performance Enhancement of Inclined Core-Shell Nanowire Solar Cells Using Multivariable Optimization. *Solar Energy* **2022**, *243*, 443-453.

[14] Huang,W.; Luo W.; Li,Y.; Two-dimensional semiconducting covalent organic frameworks for photocatalytic solar fuel production. *Meterilstoday* **2020,** *40*, 160-172.

[15] Liu, W.; Zhang, Z.; Chen, J.; J, D.; Wu, F.; Fan, J.; Li, Y.; Feasibility evaluation of large-scale underground hydrogen storage in bedded salt rocks of China: A case study in Jiangsu province. *Energy*, **2020**, *198*, 117348.

[16] van de Krol, R.; Grätzel, M., Introduction. In Photoelectrochemical Hydrogen Production. *Springer US*, **2012**, 3-11.

[17] Zang, X.; Shen, C.; Sanghadasa, M.; Lin, L.; High-Voltage Supercapacitors Based on Aqueous Electrolytes. *ChemElectroChem*, **2019,** *6*, 976-988.

[18] Chatterjee, D. P.; Nandi, A. K.; A review on the recent advances in hybrid supercapacitors. *J. Mater. Chem. A*, **2021**, *9*, 15880-15918

[19] Najib S.; Erdem E.; Current progress achieved in novel materials for supercapacitor electrodes: mini review. *Nanoscale Adv*., **2019**, *1*, 2817-2827.

[20] Sharma, P.; Bhatti, T.S.; A review on electrochemical double-layer capacitors, *Energy Conversion and Management* **2010**, *51*, 2901-2912.

[21] Bhojane, P.; Recent advances and fundamentals of Pseudocapacitors: Materials, mechanism, and its understanding. *J Energy Storage*. **2022**, *45*,103654.

[22] Fleischmann, S.; Mitchell, J. B.; Wang, R.; Zhan, C.; Jiang, De-en; Presser, V.; Augustyn, V.; Pseudocapacitance: From Fundamental

Understanding to High Power Energy Storage Materials**.** *Chem. Rev.* **2020**, *120*, 6738–6782.

[23] Yabuuchi, N.; Kubota, K.; Dahbi, M.; Komaba, S. Research Development on Sodium-Ion Batteries. *Chem. Rev.* **2014**, *114*,11636–11682.

[24] Manthiram, A.; A Reflection on Lithium-ion Battery Cathode Chemistry. Nature Comm. **2020**, *11*, 1550.

[25] Brodd, R.J.; Secondary Batteries | Overview. Encyclopedia of Electrochemical Power Sources, **2009**, 254-261.

[26] Kordesch, K.; Taucher-Mautner, W.; History | Primary Batteries. **2009**, 555-564.

[27] Peighambardoust, S.J.; Rowshanzamir, S.; Amjadi, M.;Review of the proton exchange membranes for fuel cell applications, Int. J. Hydrog. Energy, **2010**, *35*, 9349-9384.

[28] Jiao, K.; Xuan, J.; Du, Q.; Bao, Z.; Xie, B.; Wang, B.; Zhao, Y.; Fan, L.; Wang, H.; Hou, Z.; Huo, S.; Brandon, N.P.; Yin, Y.; Guiver M. D.; Designing the next generation of proton-exchange membrane fuel cells. *Nature*, **2021**, *595*, 361–369.

[29] Zhu, C.; Ang, N. W. J.; Meyer, T. H.; Qiu, Y.; Ackermann L. Organic Electrochemistry: Molecular Syntheses with Potential. *ACS Cent. Sci.* **2021**, *7*, 415–431

[30] Pollok, D.; Waldvogel, S. R.; Electro-organic synthesis – a 21st century technique. *Chem. Sci.*, **2020**, *11*, 12386-12400.

[31] Ali, T.; Wang, H.; Iqbal, W.; Bashir, T.; Shah, R.; Hu Y.; Electro-Synthesis of Organic Compounds with Heterogeneous Catalysis. *Adv. Sci.*, **2022**, *2205077(1-48)*

[32] Millet, P.; Mbemba, N.; Grigoriev, S.A.; Fateev, V.N.; Aukauloo, A.; Etiévant, C.; Electrochemical performances of PEM water electrolysis cells and perspectives, Int. J. Hydrog. Energy **2011**, *36*,4134 – 4142.

[33] Chatenet, M.; Pollet, B. G.; Dekel, D.R.; Dionigi, F.;Deseure, J.; Millet, P.; Braatz, R. D.; Bazant, M. Z.; Eikerling, M.; Staffell, I.; Balcombe,P.; Shao-Horn, Y.; Schäfer H.; Waterelectrolysis: from textbook knowledge to the latest scientific strategies and industrial developments. *Chem. Soc. Rev.*, **2022**, *51*, 4583-4762

[34] You, B.; Sun, Y.; Innovative Strategies for Electrocatalytic Water Splitting. *Acc. Chem. Res.* **2018**, *51*,1571–1580.

[35] Kumar, S. S.; Himabindu, V.; Hydrogen production by PEM water electrolysis – A review, Materials Science for Energy Technologies. **2019**, *2*,442-454.

[36] Selamet, Ö. F.; Becerikli, F.; Mat, M. D.; Kaplan, Y.; Development and testing of a highly efficient proton exchange membrane (PEM) electrolyzer stack. *Int. J. Hydrog. Energy.* **2011**, *36*,11480-11487.

[40] Fujishima, A.; Honda, K.; Electrochemical Photolysis of Water at a Semiconductor Electrode. *Nature* **1972**, *238*, 37–38.

[41] Ros, C.; Andreu, T.; Morante J. R.; Photoelectrochemical water splitting: a road from stable metal oxides to protected thin film solar cells. *J. Mater. Chem. A*, **2020**, *8*, 10625-10669

[42] Joy, J.; Mathew, J.; George, S. C.; Nanomaterials for photoelectrochemical water splitting – review. *Int. J. Hydrog. Energy.* **2018**, *43*,4804-4817.

[43] Yu, J. M.; Lee, J.; Kim, Y. S.; Song, J.; Oh, J.; Lee, S. M.; Jeong, M.; Kim, Y.; Kwak, J. H.; Cho, S.; Yang C.; Jang J. High-performance and stable photoelectrochemical water splitting cell with organic-photoactive-layer-based photoanode. *Nature Comm.* **2020**, *11*, 5509

[44] Mourad, E., Coustan, L., Lannelongue, P.; Zigah, D.; Mehdi, A.; Vioux, A.; Freunberger, S. A.; Favier, F.; Fontaine O.; Biredox ionic liquids with solid-like redox density in the liquid state for high-energy supercapacitors. *Nature Mater* **2017**, *16*, 446–453

[45] Park, J.; Lee, J.; Kim, W.; Water-in-Salt Electrolyte Enables Ultrafast Supercapacitors for AC Line Filtering. *ACS Energy Lett.* **2021**, *6*, 769–777.

[46] M. Salomon, Electrolytes | Non-Aqueous, Encyclopedia of Electrochemical Power Sources, **2009**,160-165,

[47] Nam, D.; Lumley, M. A.; Choi, K. Electrochemical Redox Cells Capable of Desalination and Energy Storage: Addressing Challenges of the Water–Energy Nexus. *ACS Energy Lett.* **2021**, *6*, 3, 1034–1044.

[48] Severin, B. F.; Hayes, T. D. Effect of Electrode Rinse Solutions on the Electrodialysis of Concentrated Salts. *Sep. Purif. Technol.* **2021**, *274*, 119048.

[49] Veerman, J.; Saakes, M.; Metz, S. J.; Harmsen, G. J. Reverse Electrodialysis: Evaluation of Suitable Electrode Systems; *J. Appl. Electrochem.* **2010**, *40*, 1461–1474.

[50] Jun H.; Im B.; Kim, J. Y.; Im, Y., Jang, J.; Kim, E. S.; Kim, J. Y.; Kang, H. J., Hong S. J.; Lee J. S.; Photoelectrochemical water splitting over ordered honeycomb hematite electrodes stabilized by alumina shielding. *Energy Environ. Sci.*, **2012**, *5*, 6375–6382.

[51] Peter, L. M.; Wijayantha, K. G. U.; Tahir A. A.; Kinetics of light-driven oxygen evolution at α-Fe_2O_3 electrodes. *Faraday Discuss.* **2012**, *155*, 309–322.

[52] Li, Y.; Liu, K.; Zhang, J.; Yang, J.; Huang, Y.; Tong, Y.; Engineering the Band-Edge of Fe_2O_3/ZnO Nanoplates via Separate Dual Cation Incorporation for Efficient Photocatalytic Performance: *Ind. Eng. Chem. Res.* **2020**, *59*, 18865–18872.

Chapter 2

Aqueous OH^-/H^+ Dual-ion Gradient Energy assisted High Voltage Supercapacitor

Abstract

The Improving energy density without compromising the power capability is a classical challenge for electrochemical suppercapacitor. Since the energy is quadratically related to voltage by the equation ½(capacitance)(voltage window)^2, so the most beneficial strategy to bust the energy density is to improve the voltage window. However, expanding the voltage window beyond 1.23 V in aqueous system is thermodynamically challenge due to parasitic water spelling reaction. We show that the parasitic chemistry can be arrested by decoupling the direct acid-alkali chemistry, and the voltage window in aqueous supercapacitors can be expanded with energy boosting up to ~230%.

2.1 Introduction

This Chapter discusses how OH^-/H^+ dual-ion gradient energy can be harvested to increase the energy density of aqueous supercapacitors without compromising their power capability. Electrochemical energy storage and conversion devices are potential candidates to restrict global warming within 1.5 °C as proposed by UN conference on climate change. [1–15] Batteries though possess high energy density, suffer from well-known power deficiency and electro-chemical capacitors exhibit a diametrically opposite behaviour with a well-known energy deficiency. [2,16,17] High energy and high power supercapacitors are especially challenging in aqueous system because of thermodynamically restricted voltage window of 1.23 V. [2,17,18] A supercapacitor store charges by reversible adsorption- desorption of ion on its surface (EDLC) or by a reversible, they fail to work properly when irreversible electrochemical processes happen. Therefore, the operation voltage of a supercapacitor cell is limited by the reversible electrochemical window of its two electrodes Hydrogen evolution reaction (HER) occurs at 0.0 V whereas oxygen evolution reaction occurs at 1.23 V, so for an aqueous supercapacitor has to charge and discharge between that potential window .if we go beyond that window irreversible solvent Here we show that by decoupling the direct acid alkali chemistry, the parasitic water splitting chemistry can be arrested and the voltage window can be expanded to a value close to 2 V with energy boosting up to ~230%.

2.2 Experimental

2.2.1. Materials and chemicals

Chemical such as ruthenium chloride (75%), sodium hydroxide (97%) and sulfuric acid (98%) were procured from Alfa-aesar India. Activated carbon powder was procured from Alfa Aesar. Nafion117 membrane was procured from Sigma-Aldrich India. Nafion117 membrane was pre-treated before use.

2.2.2. Experimental procedure

All electrochemical experiments, including cyclic voltammetry, charge discharge, leakage current and self-discharge were done with the VMP 300 electrochemical workstation (Bio-logic, France). Hydrous ruthenium oxide was prepared by sol-gel method as reported in the literature. [16–18] Briefly to a solution of ruthenium chloride (0.1 M) sodium hydroxide (pH = 14) was added drop wise till the solution attained a neutral pH where hydrous RuO_2 got precipitated. It was filtered and washed thoroughly with ethanol and water. The dried sample was annealed at 175°C for 2 h. Electrode slurry was prepared by mixing hydrous RuO_2 with 5% PTFE binder and sonicating it for 30 min. Working electrode was made by drop casting the slurry on a glassy carbon electrode at a loading ~0.14 mg/cm^2 and then it was allowed to dry for an hour. Ag/AgCl (3.5 M KCl) was used as the reference

electrode and platinum mesh was used as the counter electrode. Cyclic voltammetry was carried out in acid medium of pH = 0 (H_2SO_4) and in alkaline solution of pH = 14 (NaOH). To expand the working voltage window, a two compartment cell with acid and alkali compartments separated by a Nafion117 membrane was employed with electrodes in a symmetrical two electrode configuration. Activated carbon slurry was prepared by mixing activated carbon with 5% PTFE binder and sonicating it for 30 min. Working electrode was made by drop casting the slurry on a glassy carbon electrode at a loading~0.14 mg/cm^2 and then it was allowed to dry for an hour. Ag/AgCl (3.5 M KCl) was used as the reference electrode and platinum mesh was used as the counter electrode. All other experimental protocols were identical to that RuO_2 supercapacitor. The specific capacitance is estimated from galvanostatic charge discharge test using Eq. (1) [19]:

$$C_{sp} = \frac{I\,\Delta t}{m\,\Delta V} \qquad \text{.....(1)}$$

where C_{sp} is the specific capacitance, I is current at which capacitor is discharged, m is mass of the material per electrode, ΔV is the iR drop corrected potential window ($V - V_{IR}$) in volts, and Δt is the discharge time excluding the iR drop. The specific energy and specific power were calculated in symmetrical two electrode configuration using Eqs. (2) and (3) [19]:

$$E = \frac{1}{2}C_{sp}V^2 \qquad \text{.....} \quad 2$$

$$P = \frac{E}{\Delta t} \qquad \ldots\ldots\ldots \; 3$$

where V is the iR drop corrected potential window in volts, and Δt is the discharge time excluding the iR voltage drop.

3. Results and discussion

Proposed electrochemical cell for expanding the voltage window constitutes an anodic and a cathodic compartment respectively filled with alkaline and acidic solutions separated by a cation conducting Nafion117 membrane, Figure 1(a). This configuration is chosen for the following reasons. Hydrogen evolution reaction (HER) and oxygen evolution reaction (OER), the respective water splitting half-cell reactions are pH dependent with a slope of 59 mV/pH, Figure 1(b), Pourbaix diagram suggests that, in OH^- solution (pH 14), HER would occur at ~810 mV vs. SHE and in H^+ solution (pH 0) compared to OER at ~1230 mV vs. SHE in acidic pH, Figure 1(b). [18,20,21] These suggest that on decoupling the direct acid base chemistry by a cation selective Nafion membrane, the water splitting voltage can be expanded from 1.23 V to ~2 V, Figure 1(b) shaded region. This benefit can be exploited for boosting the energy density of well-known carbon based double layer capacitors and ruthenium oxide based pseudocapacitors as demonstrated below. First we show our concept of dual-ion gradient electrolyte for an electrochemical double layer supercapacitor.

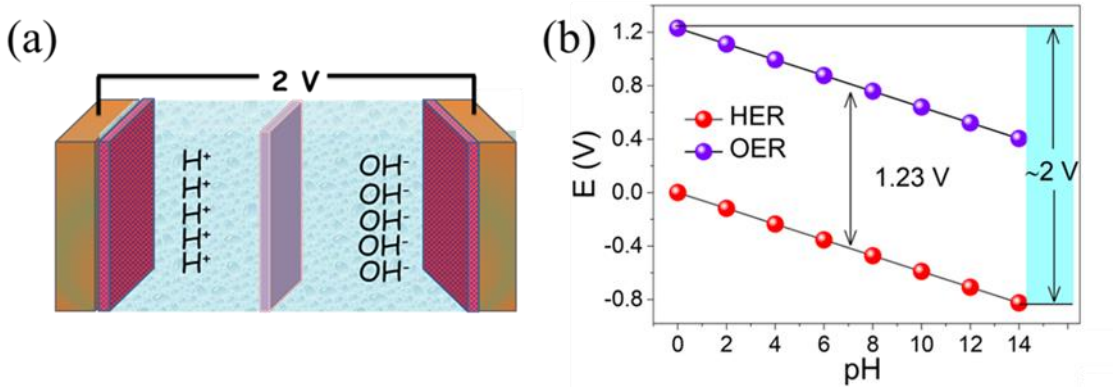

Figure 1: (a) Schematics of the high voltage aqueous supercapacitors and (b) the Pourbaix diagram for the water splitting half-cell reactions.

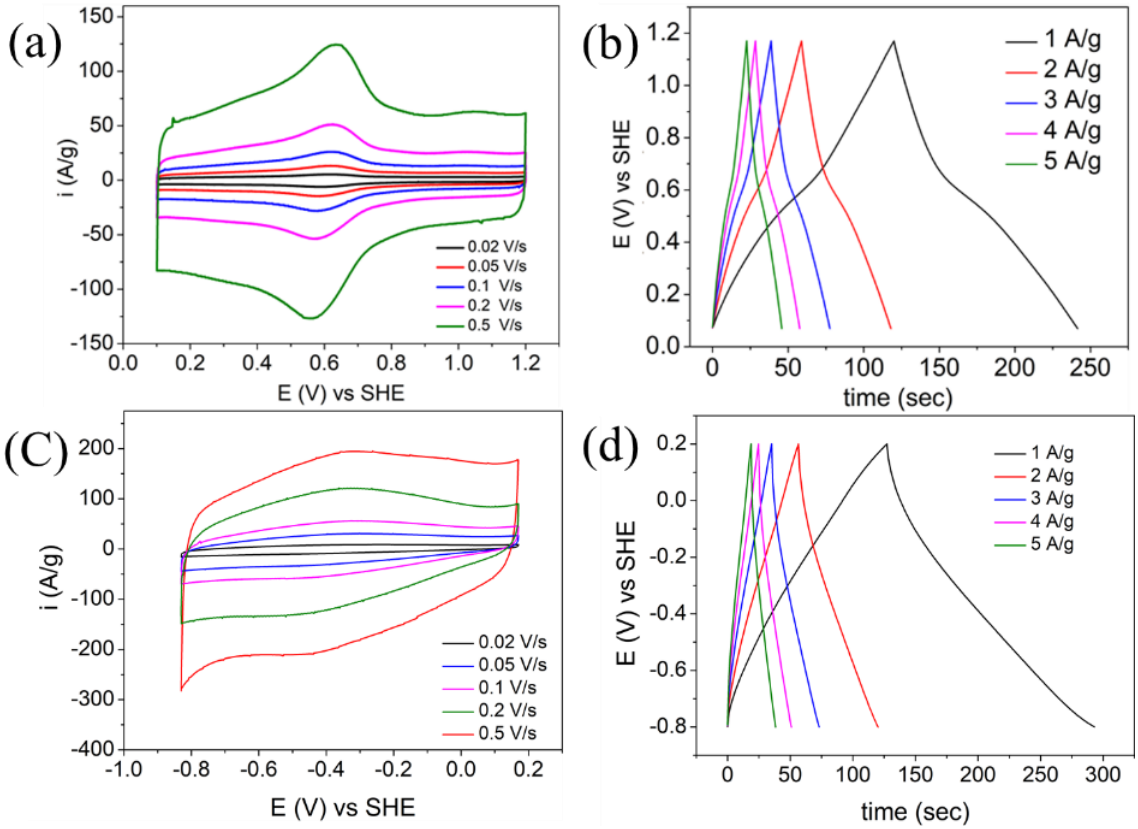

Figure 2: (a) Cyclic voltammograms of ruthenium oxide electrode in pH = 0 solution at various scan rates and (b) its charge-discharge behaviour. (c) Cyclic voltammograms of ruthenium oxide electrode in

pH = 14 solution at various scan rates and (d) its charge-discharge behaviour.

For that we have prepare activated carbon materials from Vulcan carbon and treated that with a nitric acid to increase the capacitance. The scan rate dependence of Vulcan carbon in acidic medium suggest that it possess decent rate capability, Figure 2(a), however the possible voltage window is just ~1.1 V because of the complexity of water oxidation and reduction at higher and lower potentials respectively. Galvanostatic charge-discharge also shows similar capacitance in that maximum available potential window figure 2b. After that, same

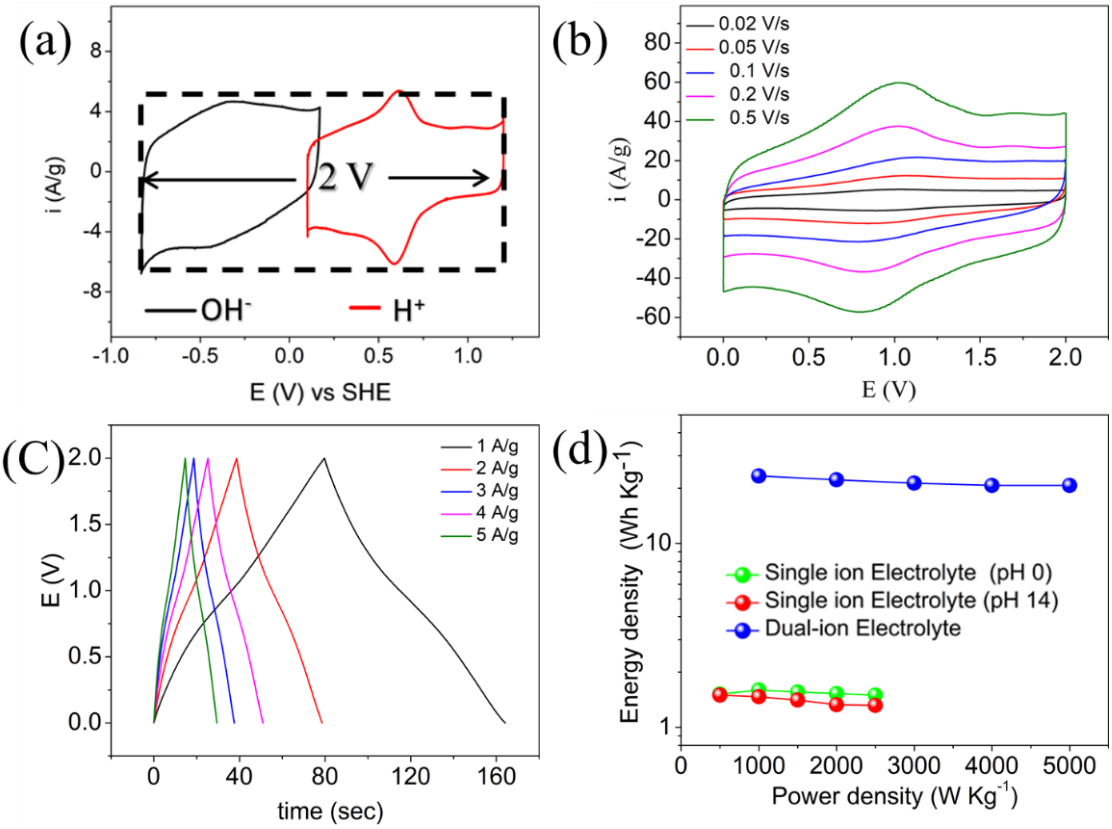

Figure 3: (a) Cyclic voltammogram of RuO_2 electrode in pH 0 and pH 14 solutions with respect to a common reference electrode at a scan rate of 20 mV/s. (b) Cyclic voltammetry and (c) charge discharge in two

electrode configurations when acid and alkaline compartments are decoupled by a Nafion117 membrane. (d) Ragone plots for RuO_2 in a symmetrical two configurations in acidic, alkaline and decoupled configurations.introduced in alkaline OH^- solution and available potential window of 1 V was found. figure 2c shows the scan rate dependence cyclic voltamogram in OH^- solution and figure 2d shows corresponding charge-discharge in that potential window.

carbon material is from the combine CV of OH^- and H^+ in Figure 3a, it is clear that a potential window of 2 V can be achieved, if the H^+ and OH^- solution can be decupled in a same device. Figure 3b is the device level cyclic voltamogram in two electrode dual-ion configuration and from that it is clear that a potential window of 2 V can be achieved in that configuration. The galvanostatic charge discharge in two electrode configuration (Figure 3c) shows that, supercapacitor can be charge upto 2 V with nearly 100% culombic efficiency. This boosted the energy density from just ~36 W h/kg in acidic or 26 Wh/kg in alkaline media to ~120 Wh/kg in acid-alkali decoupled configuration. Hydrous RuO_2 is synthesized as per the literature [22]. X-ray diffraction pattern (XRD) of as synthesized sample predominantly features amorphous characteristics, however the crystal planes appeared on annealing the sample at 175°C for 2 h, Figure 4a. Indexing of the planes suggests that it is well matching with tetragonal crystal structure of RuO_2, JCPDS card number 01-075-4303. The broader features in XRD patterns are attributed to amorphous RuO_2 [23,24]. Energy dispersive X-ray spectra

(EDS) evidence the presence of Ru and oxygen as constituent elements, Figure 4b.

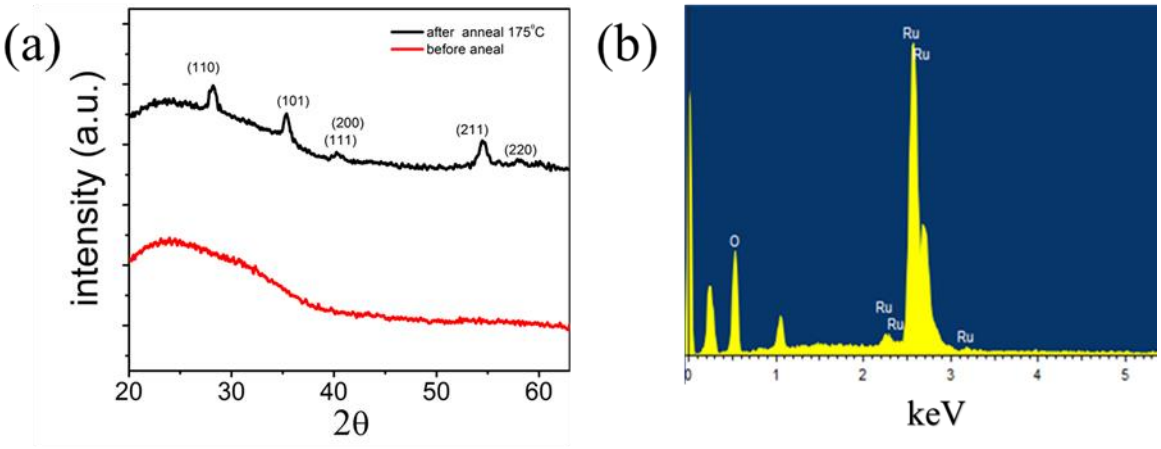

Figure 4: (a) XRD of as synthesized hydrous RuO_2 before and after annealing at 175°C for 2 hours. (b) EDS of hydrous RuO_2 after annealing at 175°C for 2 hours.

RuO_2 is a well-known super capacitive material owing to multiple oxidation states possible with the transition metal ions, Figure 2(a). Its behaviour can be described as a surface confined reversible electron transfer together with electrochemical adsorption/desorption of H^+ and OH^-, according to Equation (4) and (5) [25,26].

$$RuO_2 + xH+ + xe^- \rightarrow RuO_{2-x}(OH)_x \qquad (4)$$

$$RuO_2 + xH_2O + xe^- \rightarrow RuO_{2-x}(OH)_x + xOH^- \qquad (5)$$

During this process Ru oxidation states can change from (ii) up to (iv), and the value of x can be $0 \leq x \leq 2$. The continuous change of x during proton insertion/de-insertion is possible over a voltage window of ~1.3 V leading to supercapacitive behaviour in RuO_2 following a Frumkin-

type adsorption isotherm [25]. The scan rate dependence of RuO_2 in acidic medium suggest that it possess decent rate capability, Figure 5(a).

The galvanostatic charge-discharge profiles supports that the RuO_2 system can be used to store energy within this voltage window with decent capacity retention, Figure 5b. In alkaline medium, it demonstrated a voltage window of ~1.2 V, Figure 5(c) and the expansion of voltage window beyond this limit resulted in parasitic chemistry. Galvanostatic charge discharge demonstrates that the

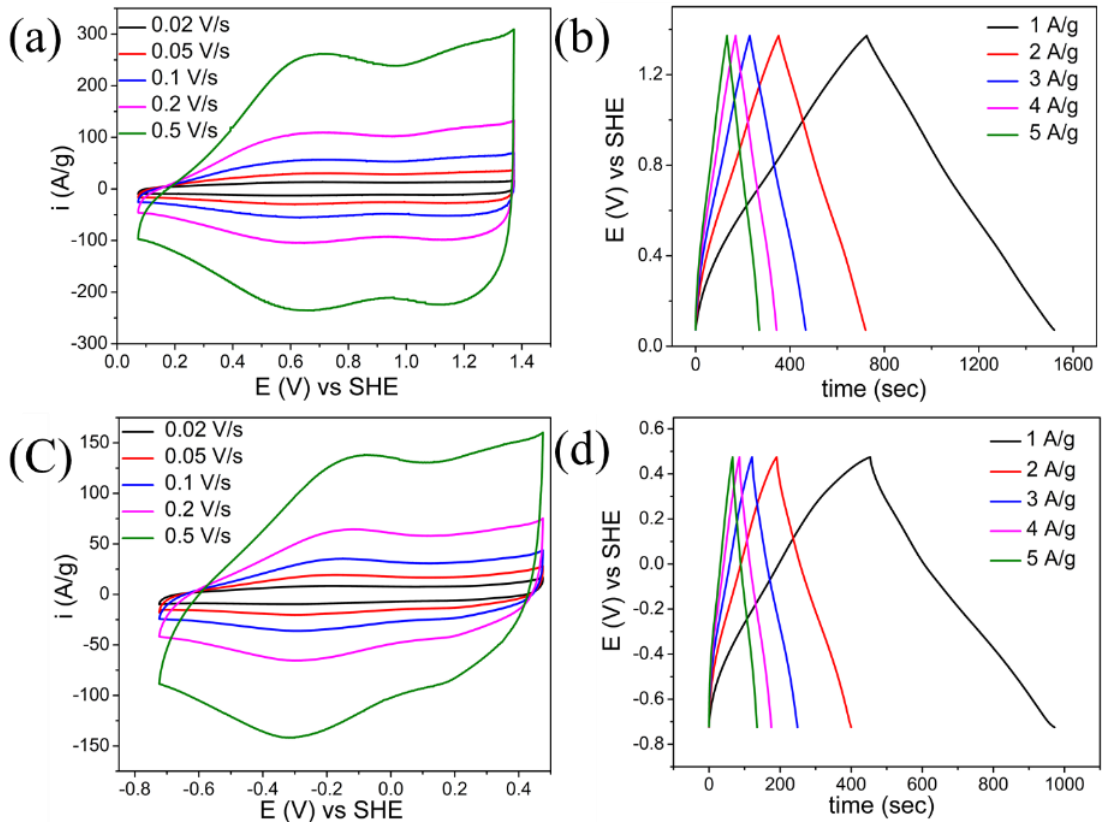

Figure 5: (a) Cyclic voltammograms of ruthenium oxide electrode in pH = 0 solution at various scan rates and (b) its charge-discharge behaviour. (c) Cyclic voltammograms of ruthenium oxide electrode in

pH = 14 solution at various scan rates and (d) its charge-discharge behaviour.

voltage window is restricted to ~1.2 V in alkaline medium, however with decent capacity retention, Figure 5(d). A lower capacitance encountered in alkaline medium compared to acidic medium, Figure 5, could be due to participation of water in the redox chemistry instead of proton in alkaline medium, Eq. (5) [26,28].

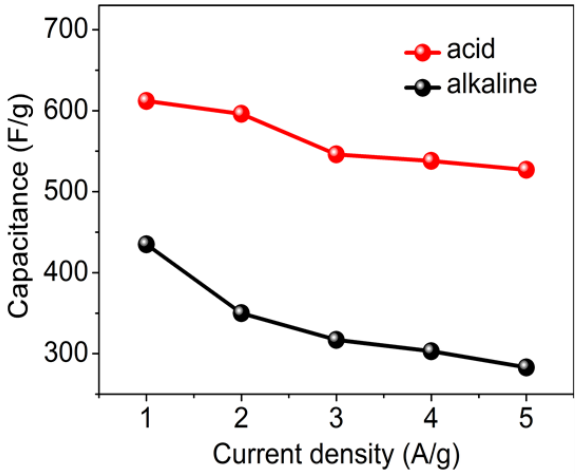

Figure 6: The capacity retention plots of RuO_2 in acidic (red trace) and alkaline (black trace) media. The values represent single electrode capacitances in three electrode configuration.

These suggest that acidic or basic media restrict the energy density of aqueous supercapacitors and by decoupling the direct acid base chemistry by a cation selective membrane as demonstrated in Figure 6a, the voltage window of RuO_2 system can be expanded to~2 V from 1.23 V, cyclic voltammograms, Figure 6a. This boosted the energy density from just ~36 Wh/kg in acidic or 26 Wh/kg in alkaline media

to ~120 Wh/kg in acid-alkali decoupled configuration. This ~230% increase in energy density is further reflected in their galvanostatic charge discharge curves, Figure 6(c). The capacity retention is decent however with an expanded voltage window, Figure 3(b), (c). Nevertheless, the obvious potential plateau close to 1.75 V (Figure 6c) especially at low rates signals the possibility of parasitic water oxidation on RuO_2 electrode.

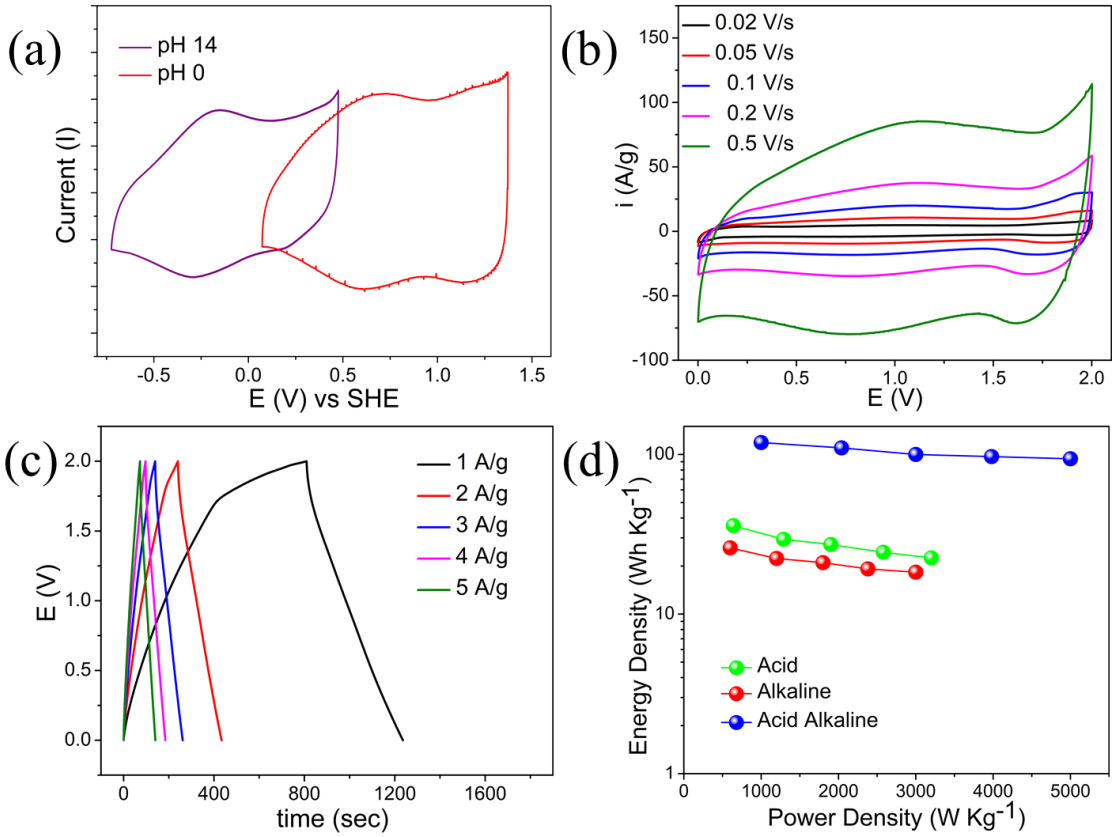

Figure 7: (a) Cyclic voltammogram of RuO_2 electrode in pH 0 and pH 14 solutions with respect to a common reference electrode at a scan rate of 20 mV/s. (b) Cyclic voltammetry and (c) charge discharge in two electrode configurations when acid and alkaline compartments are

decoupled by a Nafion117 membrane. (d) Ragone plots for RuO_2 in a symmetrical two configurations in acidic, alkaline and decoupled configurations.

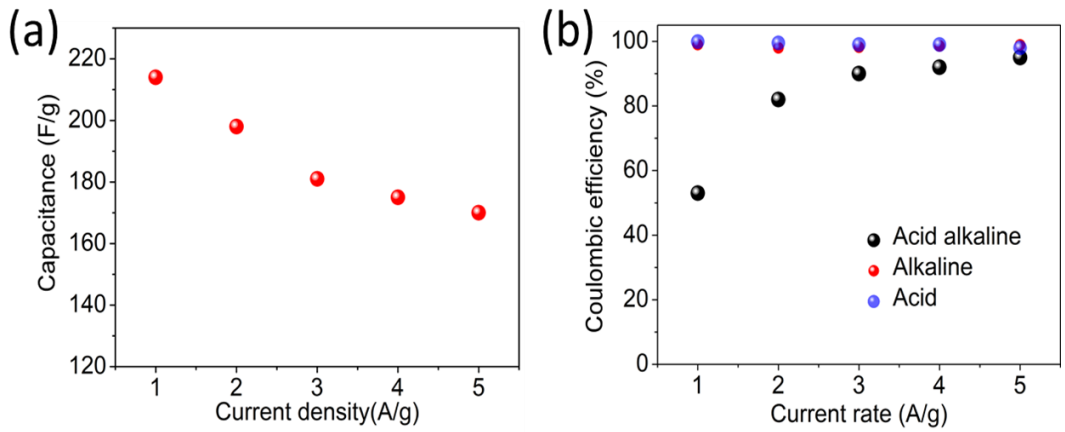

Figure 8: (a) The capacity retention plots of RuO_2 in decoupled configuration. The values represent capacitance of RuO_2 electrode in a symmetrical two electrode configuration and (b) columbic efficiency in acid, alkaline and acid-alkaline decoupled system for RuO_2 supercapacitors.

This is clear from the plot of coulombic efficiency vs. current rate plot (Figure 7b) The coulombic efficiency increases when the rate is increased indicating electrocatalytic water oxidation at lower rates. The Ragone plot (obtained after iR drop correction) suggest that in decoupled configuration energy density is boosted at all rates without compromising the power density compared to either acidic or alkaline media, Figure 6(d). The impedance analysis of RuO_2 electrode in acidic

and alkaline media, Figure 8a, suggest the equivalent series resistance (ESR) is comparatively higher in alkaline medium which could be due to the participation of water instead of protons for maintaining the electroneutrality [25,27]. This in combination with the resistive contributions from Nafion membrane should be responsible for the

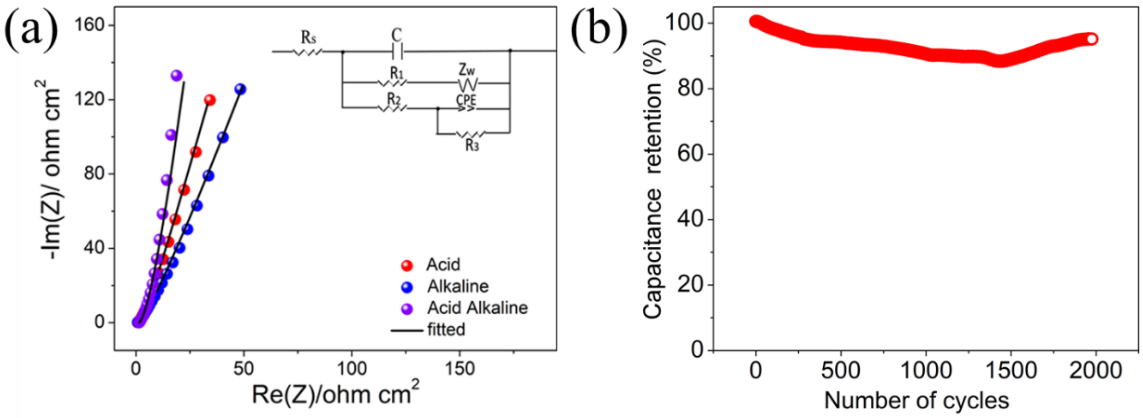

Figure 9: (a) Nyquist plot for RuO_2 in acidic, alkaline and decoupled configurations acquired at the open circuit voltage in the frequency range of 100 kHz to 10 mHz with an AC amplitude of 10 mV (peak to peak). Inset shows the enlarged high frequency region. (b) The extended cyclability plots of RuO_2 electrode in decoupled configuration at a rate of 4 A/g.

higher ESR of the RuO_2 electrode in the dual electrolyte configuration. Nevertheless, the decoupled configuration possessed decent cyclability showing upto 94% capacity retention even after 2000 cycles, Figure 8b. Further, we have compared our results on carbon and RuO_2 with the literature (Table 1) suggesting that the dual electrolyte configuration

enhances the energy density of aqueous supercapacitors without compromising the power capability.

Table 1: Performance metrics comparison of dual electrolyte configuration with the literature

Configuration	Energy density ($Whkg^{-1}$)	Power density ($kWkg^{-1}$)	References
Acidic medium (Activated carbon)	5	10	Patrice et al., Electrochemical Capacitors for Energy Management, Science. **2008**, *321*, 651–652.
Acidic medium (SWCNT)	7	20	Lee et al., Electrochemical properties of high-power supercapacitors using single-walled carbon nanotube electrodes, *Adv. Funtional Mater.* **2001**, *11*, 387–392.
Acidic medium (Graphene)	9.1	0.12	Dai et al., Advanced asymmetrical supercapacitors based on graphene hybrid materials, *Nano Res.* **2011**, *4*, 729–736.
Acidic medium (NiO/Graphe/ /RuO_2/graphene)	48	0.23	Dai et al., Advanced Asymmetrical supercapacitors based on graphene hybrid materials, *Nano Res.* **2011**, *4*, 729–736.
Alkaline	2.60	0.225	Liu et al., Fabrication of Novel Ternary Three-Dimensional

(RuO_2/ Graphitic-C3 N4@rGO)			RuO_2/Graphitic C3N4@reduced Graphene Oxide Aerogel Composites for Supercapacitors, *ACS Sustain. Chem. Eng.* **2017**, *5*, 4982–4991.
Acidic medium (RuO_2/graphene)	17.7	1	Cheng et al. Anchoring hydrous RuO_2 on graphene sheets for high-performance electrochemical capacitors, *Adv. Funct. Mater.* **2010**, *20* 3595–3602.
Acidic medium (RuO_2)	25	0.92	Naoi et al. Supercapacitor Performance of Hydrous Ruthenium Oxide Electrodes Prepared by Electrophoretic Deposition, *J. Electrochem. Soc.* 2006, 153, A321.
Neutral medium (RuO_2)	18.77	0.5	Lu et al., A Symmetric RuO_2/RuO_2 Supercapacitor Operating at 1.6 V by Using a Neutral Aqueous Electrolyte, *Electrochem. Solid-State Lett.* **2012,** *15* A60.
Dual Electrolyte (RuO_2)	~120	~1	Our work
Dual Electrolyte (Activated Carbon)	~23	~1	Our work

4. Conclusion

Improving the energy density without compromising the power capability is a classical challenge in the area of electrochemical capacitors. By arresting the direct acid base chemistry, we have demonstrated a strategy to expand the working voltage window of aqueous supercapacitors with simultaneous amplification of its energy density. The presented strategy expanded the voltage window from 1.23 V to ~2 V while boosting the energy density by ~230% in decoupled configurations. This presents a viable methodology for boosting the energy density of aqueous supercapacitors without compromising the power capability.

5. References

[1] J. Rogelj, M. Den Elzen, N. Höhne, T. Fransen, H. Fekete, H. Winkler, R. Schaeffer, F. Sha, K. Riahi, M. Meinshausen, Paris Agreement climate proposals need a boost to keep warming well below 2 °C, *Nature* **2016,** *534,* 631–639.

[2] Mourad, E.; Coustan, L.; Lannelongue, P.; Zigah, D.; Mehdi, A.; Vioux, A.; Freunberger, S.A.; Favier, F.; Fontaine, O.; Biredox ionic liquids with solid-like redox density in the liquid state for high-energy supercapacitors, *Nat. Mater.* **2016**, *16*, 446–453.

[3] K. Anderson, G. Peters, The trouble with negative emissions, *Science*. **2016**, *354*, 182–183.

[4] Schafzahl, L.; Mahne, N.; Schafzahl, B.; Wilkening, M.; Slugovc, C.; Borisov, S.M.; Freunberger, S.A. Singlet oxygen during cycling of the aprotic sodium–O_2 battery, *Angew. Chem. Int. Ed.* **2017**, *56*, 15728–15732.

[5] Cavaliere, S.; Subianto, S.; Savych, I.; Jones, D.J.; Rozi, J.; Electrospinning: designed architectures for energy conversion and storage devices, *Energy Environ. Sci.* **2011,** *8*, 4761–4785.

[6] Miroshnikov, M.; Divya, K.P.; Babu, G.; Meiyazhagan, A.; Mohana, L.; Arava, R.; Ajayan, P.M.; John, G. Power from nature: designing green battery materials from electroactive quinone derivatives and organic polymers, *J. Mater. Chem. A* **2016**, *4*, 12370–12386.

[7] Anju, V.G.; Manjunatha, R.; Austeria, P.M.; Sampath, S. Primary and rechargeable zinc–air batteries using ceramic and highly stable TiCN as an oxygen reduction reaction electrocatalyst, *J. Mater. Chem. A*, **2016**, *4*, 5258–5264.

[8] Pino, M.; Herranz, D.; Chacon, J.; Fatas, E.; Ocon, P.; Carbon treated commercial aluminium alloys as anodes for aluminium-air batteries in sodium chloride electrolyte, *J. Power Sources* **2016**, *326*, 296–302.

[9] Sathiya, M.; Prakash, A.S.; Ramesha, K.; Tarascon, J.À.M.; Shukla, A.K. V_2O_5 anchored carbon nanotubes for enhanced electrochemical energy storage, J. Am. Chem. Soc. **2011,** *133*, 16291–16299.

[10] Ferreyra, N.; Coche-Guérente, L.; Fatisson, J.; López Teijelo, M.; Labbé, P.; Layer-by-layer self-assembled multilayers of redox polyelectrolytes and gold nanoparticles, *Chem. Commun.* **2003**, *6*, 2056–2057.

[11] Goodwin, S.; Walsh, D.A.; Closed bipolar electrodes for spatial separation of H_2 and O_2 evolution during water electrolysis and the development of high-voltage fuel cells, *ACS Appl. Mater. Interfaces* **2017**, *9*, 23654–23661.

[12] Choi, N.S.; Chen, Z.; Freunberger, S.A.; Ji, X.; Sun, Y.K.; Amine, K.; Yushin, G.; Nazar, L.F.; Cho, J.; Bruce, P.G.; Challenges facing lithium batteries and electrical double-layer capacitors, *Angew. Chem. Int. Ed.* **2012**, *51*, 9994–10024.

[13] Maiyalagan, T.; Alaje, T.O.; Scott, K.; Highly stable Pt-Ru nanoparticles supported on three-dimensional cubic ordered

mesoporous carbon (Pt-Ru/CMK-8) as promising electrocatalysts for methanol oxidation, *J. Phys. Chem. C.* **2012**,*116*, 2630–2638.

[14] Hassoun, J.; Panero, S.; Reale, P.; Scrosati, B. A new, safe, high-rate and high-energy polymer lithium-ion battery, *Adv. Mater.* **2009**, *21*, 4807–4810.

[15] Fakharuddin, A.; Jose, R.; Brown, T.M.; Fabregat-Santiago, F.; Bisquert, J.; A Perspective on the production of dye-sensitized solar modules, *Energy Environ. Sci.* **2014**, *7*, 3952–3981.

[16] Miller, J.R.; Simon, P.; Patrice, S. Electrochemical capacitors for energy management, *Science* **2008**, *321*, 651–652.

[17] A.G. Pandolfo, A.F. Hollenkamp, Carbon properties and their role in supercapacitors, *J. Power Sources*. **2006**, *157*, 11–27.

[18] X. Wang, R.S. Chandrabose, Z. Jian, Z. Xing, X. Ji, A 1.8 V aqueous supercapacitor with a bipolar assembly of ion-exchange membranes as the separator, *J. Electrochem. Soc.* **2016**,*163*, A1853–A1858.

[19] G. Wu, P. Tan, D. Wang, Z. Li, L. Peng, Y. Hu, C. Wang, High performance supercapacitors based on electrochemical-induced vertical-aligned carbon nanotubes and polyaniline nanocomposite electrodes, *Sci. Rep.* **2017**, *7*, 43676–43684.

[20] Fic, K.; Meller, M.; Menzel, J.; Frackowiak, E. Around the thermodynamic limitations of supercapacitors operating in aqueous electrolytes, *Electrochim. Acta* **2016,** *206*, 496–503.

[21] Bhat, Z. M.; Thimmappa, R.; Devendrachari, M.C.; Kottaichamy, A.R.; Shafi, S.P.; Varhade, S.; Gautam, M.; Thotiyl, M.O. Fuel exhaling fuel cell, *J. Phys. Chem. Lett.* **2018** 388–392.

[22] Zheng, J.P.; Cygan, P.J.; Jow, T.R. Hydrous ruthenium oxide as an electrode material for electrochemical capacitors, *J. Electrochem. Soc.* **1995**,*142*, 98–102.

[23] Long, J.W.; Swider, K.E.; Merzbacher, C.I.; Rolison, D.R.; Voltammetric characterization of ruthenium oxide-based aerogels and other RuO_2 solids: the nature of capacitance in nanostructured materials, *Langmuir* **1999**,*15*, 780–785.

[24] Directorate, P.S.; Monmouth, F. A new charge storage mechanism for electrochemical capacitors, *J. Electrochem. Soc.***1995**,*142*, 6–8.

[25] Tomiyasu, H.; Shikata, H.; Takao, K.; Asanuma, N.; Taruta, S.; Park, Y.Y. An aqueous electrolyte of the widest potential window and its superior capability for capacitors, *Sci. Rep.* **2017**, *7*, 45048–45060.

[26] Kurzweil, P.; Hartmann, H.; Schell, C. The redox chemistry of ruthenium dioxide: a cyclic voltammetry study—review and revision, *Int. J. Electrochem. Sci.* **2018**, *8*, 1–15.

[27] Barbu, A.; Plichon, V. Voltammetry of thermally prepared ruthenium oxide films and flux detection at the electrolyte interface, *Electrochim. Acta* **1997**, *42*, 489–492.

[28] Bauer, B.; Gerner, F.J.; Strathmann, H. Development of bipolar membranes, *Desalination* **1988**, *68*, 279–292.

[29] Bazinet, A.; Lamarche, L.; Ippersiel, D. Bipolaire-membrane electrodialysis: application of electrodialysis in food industry, *Trends Food Sci. Technol.* **1998**, *9*, 107–113.

Declaration: This work has been published in the following journal:

Chemical Physics Letters 712 (2018) 160–164 Copyright. *Elsevier*

Chapter 3

Aqueous OH^-/H^+ Dual-ion Gradient Energy Assisted Electrochemical Device for Electricity Effective Desalination

Abstract

Integrating bifunctional applications in a single electrochemical device is highly desirable as it potentially enhance the electrical efficiency. We herein report a hybrid alkali-salt-acid electrochemical cell (h-ASAEC) that is capable of simultaneously implementing electrodesalination and H_2 generation in an electricity effective manner, by lowering the electrical energy input required for electrodesalination and H_2 generation, thanks to the electrical driving force of neutralization energy by virtue of the pH gradients in the three-compartment cell. The h-ASAEC at an electrolytic current density of 40 mA/cm^2 performs electrodesalination with minimal parasitic chemistry while generating ~33 ml/h of H_2 at a terminal voltage of ~1 V, which is only half of the voltage required in a symmetric configuration. Contrary to conventional desalination process, the low-voltage electrodesalination in h-ASAEC noticeably improves the energy efficiency and prevents competitive parasitic chemistry.

3.1 Introduction

This Chapter discusses how OH^-/H^+ dual-ion gradient energy can be harnessed to decrease the required input potential for electricity effective desalination. Due to the population explosion and rapid industrial growth around the globe, conventional water resources are no longer sufficient to meet the growing demand for drinking water.[1–6] In this aspect, seawater can be the ultimate solution as ~9.6 % of the water on the earth's crust is reserved in the oceans.[7–10] The presence of excess amount of salts in seawater (~3.5 wt % of NaCl) yet makes it impractical for everyday usage.[11–14] This has encouraged the researchers around the globe to look for efficient desalination technologies. Currently, reverse osmosis (RO) and thermal distillation are the widely used desalination techniques all over the world.[15–18] However, due to the high energy input required in the RO process, alternative electrochemical desalination strategies like capacitive deionization (CDI), electrodialysis (ED), solid battery electrodes (SBE) etc., have been explored.[19–22] A simple electrodialysis cell has a three-compartment architectural configuration containing neutral electrolyte with a cathodic half-cell, an anodic half-cell, and a middle compartment which holds the feed solution for desalination.[23–25] There are two major shortcomings for the traditional electrodialytic desalination process. On one hand, it suffers from large ohmic (iR) losses since the salt removal happens against the concentration gradient.[26–28] On the other hand, the OER occurring in the anodic half-cell has sluggish electrode

kinetics leading to serious energy losses. For these reasons, the minimum voltage required for electrodialysis at a reasonable rate is much larger than the thermodynamic voltage of water splitting (1.23 V).[29–31] Moreover, the proximity of chlorine evolution reaction (CER, 1.36 V vs. SHE) to OER (1.23 V vs. SHE) can also result in competitive CER at the anode.[29,32,33] This can contaminate the oxygen generating from the anodic compartment with consuming more electricity and may corrode the anode catalyst.

Another critical challenge in the 21st century is the global warming due to excessive use of non-renewable fossil fuel. H_2 generated via the water splitting powered by renewable energy resources, is a clean energy carrier molecule. However, hydrogen production via water splitting requires high input potential typically >1.23 V as it is a thermodynamically unfavourable reaction under ambient conditions,[34,35] which in fact derail the pathway towards a robust hydrogen economy. Therefore, it is imperative to design strategies and methodologies to generate molecular hydrogen in an electricity efficient way. It is to be noted that there are microbial electrodialysis devices which can perform simultaneous desalination and H_2 production,[36,37] however the microbial current generation is affected by the build-up chloride ion concentration in the anodic half-cell.

In this direction, we propose a hybrid alkali-salt-acid electrochemical cell (h-ASAEC) which can perform electrodesalination and H_2 production at a remarkably low electrical driving force compared to the

conventional electrodialysis cell, thanks to the contribution of electrochemical neutralization energy (ENE). This h-ASAEC has a OH^-/H^+ dual-ion gradient three-compartment architectural configuration with an anodic alkaline cell (OH^- solution), a middle compartment which holds the feed saline solution for desalination, and a cathodic acidic cell (H^+ solution), between which is separated by a cation exchange membrane (CEM) and an anion exchange membrane (AEM), as shown in Scheme 1. During the desalination, hydrogen evolution reaction (HER) and oxygen evolution reaction (OER) occur in the H^+ solution at cathode and the OH^- solution at anode respectively with concomitant desalination in the middle saline compartment. In this electrodesalination cell assisted by ENE, since HER and OER will be occurring respectively in H^+ and OH^- half-cells, the theoretical voltage required for the overall water splitting decreases from 1.23 V to 0.41 V.[38–40] Secondly, the sluggishness of chloride ion oxidation in alkaline media makes pH dependent OER more favorable on the electrocatalyst.[41–43] Hence, this h-ASAEC assisted by ENE on one hand, decreases the overall electrical energy input required for the desalination process, and on the other hand produce green fuel hydrogen at relatively lower potential. As a proof of concept, we further demonstrate h-ASAEC to desalinate highly saline sea water collected from the Arabian Sea and to produce H_2.

3.2 Experimental

3.2.1 Chemicals and Reagents

Chemicals required for the experiments such as sodium hydroxide (97%), sulphuric acid (98%), potassium hydrogen phosphate (98%), potassium phosphate (99%), acetic acid (99.7%), sodium acetate (99%), potassium sulphate (99%), nickel cobalt oxide, and sodium chloride were procured from Sigma-Aldrich India. Nafion@117 and Fumasep FAA-3-PK-130 membrane were also procured from Fuel Cell Store, USA.

3.2.2 Experimental Procedure

All electrochemical measurements were performed with the help of VMP 300 electrochemical workstation (Biologic, France). The fundamental electrochemistry of HER and OER reactions were carried out in a three-electrode setup, with $Ag/AgCl/Cl^-$ electrode as the reference electrode. Pt disk was served as the counter electrode and Pt and IrO_2 were used as the electrodes for HER and OER respectively. HER and OER reactions were performed in different pH solutions having pH = 0 (H_2SO_4), pH = 2 (sulphate buffer), pH = 4 (acetate buffer), pH = 6-12 (phosphate buffer) and pH = 14 (NaOH). Two compartment electrochemical cell was designed with a Nafion 117 membrane. The cathodic compartment was filled with 30 ml of 2 M H_2SO_4 solution whereas the anodic compartment was filled with 30 ml of 2 M NaOH solution. A Pt-mesh was used as the cathode for HER

reaction and nickel cobalt oxide coated on titanium mesh was used as the anode for OER reaction.

In a similar manner, a three-compartment cell was designed where the cathodic compartment was separated from the middle saline compartment by a cation exchange membrane (Nafion 117) and the anodic compartment was separated from the middle saline compartment by an anion exchange membrane (Fumasep FAA-3-PK-130). 30 ml of 2 M H_2SO_4 was used as catholyte and 30 ml of 2 M

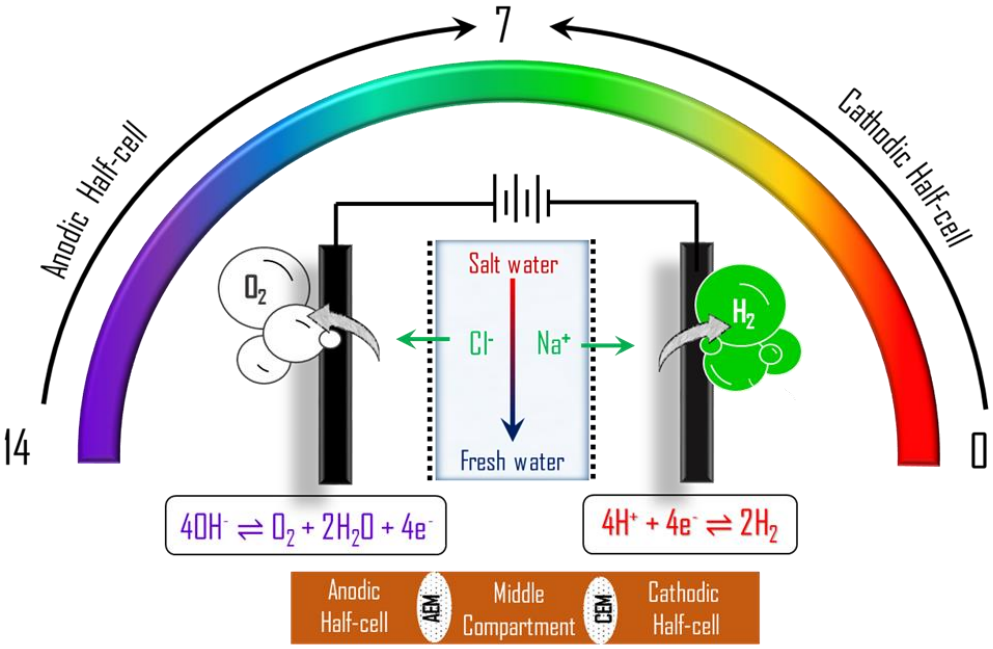

Scheme 1. Schematic representation of the h-ASAEC assisted by ENE.

NaOH was used as the anolyte. The middle saline compartment (desalination compartment) was filled with 8 ml of 3 M NaCl solution or 15ml of seawater. A Pt-mesh was used as the cathode for HER and nickel cobalt oxide coated on titanium mesh was used as anode for OER

reaction. Quantification of hydrogen and oxygen coming out from the cathodic and anodic compartments respectively was carried out by water displacement technique. The identity of hydrogen and oxygen was proved by in-situ electrochemical mass spectrometry (Hiden Analytical). The concentration of the catholyte (H_2SO_4) and the anolyte (NaOH) was estimated by acid-base titration method using oxalic acid as the primary standard. The concentration of sodium ion in the middle compartment was measured by microwave plasma atomic emission spectroscopy (MP-AES) technique (Agilent Technologies) and chloride ion concentration was measured by Mohr's titration method where silver nitrate was used as the titrant and potassium chromate was used as the indicator. Conductivity measurements were carried with µ controller-based conductivity meter (Type 306, Systronics India). The sea water used in the middle saline compartment for desalination was collected from the Arabian sea.

3.3. Results and discussion

The as-proposed h-ASAEC (Scheme 1) constitutes a three-compartment configuration with ion exchange membranes separating three different electrolytes. An electrical driving force is applied between a Pt electrode in H^+ electrolyte and a nickel cobalt oxide electrode in OH^- electrolytes. We have chosen Pt and nickel cobalt oxide as the electrocatalytic electrode because of their well-known capability in catalyzing HER and OER, respectively.[44,45] It should be pointed out that OH^-/H^+ dual-ion configuration can produce H_2 and O_2

in both half cells and drive Na^+ and Cl^- from the middle compartment to the respective half-cells (desalination) with the assistance of electrical driving force. Both HER and OER are the well-known pH-dependant reactions in water splitting half-cell. The voltammograms and Pourbaix diagrams demonstrate that they exhibit a pH dependence with a voltage shift of nearly 59 mV/pH, as revealed by (Figure 1a and 1b). Thermodynamically, HER in H^+ solution (pH= 0) occurs at E^0 = 0.0 V vs. SHE (Equation 1) while OER in OH^- solution (pH=14) occurs at E^0 = 0.41 V vs. SHE (Equation 2), respectively, leading to a required voltage of 0.41 V for hybrid alkali-acid electrolytic for H_2 and O_2 generation (Equation 3).

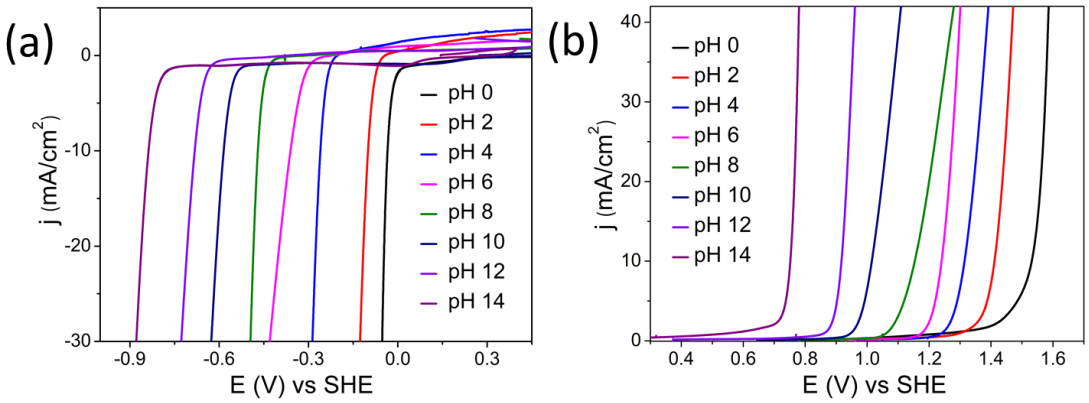

Figure 1. Linear sweep voltammograms for (a) hydrogen evolution reaction (HER) and (b) oxygen evolution reaction (OER) at different pH from pH = 0 to pH = 14.

This is further supported by Figure 2a and 2b, which suggest that, if HER is performed in H^+ solution while OER in OH^- solution by decoupling the direct acid alkali chemistry or in a OH^-/H^+ dual-ion

gradient electrolyte configuration, the electrical driving force (~0.7 V) required will be significantly lower than that (~1.5 V) required in a OH^- /OH^- single-ion electrolyte configuration.

$$4H^+(aq) + 4e^- \leftrightharpoons 2H_2(g) \qquad E^o = 0.00\ V \qquad (1)$$

$$4OH^-(aq) \leftrightharpoons O_2(g) + 2H_2O(l) + 4e^- \qquad E^o = 0.41\ V \qquad (2)$$

$$4H^+(aq) + 4OH^-(aq) \leftrightharpoons 2H_2(g) + O_2(g) + 2H_2O(l) \qquad E^o = 0.41\ V \qquad (3)$$

Therefore, the acid-base neutralization energy available in the OH^-/H^+ dual-ion gradient electrolyte configuration can be harvested for lowering the electrical driving force remarkably. This is demonstrated in Figure 2c with OH^-/H^+ dual-ion gradient electrolyte electrolytes which clearly show a noticeably lower onset voltage and a terminal voltage of ~1.1 V for achieving a current density of 100 mA/cm^2 (Figure 2c). To obtain the same current density from a water electrolyzer employing OH^-/OH^- single ion electrolytes with the same electrode architectures, a much higher voltage of ~2.0 V was required. As explained earlier, the thermodynamic potential difference between the OH^-/OH^- single ion and OH^-/H^+ dual-ion water electrolyzer is pH dependent and the value is ~0.8 V with $\Delta pH=14$ that is well consistent with the acid base neutralization energy. Therefore, the contribution of neutralization energy due to pH gradients is responsible for the overall decrease in electrical energy input in OH^-/H^+ dual-ion gradient electrolytes. In order to prove that decoupling of acid and base develop an inherent electromotive force between the half-cells, we have

monitored the electromotive force (EMF) in OH^-/OH^- single ion and OH^-/H^+ dual-ion electrolytes with two identical Pt electrodes (Figure 2d). The EMF was ~0.8 V in OH^-/H^+ dual-ion electrolytes which is

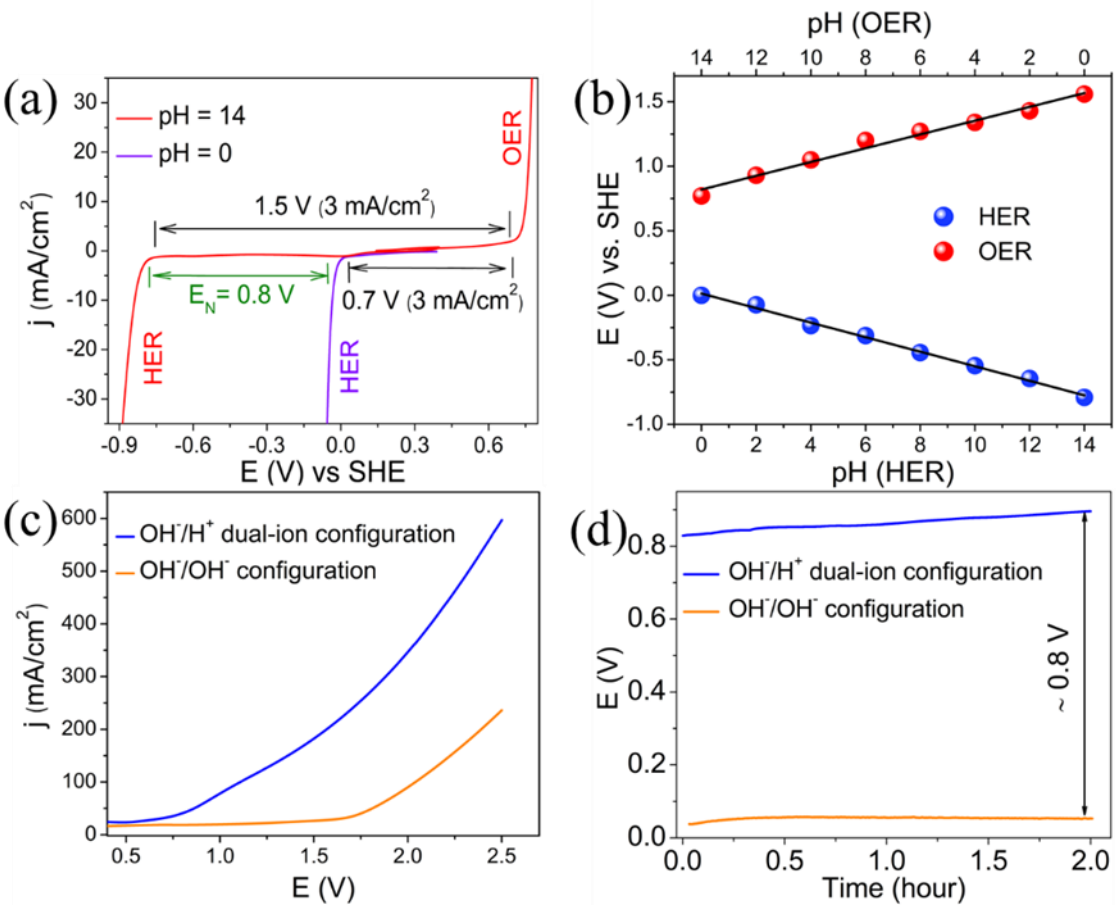

Figure 2 (a) Hydrogen evolution reaction (HER) in pH = 0 and pH = 14 electrolytes and oxygen evolution reaction (OER) in pH = 14 electrolyte and (b) Pourbaix diagram for water splitting half-cell reactions (HER and OER). (c) Current–voltage (I–V) curves for the OH^-/H^+ dual-ion and OH^-/OH^- single ion water electrolyzers and (d) open-circuit voltage vs time plots in OH^-/H^+ dual-ion and OH^-/OH^- single ion electrolyte configurations using two identical Pt electrodes. close to the thermodynamic potential for acid base neutralization (Calculation 1).

It should be noted that in OH^-/OH^- single ion electrolyte configuration the EMF was close to zero indicating that energy of neutralization can be harvested as electromotive force only in the OH^-/H^+ dual-ion electrolyte configuration.

Calculation 1

OH^-/OH^- Single-ion Electrolyte

Cathode electrode: $4H^+(aq) + 4e^- \rightarrow 2H_2(g)$ $E^o = 0.0$ V

Anode electrode: $4H_2O\ (l) \rightarrow O_2(g) + 4H^+ + 4e^-$ $E^o = 1.23$ V

$$4H_2O\ (l) \rightarrow 2H_2\ (g) + O_2\ (g)\ E^o = -1.23\ V \ldots\ldots (1)$$

OH^-/H^+ dual-ion Electrolyte

Cathode electrode: $4H^+(aq) + 4e^- \rightarrow 2H_2\ (g)$ $E^o = 0.0$ V

Anode electrode: $4OH^-\ (aq) \rightarrow O_2\ (g) + 2H_2O\ (l) + 4e^-$ $E^o = 0.41$ V

$$4H^+\ (aq) + 4OH^-\ (aq) \rightarrow 2H_2\ (g) + O_2\ (g) + 2H_2O\ (l) \quad E^o = -0.41\ V \ldots\ldots (2)$$

Equation (2) - Equation (1)

$$4H^+\ (aq) + 4OH^-\ (aq) \rightarrow 2H_2\ (g) + O_2\ (g) + 2H_2O\ (l) \quad E^o = -0.41\ V$$

$$4H_2O\ (l) \rightarrow 2H_2\ (g) + O_2\ (g) \quad E^o = -1.23\ V$$

$$4H^+\ (aq) + 4OH^-\ (aq) \rightarrow 2H_2O\ (l)$$

$$E^o = (-0.41\ V) - (-1.23\ V) = 0.82\ V \ldots\ldots (3)$$

Enthalpy change during Neutralization:

$\Delta H^o = 4*H^o\ (H_2O) - 4*H^o\ (OH^-) - 4*H^o\ (H^+)$

$= 4*(285.83\ kJ) - 4*(-229.99\ kJ) - 4*0$

$= -223.36\ kJmol^{-1}$

Entropy change during Neutralization:

$\Delta S^o = 4*S^o (H_2O) – 4*S^o (OH^-) – 4*S^o (H^+)$

$= 4*69.91 – 4*(-10.75) - 4*0$

$= 322.64\ JT^{-1}mol^{-1}$

Free energy change during Neutralization:

$\Delta G^o = \Delta H^o - T\Delta S^o$

$= -223.36\ kJmol^{-1} – (298\ T * 322.64\ JT\text{-}1mol^{-1})$

$= -319.50\ kJmol^{-1}$

$E^o = - \Delta G/nF$

$= -319.50\ kJmol^{-1}\ 4*96500\ C\ mol^{-1}$

$= 0.82\ V$

Galvanostatic polarization demonstrates that at the same current density, the voltage required by the OH^-/OH^- single ion water electrolyzer is twice higher compared to OH^-/H^+ dual-ion electrolyzer (Figure 3a). All these suggest that by utilizing OH^-/H^+ dual-ion electrolytes, energy of neutralization can be harvested as electromotive force only in the OH^-/H^+ dual-ion electrolyte configuration. In the OH^-/H^+ dual-ion electrolyte configuration, the identity of the gaseous species is proved to be hydrogen and oxygen from cathodic and anodic half cells respectively by in-situ electrochemical mass spectrometry (Figure 3b).

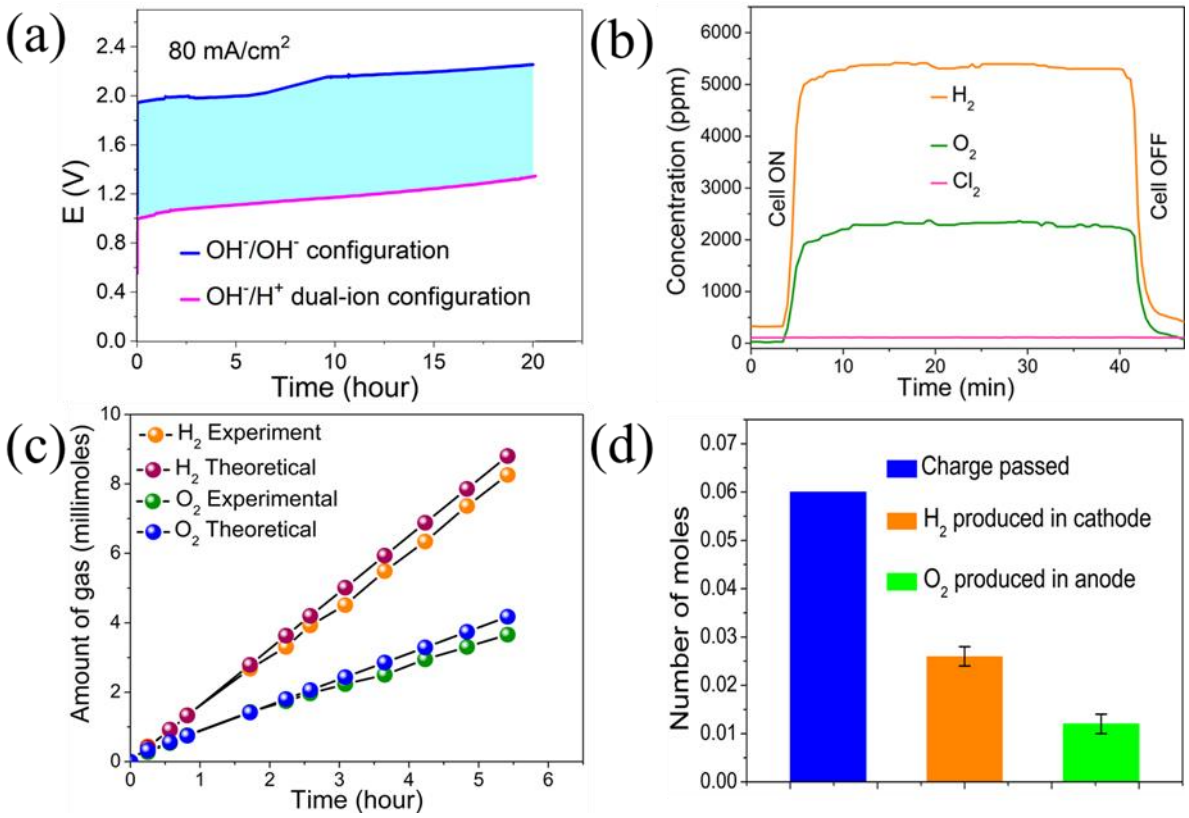

Figure 3 (a) Chronopotentiometry of OH^-/H^+ dual-ion and OH^-/OH^- single ion water electrolyzer at 80 mA/cm^2 for 20 hours, (b) in-situ electrochemical mass spectrometry of cathodic and anodic species of OH^-/H^+ dual-ion water electrolyzer at 80 mA/cm^2, (c) quantification of gaseous species evolved at the cathode and the anode of the OH^-/H^+ dual-ion water electrolyzer at 80 mA/cm^2 and (d) the amount of charge passed vs. moles of H_2 and O_2 evolved respectively at the cathode and the anode of the asymmetric water electrolyzer at 80 mA/cm^2 for 20 hours.

We have carried out the quantification of gaseous species emanating from the half cells of the OH^-/H^+ dual-ion water electrolyzer at a current density of 80 mA/cm^2 by collecting the gases in calibrated cylinders

using water displacement technique (Figure 3c). As expected, the amount of hydrogen is twice that of oxygen and the amount of hydrogen and oxygen produced is in line with the amount of charge passed during electrolysis, suggesting almost 100% Faradaic efficiency for H_2 and O_2 generation (Figure 3d). This electrochemical device assisted by ENE is further utilized to perform simultaneous electrodesalination in a hybrid alkali-salt-acid electrochemical cell (h-ASAEC).

According to the current voltage (I-V) polarization curves (Figure 4a), the h-ASAEC can reach a current density of 40 mA/cm^2 at an applied voltage of only ~1.0 V, obviously outperforming the OH^-/OH^- single ion alkali-salt-alkali electrochemical cell (ASAEC) which demands a corresponding voltage of 1.9 V, as illustrated in Figure 3a. During the constant current test at 40 mA/cm^2 as shown in Figure 4b, we have identified and quantified the gaseous species emanating from the half cells of h-ASAEC and also monitored the extent of water desalination in the middle chamber. The identification and quantification of the gaseous species suggest that hydrogen amount is twice as that of oxygen with nearly 100% Faradic efficiency for both anodic OER and cathodic HER (Figure 4c and Figure 4d). After 15 hours' operation of h-ASAEC at 40 mA/cm^2, the sodium ion concentration in the middle saline compartment significantly decreased to ~21 g/L from 175 g/L, as confirmed by microwave plasma atomic emission spectroscopy (MP-AES) analysis (Figure 5a).

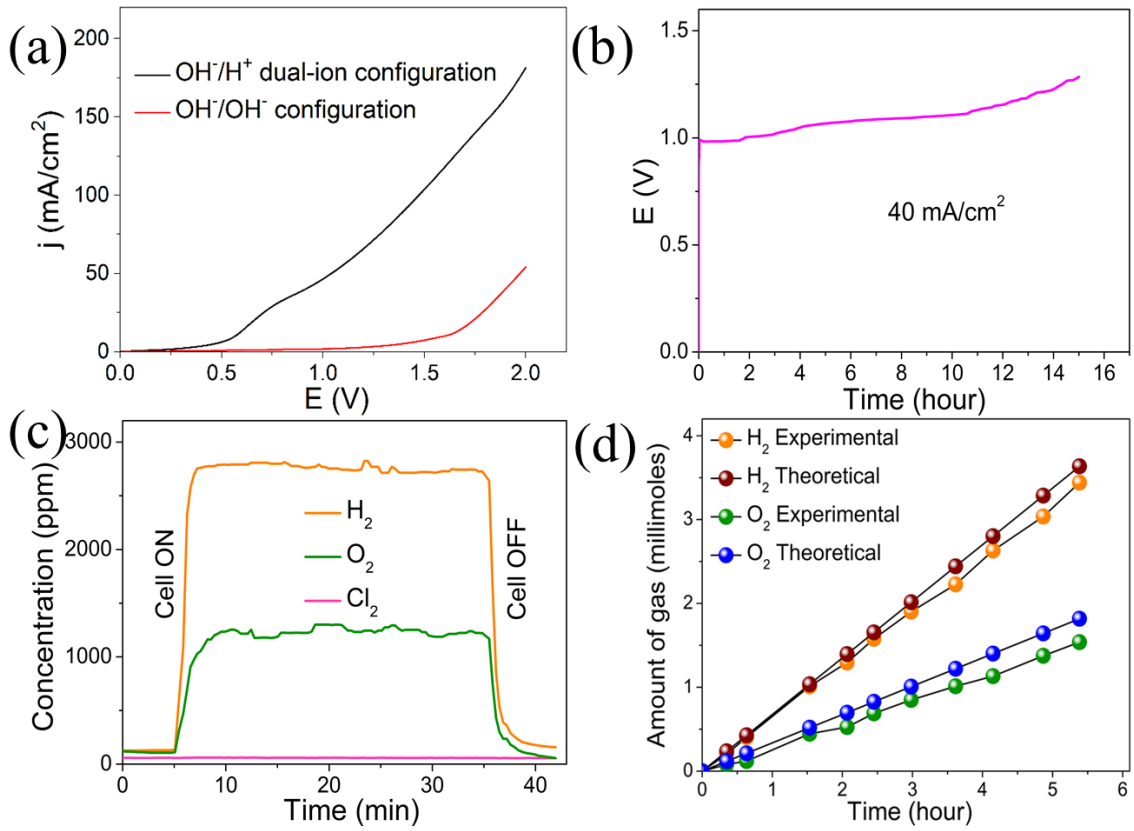

Figure 4 (a) Current−voltage (I−V) curves for the h-ASAEC. (b) Chronopotentiometry of the h-ASAEC cell at 40 mA/cm^2 current density for 15 h. (c) In situ electrochemical mass spectrometry of evolved cathodic and anodic species at 40 mA/cm^2. (d) Quantification of evolved gaseous species at the cathode and anode at 40 mA/cm^2 current density.

Precipitation titration with $AgNO_3$ (Mohr's method) was used to follow chloride ion concentration in the saline compartment, which revealed a decrease in chloride ion concentration commensurate to Na^+ ion decrease (Figure 5a). These suggest a removal of ~154 g of NaCl from the middle saline compartment in the h-ASAEC. Further, the

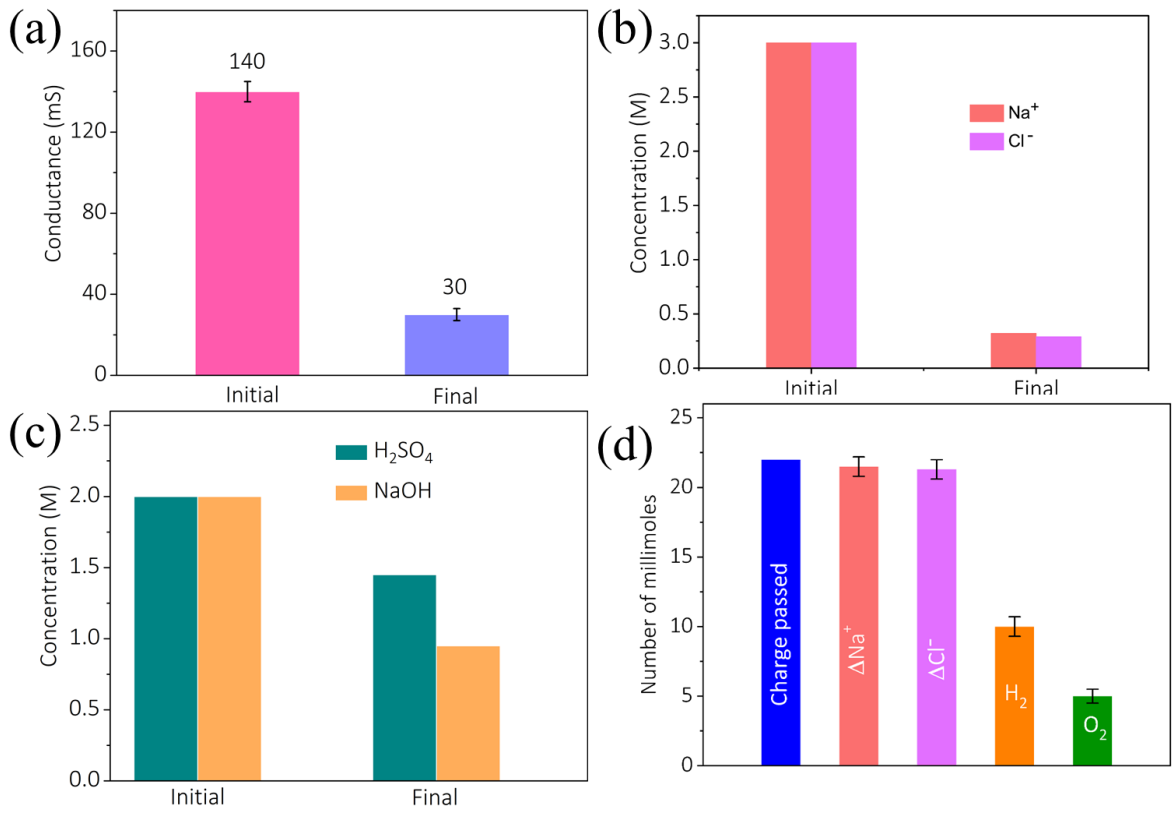

Figure 5 (a) Conductance measurement of saline compartment before and after long term polarization (b) Change in concentration of Na^+ and Cl^- in the middle saline compartment after desalination for 15 h. (c) concentration of H_2SO_4 in the cathodic half-cell and NaOH in the anodic half-cells before and after long term polarization. (d) Amount of charge passed vs moles of Na^+ and Cl^- removed (from the desalination compartment) and the moles of H_2 (cathode) and O_2 (anode) produced at 40 mA/cm^2 for 15 h.

conductance in the middle compartment decreased from ~140 mS to ~30 mS after 15 hours running (Figure 5b), additionally confirming the desalination process. During constant current polarization at 40 mA/cm^2, the concentration of H^+ in the cathodic half-cell and OH^- in

the anodic half-cell were decreased, (Figure 5c), suggesting the consumption of acidic and alkaline species in the overall process. As shown in Figure 5d, the charge passed during galvanostatic desalination is well correlated to the amount of H_2 and O_2 produced at the half-cells and the amount of NaCl removed from the saline compartment. At the open circuit conditions of h-ASAEC, the changes in salt concentrations in the middle saline compartments were negligibly small for almost 15 hours, suggesting that the contribution of diffusion driven desalination is negligible (Figure 6a, b). All these evidence that such h-ASAEC device, thanks to the assistance of ENE, is capable for both electrolytic desalination and H_2 generation at a relative low voltage. The amount of energy spent for desalination is extracted by comparing the current-voltage curves with and without the desalination compartment (Figure 7a) the shaded portion represents the energy consumption during the desalination process (calculation 2).

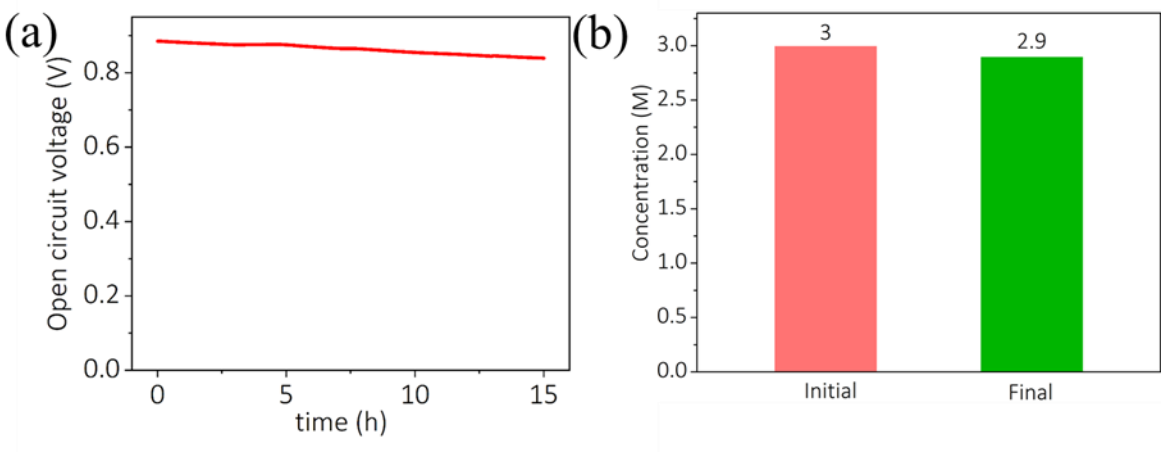

Figure 6. (a) Open circuit voltage of hybrid alkali-salt-acid electrochemical cell (h-ASAEC) for 15 hours. (b) Concentration of

ions in the desalination compartment when the h-ASAEC is kept at the open circuit voltage for 15 hours.

The electrical energy efficiency of the electrodialysis process assisted by ENE is compared with state-of-the-art methods for desalination (Figure 7b).

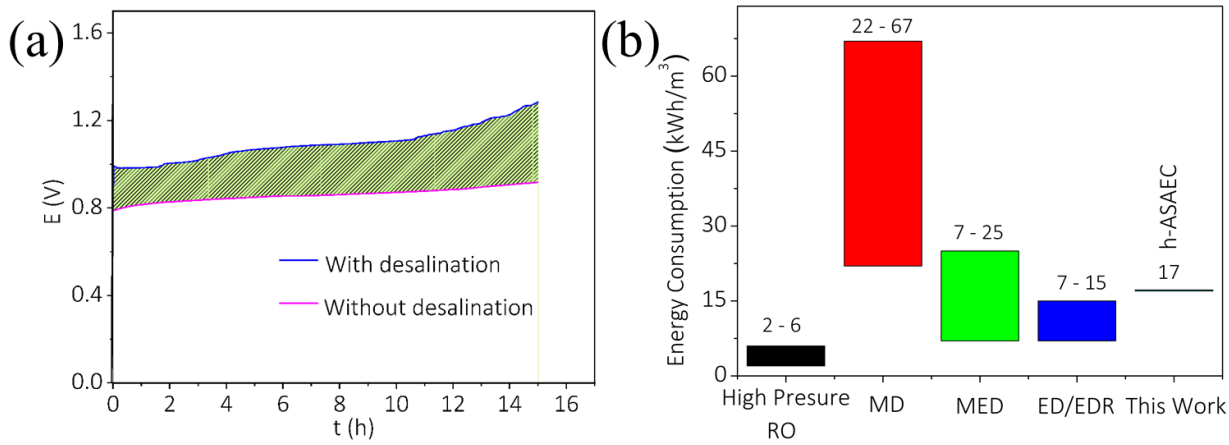

Figure 7 (a) Chronopotentiometry of the device with and without the saline middle compartment. (d) Energy efficiency comparison of the h-ASAEC with the state-of-the-art electrochemical desalination techniques.[44,45]Concentrations of NaCl were ~200 g/L (~3.4 M) for MD, MED, and ED/EDR and ~78 g/L (~1.3 M) for high-pressure RO.

Calculation 2

Area of the shaded portion in Figure 7(a) = 3.52 V.h = 12,672 V.s
Change in moles of NaCl in saline compertment = 21.6 mmol.

Energy efficiency (kJ/mol)

$$= area \times applied\ current\ change\ in\ mol$$

= $12672 V.s \times 0.04\ A\ 0.0216\ mol$

= 23,466.66 J/mol

= 23 kJ/mol

Energy efficiency (kWh/m3)

= $area \times applied\ current\ Volumn\ of\ feed\ solution$

= $12672 V.s \times 0.04\ A\ 8ml$

= 17 kWh/m3

It is observed that in h-ASAEC with 3 M NaCl in the middle compartment, the electrical energy spent on desalination is ~17 kWh/m^3 (~23 kJ/mol) of feed water. A comparison with other desalination methods like high pressure RO, membrane desalination (MD), multi-effect distillation (MED), electrodialysis (ED) or electrodialysis reversal (EDR), show that the energy efficiency values of h-ASAEC is comparable to ED/EDR.[45,46] Overall, the half-cell reactions and the overall cell reaction for desalination in h-ASAEC are as shown in equations 4 to 6.

Cathodic half-cell:

$4H^+(aq) + 4e^- + Na^+(MC) \rightarrow 2H_2(g) + Na^+(CC)$ $E^o_{cathode} = 0.0$ V … (4)

Anodic half-cell:

$4OH^-(aq) + Cl^-(MC) \rightarrow O_2(g) + 2H_2O(l) + 4e^- + Cl^-(AC)$ $E^o_{anode} = 0.4$ V (5)

$$4H^+(aq) + 4OH^-(aq) + Na^+(MC) + Cl^-(MC) \rightarrow 2H_2(g) + O_2(g) + 2H_2O(l) + Na^+(CC) + Cl^-(AC)$$

$$E^o_{cell} = -0.41\ V \qquad (6)$$

where, MC represents the middle compartment, whereas CC and AC are the cathodic and anodic compartments respectively. The energy balance calculation for the overall reaction in h-ASAEC demonstrates an energy efficiency of 0.85 (Calculation S4, Supporting Information), and out of these ~17 kwh/m^3 (~23 kJ/moles) is spend for the desalination process, Figure 3d.

In order to demonstrate the practical application of such proof-of-concept, we have carried out the desalination of sea water collected from the Arabian Sea with the help of h-ASAEC. The I-V characteristics in (Figure 8a) suggest the performance is almost similar to the above h-ASAEC with NaCl solution (175 g/L) in the middle saline compartment. After running at 40 mA/cm^2 for 6 hours (Figure 8b), detection of evolved gaseous species is performed with in-situ mass spectrometry, which suggests that there is concomitant HER and OER in the cathodic and anodic half cells respectively with nearly 100% of Faradaic efficiency (Figure 8 c). All these evidence that the h-ASAEC is capable for simultaneous seawater desalination and hydrogen generation at remarkably low electrical driving force. MP-AES of sea water demonstrate the presence of Na^+, Mg^{2+}, K^+ and Ca^{2+} ions as the major components, and their concentrations decreased noticeably during galvanostatic polarization at 40 mA/cm^2 (Figure 8d).

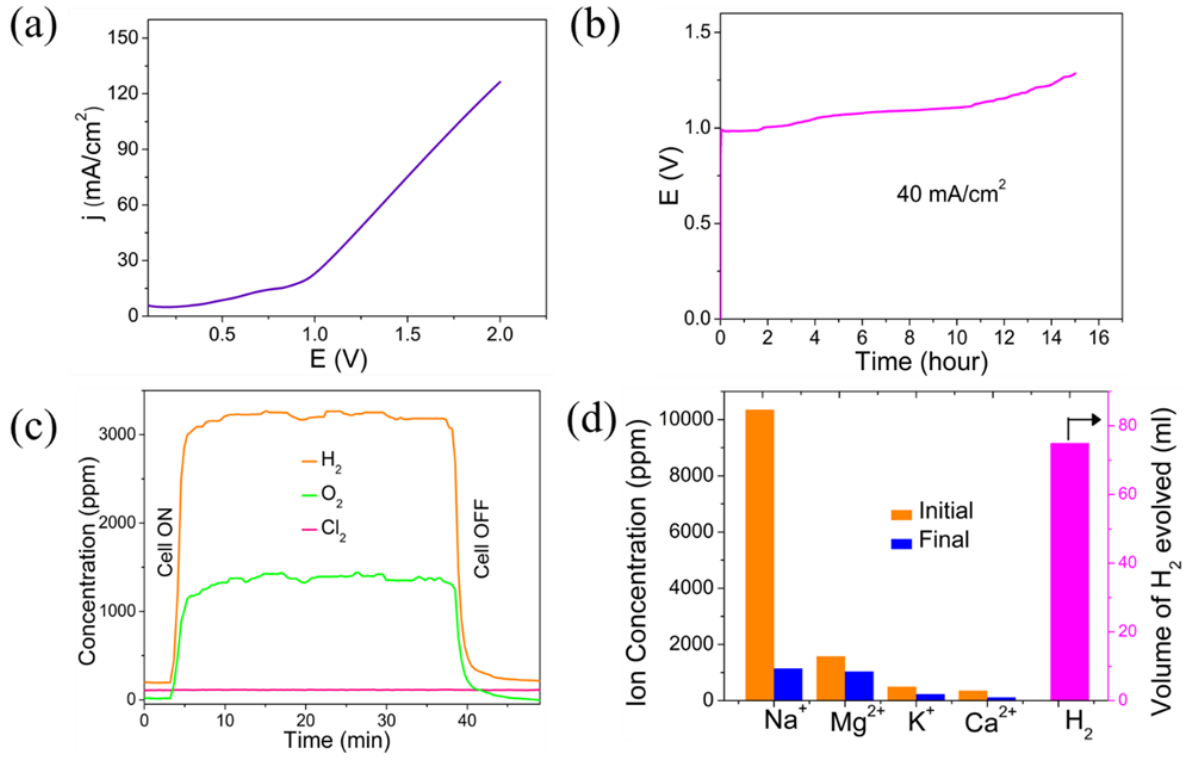

Figure 8 (a) Current-voltage (I-V) curves of h-ASAEC for the desalination of Arabian sea water. (b) Chronopotentiometry for the h-ASAECcell for the desalination of Arabian seawater. (c) In situ electrochemical massspectrometry of the evolved cathodic and anodic species and (d) Na^+, Mg^{2+}, K^+, and Ca^{2+} ion concentrations obtained from MP-AES analysis when the middle compartment of the h-ASAEC housed seawater from Arabian Sea and the amount of H_2 released after 6 h.

4. Conclusion

We have demonstrated the design of a novel electrochemical neutralization cell for simultaneous electrodesalination and hydrogen generation. Compared to the conventional electrodialysis cell hybrid

alkali-salt-acid electrochemical cell can perform electrodesalination and H_2 production at a low electrical driving force. Moreover, in h-ASAEC pure oxygen is evolved from the anodic compartment, whereas in conventional elctrodialysis cell Cl_2 gas can be present as an impurity. One of the disadvantages of h-ASAEC is that, both acid and alkali are required as electrolytes which will be consumed during the desalination process. Nevertheless, the overall cost efficiency in h-ASAEC is compensated by the lower electrical energy input. A second disadvantage of h-ASAEC is related to recyclability of the device since the acid cathode and the alkaline anode are independent of the intermediate salt chamber. Since, corrosive electrolytes are used in h-ASAEC, Pt instability issues including carbon corrosion and Pt leaching can be encountered in acidic and alkaline electrolytes and this can be addressed by careful engineering of electrocatalysts.[47,48] Nevertheless, the proposed device requires a significantly low voltage compared to state of the art electrodialysis process, as the desalination occurs in the direction of pH gradients which in turn improves the energy efficiency and arrests the parasitic chemistry at the cathode. The h-ASAEC involves gaseous products at separated electrodes which prevent the poisoning of the desalinated water. h-ASAEC requires nearly 23 kJ to remove 1 mole of salt from the saline water which is lower than the state-of-the-art desalination processes. The proposed ENE cell design opens up novel pathways for integrating multiple functionalities in single devices, which leads to new design strategies for future generation energy storage and conversion devices.

5. References

[1] Mekonnen, M. M.; Hoekstra, A. Y. Four billion people facing severe water scarcity. *Sci. Adv.* **2016**, *2*, e1500323.

[2] Wang, J.; Lu, J.; Zhou, Y.; Zhou, Y. Multifunctional Antibacterial Materials for the Control of Hazardous Microbes and Chemicals: A Review. *ACS EST Water*, **2021**, 1, 479–497.

[3] Huang, Y.; Zhu, M.; Huang, Y.; Pei, Z.; Li, H.; Wang, Z.; Xue, Q.; Zhi, C. Multifunctional energy storage and conversion devices. *Adv. Mater.* **2016**, *28*, 8344–8364.

[4] Zhu, Y.; Zhang, J.; Qian, Q.; Li, Y.; Li, Z.; Liu, Y.; Xiao, C.; Zhang, G.; Xie, Y. Dual Nanoislands on Ni/C Hybrid Nanosheet Activate Superior Hydrazine Oxidation-Assisted High-Efficiency H_2 Production. *Angew. Chem. Int. Ed.* **2022**, *61*, e202113082.

[5] Elimelech, M.; Phillip,W.A.; The future of seawater desalination: Energy, Technology, and the Environment. *Science*, **2011**, *333*, 6043, 712–717.

[6] Ferreyra, N.; Coche-Guérente, L.; Fatisson, J.; Lopez Teijelo, M.; Labbé, P. Layer-by-Layer Self-Assembled Multilayers of Redox Polyelectrolytes and Gold Nanoparticles. *Chem. Commun*. **2003**, 2056–2057.

[7] Bąbel, M.; Schreiber, B. C.; Geochemistry of Evaporites and Evolution of Seawater, **2014**, volume 9, 483–560.

[8] Hallsworth, J. E.; Yakimov, M. M.; Golyshin, P. N.; Gillion, J. L. M.; D'Auria, G.; Alves, F. D. L.; Cono, V. L.; Genovese, M.; Mckew, B. A.; Hayes, S. L.; Harris, G.; Giuliano, L.; Timmis, K. N.; McGenity, T. J. Limits of Life in $MgCl_2$ Containing Environments: Chaotropicity Defines the Window. *Environmental Microbiology*, **2007**, *9*, 801–813.

[9] Schafzahl, L.; Mahne, N.; Schafzahl, B.; Wilkening, M.; Slugovc, C.; Borisov, S. M.; Freunberger, S. A. Singlet Oxygen during Cycling of the Aprotic Sodium–O_2 Battery. *Angew. Chem. Int. Ed*. **2017**, *56*, 15728–15732.

[10] Cavaliere, S.; Subianto, S.; Savych, I.; Jones, D. J.; Rozière, J. Electrospinning: Designed Architectures for Energy Conversion and Storage Devices. *Energy Environ. Sci.* **2011**, *4*, 4761–4785.

[11] Liu, Z.; Wu, B.; Zhu, B.; Chen, Z.; Zhu, M.; Liu, X. Continuously Producing Watersteam and Concentrated Brine from Seawater by Hanging Photothermal Fabrics under Sunlight. *Adv. Funct. Mater.* **2019**, *29*, 1905485.

[12] Shannon, M. A.; Bohn, P. W.; Elimelech, M.; Georgiadis, J. G.; Marinas, B. J.; Mayes, A. M. Science and Technology for Water Purification in the Coming Decades. *Nature*, **2008**, *452*, 301–310.

[13] Lee, J.; Srimuk, P.; Zwingelstein, R.; Zornitta, R. L.; Choi, J.; Kim, C.; Presser, V. Sodium Ion Removal by Hydrated Vanadyl Phosphate for Electrochemical Water Desalination. *J. Mater. Chem. A*, **2019**, *7*, 4175–4184.

[14] Hassoun, J.; Scrosati, B. Review — Advances in Anode and Electrolyte Materials for the Progress of Lithium-Ion and beyond Lithium-Ion Batteries. *J. Electrochem. Soc*. **2015**, *162*, 14, A2582–A2588.

[15] Lumley, M. A.; Nam, D.; Choi, K. Elucidating Structure−Composition−Property Relationships of Ni-Based Prussian Blue Analogues for Electrochemical Seawater Desalination. *ACS Appl. Mater. Interfaces.* **2020**, *12*, 36014–36025.

[16] Ghaffour, N.; Missimer, T. M.; Amy, G. L. Technical Review and Evaluation of the Economics of Water Desalination: Current and Future Challenges for Better Water Supply Sustainability. *Desalination* **2013**, 309, 197−207.

[17] Saadat, A. H. M.; Islam, M. S.; Islam, M. S.; Parvin, F.; Sultana, A. Desalination Technologies for Developing Countries: A Review. *J. Sci. Res.* **2018**, *10*, 1, 77−97.

[18] Missimer, T. M.; Maliva, R. G. Environmental Issues in Seawater Reverse Osmosis Desalination: Intakes and Outfalls. *Desalination*, **2018**, *434*, 198−215.

[19] Anderson, M. A.; Cudero, A. L.; Palma, J. Capacitive Deionization as an Electrochemical Means of Saving Energy and Delivering Clean Water. Comparison to Present desalination practices: Will it compete? *Electrochim. Acta.* **2010**, *55*, 3845−3856.

[20] Porada, S.; Zhao, R.; Van Der Wal, A.; Presser, V.; Biesheuvel, P. M. Review on the Science and Technology of Water Desalination by Capacitive Deionization; *P. Mat. Sci.* **2013**, 58, 1388–1442.

[21] Oren, Y. Capacitive Deionization (CDI) for Desalination and Water Treatment — Past, Present and Future (a Review). *Desalination*, **2008**, 228, 10–29.

[22] Mourad, E.; Coustan, L.; Lannelongue, P.; Zigah, D.; Mehdi, A.; Vioux, A.; Freunberger, S. A.; Favier, F.; Fontaine, O. Biredox Ionic Liquids with Solid-like Redox Density in the liquid state for high-energy supercapacitors; *Nat. Mater.* **2017**, *16*, 446–453.

[23] Patel, S. K.; Biesheuvel, P. M.; Elimelech, M. Energy Consumption of Brackish Water Desalination: Identifying the Sweet Spots for Electrodialysis and Reverse Osmosis. *ACS EST Engg.* **2021**, *1*, 851−864.

[24] Yan, H.; Xu, C.; Li, W.; Wang, Y.; Xu, T. Electrodialysis to Concentrate Waste Ionic Liquids: Optimization of Operating Parameters. *Ind. Eng. Chem. Res*. **2016**, *55*, 2144–2152.

[25] Patel, S. K.; Qin, M.; Walker, W. S.; Elimelech, M. Energy Efficiency of Electro-Driven Brackish Water Desalination: Electrodialysis Significantly Outperforms Membrane Capacitive Deionization. *Environ. Sci. Technol.* **2020**, *54*, 3663–3677.

[26] Vermaas, D. A.; Veerman, J.; Yip, N. Y.; Elimelech, M.; Saakes, M.; Nijmeijer, K. High Efficiency in Energy Generation from Salinity

Gradients with Reverse Electrodialysis. *ACS Sustainable Chem. Eng.* **2013**, 1, 1295–1302.

[27] Moreno, J.; Grasman, S.; Engelen, R. V.; Nijmeijer, K. Upscaling Reverse Electrodialysis. *Environ. Sci. Technol*. **2018**, *52*, 10856–10863.

[28] Kim, D.; Amy, G. L.; Karanfil, T. Disinfection by-product Formation during Seawater Desalination: A Review. *Water Res.* **2015**, *81*, 343–355.

[29] Nam, D.; Lumley, M. A.; Choi, K. Electrochemical Redox Cells Capable of Desalination and Energy Storage: Addressing Challenges of the Water–Energy Nexus. *ACS Energy Lett.* **2021**, *6*, 3, 1034–1044.

[30] Severin, B. F.; Hayes, T. D. Effect of Electrode Rinse Solutions on the Electrodialysis of Concentrated Salts. *Sep. Purif. Technol.* **2021**, *274*, 119048.

[31] Veerman, J.; Saakes, M.; Metz, S. J.; Harmsen, G. J. Reverse Electrodialysis: Evaluation of Suitable Electrode Systems; *J. Appl. Electrochem.* **2010**, *40*, 1461–1474.

[32] Nam, D.; Choi, K. Tandem Desalination/Salination Strategies Enabling the Use of Redox Couples for Efficient and Sustainable Electrochemical Desalination. *ACS Appl. Mater. Interfaces*, **2019**, *11*, 38641–38647.

[33] Nam, D.; Choi, K. Electrochemical Desalination Using Bi/BiOCl Electrodialysis Cells. *ACS Sustainable Chem. Eng.* **2018**, 6, 15455–15462.

[34] Carmo, M.; Fritz, D. L.; Mergel, J.; Stolten, D. A Comprehensive Review on PEM Water Electrolysis. *Int. J. Hydrog. Energy*, **2013**, 38, 4901–4934.

[35] Shiva Kumar, S.; Himabindu, V. Hydrogen Production by PEM Water Electrolysis – A Review. *Materials Science for Energy Technologies*, **2019**, 2, 442–454.

[36] Mehanna, M.; Kiely, P. D.; Call, D. F.; Logan, B. E. Microbial Electrodialysis Cell for Simultaneous Water Desalination and Hydrogen Gas Production. *Environ. Sci. Technol.* **2010**, 44, 9578–9583.

[37] Khalla, S. A.; Atlas, I.; Litster, S.; Suss, M. E. Desalination Fuel Cells with High Thermodynamic Energy Efficiency. *Environ. Sci. Technol.* **2022**, 56, 1413–1422.

[38] Ding, Y.; Cai, P.; Wen, Z. Electrochemical Neutralization Energy: From Concept to Devices. *Chem. Soc. Rev.* **2021**, *50*, 1495–1511.

[39] Cavaliere, S.; Subianto, S.; Savych, I.; Jones, D. J.; Roziere, J. Electrospinning: Designed Architectures for Energy Conversion and Storage Devices. *Energy Environ. Sci.* **2011**, *4*, 4761–4785.

[40] Anantharaj, S.; Noda, S. Amorphous Catalysts and Electrochemical Water Splitting: An Untold Story of Harmony. *Small*, **2020**, *16*, 1905779.

[41] Karlsson, R. K. B.; Cornell, A. Selectivity between Oxygen and Chlorine Evolution in the Chlor-Alkali and Chlorate Processes. *Chem. Rev.* **2016**, *116*, 2982–3028.

[42] Chen, Z.; Duan, X.; Wei, W.; Wang, S.; Ni, B. Iridium-Based Nanomaterials for Electrochemical Water Splitting. *Nano Energy*, **2020**, *78*, 105270.

[43] Dionigi, F.; Reier, T.; Pawolek, Z.; Gliech, M.; Strasser, P. Design Criteria, Operating Conditions, and Nickel – Iron Hydroxide Catalyst Materials for Selective Seawater Electrolysis. *ChemSusChem*, **2016**, *9*, 962–972.

[44] Cheng, Y.; Jiang, S. P. Advances in Electrocatalysts for Oxygen Evolution Reaction of Water Electrolysis–from Metal Oxides to Carbon Nanotubes. *Prog. Nat. Sci. Mater.* **2015**, *25*, 545–553.

[45] D. Zhao, L. Yoke Lee, S. Leong Ong, P. Chowdhury, K. Boon Siah, H. Yong Ng, Electrodialysis Reversal for Industrial Reverse Osmosis Brine Treatment, *Separation and Purification Technology*. **2018**, *213*, 339-347

[46] T. Tong, M. Elimelech, The Global Rise of Zero Liquid Discharge for Wastewater Management: Drivers, Technologies, and Future Directions, *Environ. Sci. Technol*. 50 (2016) 6846-6855.

[47] Zadick, A.; Dubau, L.; Sergent, N.; Berthome, G.; Chatenet, M. Huge Instability of Pt/C Catalysts in Alkaline Medium. *ACS Catal.* **2015**, *5*, 4819–4824.

[48] Bagotzky, V. S.; Khrushcheva, E. I.; Tarasevich, M. R.; Shumilova, N. A. Corrosion of Platinum Catalyst in Alkaline Solutions. *J. Power Sources*, **1982**, *8*, 301–309.

Declaration: This work has been published in the following journal:

ACS Sustainable Chem. Eng. 2022, 10,10781–10788 Copyright. ACS

Chapter 4

Aqueous OH^-/H^+ Dual-ion Gradient Energy Assisted Photoelectrochemical Water Splitting

Abstract

Photoelectrochemical (PEC) water splitting is an emerging technology to store the solar energy in the chemical bonds of molecular hydrogen. Among several photo electrodes used for PEC water splitting, α-Fe_2O_3 is a promising material due to its suitable bandgap, chemical stability, and abundance. Despite these, the position of its conduction band does not allow spontaneous movement of photo-generated electrons to cause the water reduction. This demands the application of a minimum electrical bias of ~1.5 V vs. SHE to increase the energy of the conduction band such that it will be energetically above the H_2O/H_2 redox level. We show that by utilizing the energy of neutralization, the minimum electrical voltage required for PEC water splitting can be brought down to ~0.8 V by employing an OH^-/H^+ dual-ion configuration. OH^-/H^+ dual-ion assisted PEC water splitting required only 0.95 V to produce a current density of 10 mA/cm^2, and for achieving the same rate in a conventional symmetric ion configuration required at least a doubling a applied electrical bias (~1.8 V).

1. Introduction

In this chapter the OH^-/H^+ dual-ion gradient energy assists to reduce the required potential for photoelectrochemical water splitting. Harvesting solar energy by photoelectrochemical (PEC) water splitting and storing that in the chemical bonds of molecular hydrogen is a promising approch.[1-3] as it combines the dual functions of a solar cell and a water electrolyzer in a single divice.[4-6] In 1972 Honda and Fujishima first reported photoelectrochemical water splitting using TiO_2 as the photoanode and Pt as the cathode.[7,8] In principle, when a semiconductor photo electrode immersed in an electrolyte is illuminated with light, electron and hole pairs will be generated and get separated due to presence of internal electric field.[9,10] Electrons from the conduction band (for n-type semiconductor) are drifted towards the counter electrode where they involve in the water reduction half-cell reaction.[11,12] While the holes in valence band participate in the oxidation half-cell reaction in the semiconductor electrolyte interface to generate molecular O_2.[13-15] In these contexts, selection of a suitable semiconductor for absorbing light is an important part for constructing a photoelectrochemical (PEC) device. Semiconductor electrode should be sufficiently stable in aqueous solution, it should have suitable band gap for absorbing visible range of the solar spectrum, and the band edge positions should be such that it should be able to split water molecules spontaneously on illumination.[16-19] Several n-type semiconductors like $BiVO_4$, WO_3, Fe_2O_3, TiO_2 etc., are used as a photo anodes in photo

assisted water spelling reaction.[20-22] Among them, hematite (α-Fe_2O_3) is widely used as the photo anode in PEC water splitting because of its low band gap (1.9 eV to 2.1 eV) for absorbing the visible range of the solar spectrum, excellent chemical stability in a wide range of pH, nontoxicity and natural abundance.[23-27] Despite these promising aspects for using it as the photo anode, several limitations need to be addressed. Importantly, hematite has inherently slow surface reaction kinetics due to a very short excited-state lifetime which combined with the high overpotential for water splitting in the conventional symmetric ion configuration, noticeably decrease the electrical efficiency of PEC water splitting.[28,29]This high overpotential is due to the location of hematite's conduction band energy, which is ~1.5 V (vs SHE) below the H_2O/H_2 redox level.[30] This suggests that water splitting is thermodynamically possible only when an additional bias voltage is provided, so that conduction band will have sufficient energy to transfer electrons for water reduction. We show that by utilizing OH^-/H^+ dual-ion energy, the electrical energy required for PEC water splitting can be brought down significantly. In the conventional symmetric ion configuration, the electrical energy required for PEC water splitting is ~1.8 V to achieve a current density of 10 mA/cm^2 and for achieving the same rate, OH^-/H^+ dual-ion assisted device required only ~0.95 V which is ~50 % lower. Energy of neutralization using OH^-/H^+ dual ion configuration nowadays has been widely used for improving the performance of several electrochemical devices like

supercapacitors, batteries, fuel cells, water electrolyser etc.[31-34] This work show for the first time how the hidden energy of OH^{-}/H^{+} dual-ion can be efficiently tapped for the electricity effective PEC water splitting using semiconductor electrodes.

2. Materials and methods

2.1. Chemicals

Ferrous sulphate, ascorbic acid (99%), amidosulfonic acid, boric acid (99.5%), potassium hydroxide (KOH), and sulphuric acid (H_2SO_4) were acquired from Sigma-Aldrich India. Nafion117 membrane was obtained from Fuel Cell Store, USA.

2.2. Experimental Procedure

α-Fe_2O_3 is electrodeposited on FTO plate. Prior to deposition, FTO strips were successively cleaned by ultrasonic degreasing in acetone, ethanol and deionized water (each for 10 min) and subsequently dried using an N_2 stream. The electrolyte consisted of 6 g ferrous sulphate, 0.15 g ascorbic acid, 0.05 g amidosulfonic acid and 1.5 g boric acid in 0.1 L deionized water. After electrodeposition for 10 min at 1.5 V vs Ag/AgCl/Cl^{-} reference electrode, the electrodeposited FTO is annealed in a furnace at 450ºC for 6 hours, which is the used as the photo anode. The morphology of the samples was observed by field emission scanning electron microscope (FESEM Zeiss UltraPlus) and transmission electron microscope (TEM, JEOL JEM-2200FS operating at 220 kV). Powder XRD patterns were recorded in Bruker D8

Advanced X-ray diffractometer with CuKα radiation (1.54 A). Electrochemical studies were carried out with a Biologic electrochemical workstation (VMP 300, France) with α-Fe_2O_3 as the working electrode, Ag/AgCl/Cl^- as the reference electrode and Pt wire as the counter electrode with electrolytes having a range of pH from 0 to 14. Reflection mode UV-vis spectroscopy was carried out with SHIMADZU UV-VIS 300. The photoelectrochemical (PEC) water splitting studies were carried out in a two-compartment cell made of quartz window and the two half-cells were separated by a Nafion 117 membrane. The α-Fe_2O_3 semiconductor electrode was used for driving the oxygen evolution reaction in the alkaline half-cell and a Pt disc served as the counter electrode for driving the hydrogen evolution reaction in the acidic half-cell.

3. Results and discussion

The OH^-/H^+ dual-ion assisted photo electrochemical cell was prepared by using a quartz cell as shown in Scheme 1. For the OH^-/H^+ dual ion energy assisted device, the anodic half-cell housed an alkaline solution at a pH 14 (KOH) and the cathodic half-cell housed an acidic electrolyte at a pH 0 (H_2SO_4) and the two half-cells were divided by a cation conducting Nafion 117 membrane. For a symmetric electrolytic cell without OH^-/H^+ dual-ion gradient, both the half-cells were filled with pH 14 solution. An electrical driving force was applied between a platinum (Pt) mesh electrode (housed in the acidic electrolyte) and a α-Fe_2O_3 film photoelectrode deposited on FTO substrate (housed in the

alkaline electrolyte) for photo electrochemical (PEC) water splitting. The cathodic half-cell was illuminated with a light source of 150 W at 1 Sun. In both the configurations, hydrogen evolution reaction (HER) should be the cathodic half-cell reaction and photo oxidation of water should be the anodic half-cell reaction.

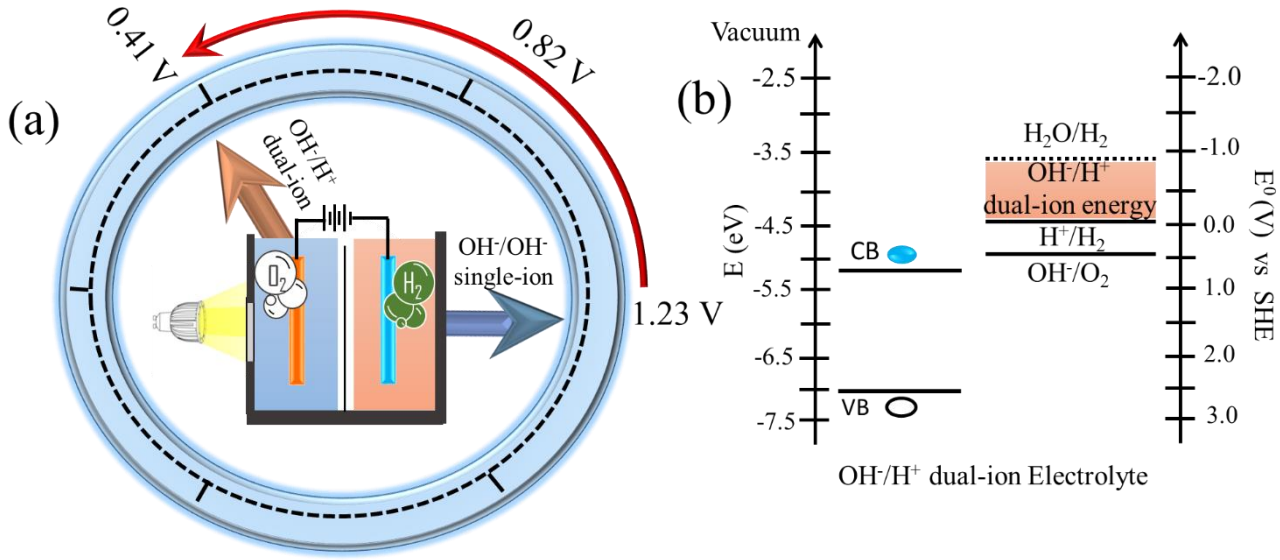

Scheme 1: (a) Schematic representation of OH-/H+ dual-ion energy assisted PEC water splitting device. (b) The corresponding band diagram of hematite electrode

Hematite was chosen as the semiconductor electrode to drive the photooxidation because of its suitable band gap (1.9 eV to 2.1 eV) for absorbing a wide range of the visible spectrum, chemical stability in a wide range of pH, nontoxicity and natural abundance.[23-26] Hematite electrode was deposited on FTO by electrodeposition from an iron

containing bath followed by annealing at 450°C for six hours as detailed in the experimental section.[35]

The as prepared α-Fe_2O_3 was characterized with X ray diffractometer (XRD) Figure 1a. The 2θ values were well matched with the JCPDS Card No. 00-005-0637 corresponding to α-Fe_2O_3 with the Miller indices at 24° (012), 33° (104), 36° (110), 41° (113), 49° (024), 54° (115), 58° (112), and 63° (214). The other peaks are due to substrate

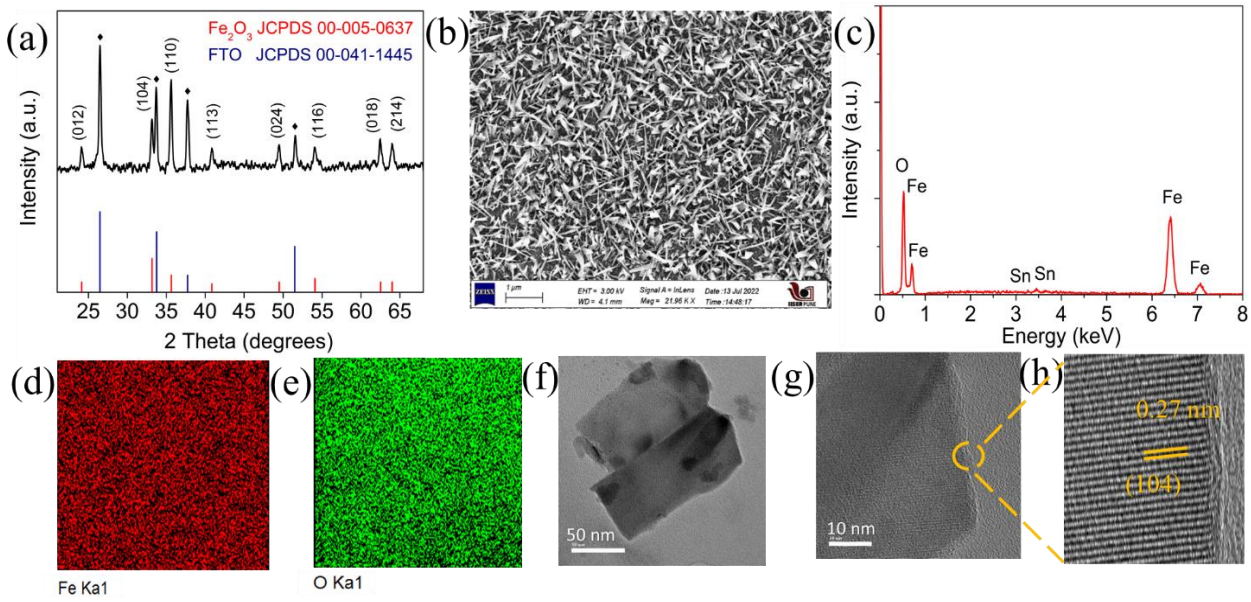

Figure 1: (a) X-Ray diffraction (XRD) of as-prepared α-Fe_2O_3 on FTO. (b) Scanning electron microscopy (SEM) image of as prepared α-Fe_2O_3. (c) Energy dispersive spectroscopy (EDS) of α-Fe_2O_3 layer on FTO. (d) and (e) corresponds to elemental mapping of iron (Fe) and oxygen (O). (f) Transmission electron microscopy (TEM) image of α-Fe_2O_3. (g) and (h) corresponds to high resolution TEM (HRTEM) images.

FTO on which α-Fe_2O_3 was deposited. The morphology of electrodeposited hematite was characterized by SEM, which showed needle like growth of α-Fe_2O_3 on FTO, Figure 1b. EDS shows the presence of iron and oxygen (Figure 1c), and the corresponding elemental mapping (Figure 1d, and 1e) shows uniform distribution of Fe and O in α-Fe_2O_3. TEM image shows the presence of typical lattice fringes of α-Fe_2O_3 with d-spacing of ~0.27 nm which corresponds to the intense (104) planes of α-Fe_2O_3.

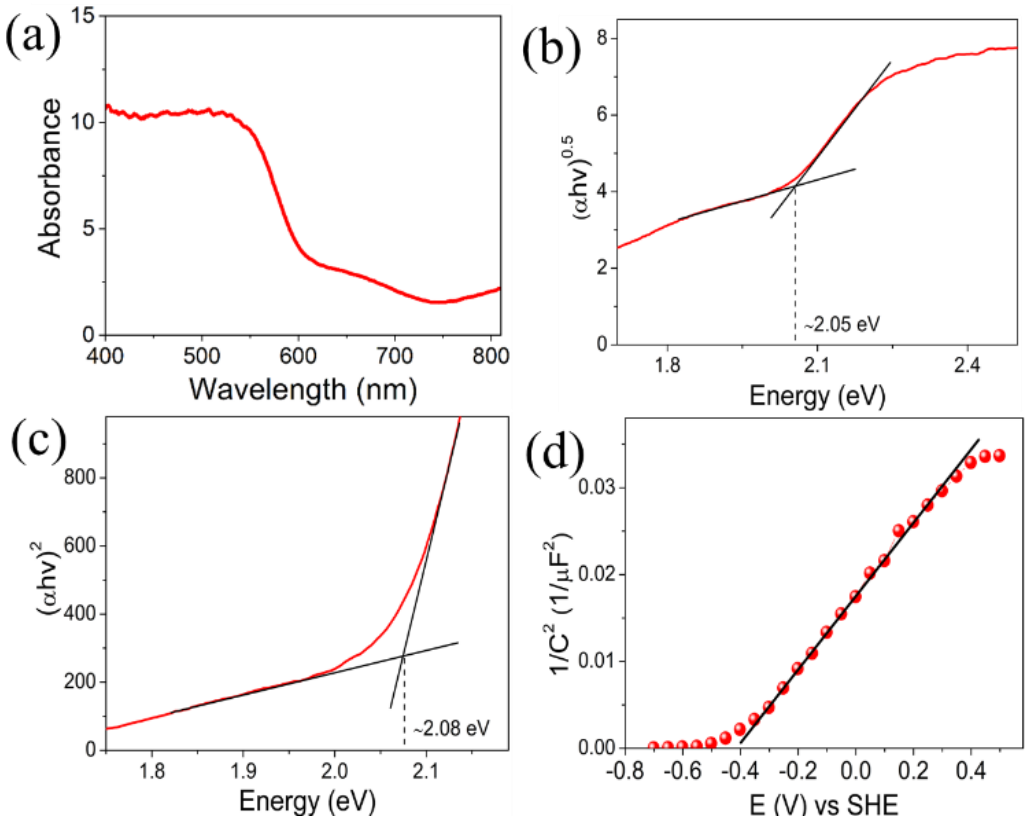

Figure 2: (a) Solid state UV-Vis spectroscopy of as prepared α-Fe_2O_3 on FTO. Tauc plots of α-Fe_2O_3 for showing (b) the indirect and (c) the direct bandgap. (d) Mott-Schottky plots of α-Fe_2O_3 electrode obtained in 0.1 M

NaOH electrolyte at 5 kHz AC frequency with a 10 mV AC amplitude (peak to peak).

The optical properties of as prepared α-Fe_2O_3 were characterized by solid state UV-Vis spectroscopy (Figure 2a) which showed a sharp increase of absorption below 600 nm. The optical band gap was determined by Tauc equation $(\alpha h\nu)^{1/n} = A\,(h\nu - E_g)$ where A is proportionality constant, h is Planck's constant, ν is the photon's frequency, E_g is energy of the optical band gap, and α is absorption coefficient. The value of the exponent represents the character of the electronic transition, for the direct band gap n is 0.5 and for the indirect band gap n is 2. Tauc plots in Figure 2b and 2c show an indirect band gap of nearly 2.05 eV and a direct bandgap of nearly 2.08 eV. All these suggest that α-Fe_2O_3 can absorb in the visible range of solar spectrum. Further, the Mott-Schottky analysis were performed to investigate the type of majority charge carrier. A.C. current with a frequency of 5 kHz and an amplitude of 10 mV were applied to the interface under the assumption that the overall capacitance of the semiconductor electrolyte interface is dominated by the space charge capacitance within the semiconductor. Figure 2c shows a positive slope in the Mott-Schottky plot which indicate that it is an n-type semiconductor, and the flat band potential is found to be -0.4 V vs SHE and the charge density is calculated from the slope of Mott-Schottky equation $\frac{1}{C^2} = \frac{2}{q\varepsilon\varepsilon^0 nA^2}\left(E - E_{fb} - \frac{kT}{e}\right)$, is found to be 7*$10^{16}$ cm^{-3}. All these suggest

that α-Fe_2O_3 has got a reasonably good charge carrier density and its band gap of ~2 eV is suitable to harvest visible range of the solar spectrum.

The free energy and potential plots associated with OH^-/H^+ dual-ion gradients depend on the pH deference of the two half-cells of OH^-/H^+ dual-ion gradient cell. As the ΔpH increases, the $\Delta G_{\text{Neutralization}}$ becomes more negative and E becomes more positive, Figure 1a. The open circuit voltage (OCV) of the OH^-/H^+ dual-ion gradient system is monitored with a Pt electrode as the counter and α-Fe_2O_3 photo electrode as the working electrodes in the presence and the absence of light, Figure 3b. The increase in OCV of α-Fe_2O_3 electrode on illumination signals the generation of photovoltage in both the configurations. The voltage difference on illumination is nearly 800 mV between the OH^-/H^+ dual-ion and OH^-/OH^- symmetrical ion cells, which decipher the presence of an in-built electric field of nearly 800 mV in the former which is commensurate to the energy of neutralization (Calculation 1). The counter reaction in PEC water splitting is hydrogen evolution reaction (HER) which is a pH-dependent electrochemical reaction. Linear sweep voltammetry demonstrated a negative voltage shift when the alkalinity of the electrolytic solution is gradually increased. The negative slope of nearly 60 mV/pH in the Pourbaix diagram suggests the involvement of equal number of protons and electrons, Figure 4b. Figure 4a and 4b also suggest that hydrogen evolution reaction occurs at a more negative

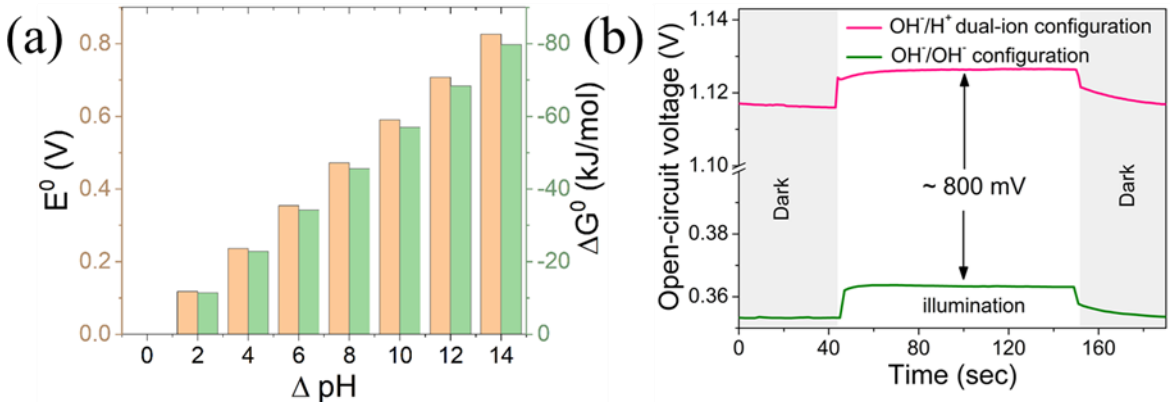

Figure 3: (a) Gibbs free energy change and potential plots with respect to pH gradients. (b) Open circuit voltage vs. time plots in OH^-/H^+ dual-ion gradient cell and OH^-/OH^- symmetric cell using Pt electrode as the counter and α-Fe_2O_3 as the working electrodes in the presence and the absence of light.

Calculation 1

OH^-/OH^- single-ion Electrolyte

Cathode electrode	$2H_2O + 2e^- \rightarrow H_2(g) + 4OH^-(aq)$	E^o = -0.82 V
Anode electrode	$4h^+ + 4OH^-(aq) \rightarrow O_2(g) + 2H_2O$	E^o = -0.41 V

$$4H_2O \rightarrow 2H_2(g) + O_2(g) \qquad E^o = -1.23\ V \qquad \ldots\ldots\ldots (1)$$

OH^-/H^+ dual-ion Electrolyte

Cathode electrode	$4H^+(aq) + 4e^- \rightarrow 2H_2(g)$	E^o = 0.0 V
Anode electrode	$4h^+ + 4OH^-(aq) \rightarrow O_2(g) + 2H_2O$	E^o = -0.41 V

$$4H^+(aq) + 4OH^-(aq) \rightarrow 2H_2(g) + O_2(g) + 2H_2O(l) \quad E^o = -0.41\ V \quad ...(2)$$

Equation (2) - Equation (1)

$$4H^+(aq) + 4OH^-(aq) \rightarrow 2H_2(g) + O_2(g) + 2H_2O(l) \quad E^o = -0.41\ V$$

$$4H_2O \rightarrow 2H_2(g) + O_2(g) \quad E^o = -1.23\ V$$

$$4H^+(aq) + 4OH^-(aq) \rightarrow 2H_2O(l)$$

$$E^o = (-0.41\ V) - (-1.23\ V) = 0.82\ V \quad ...(3)$$

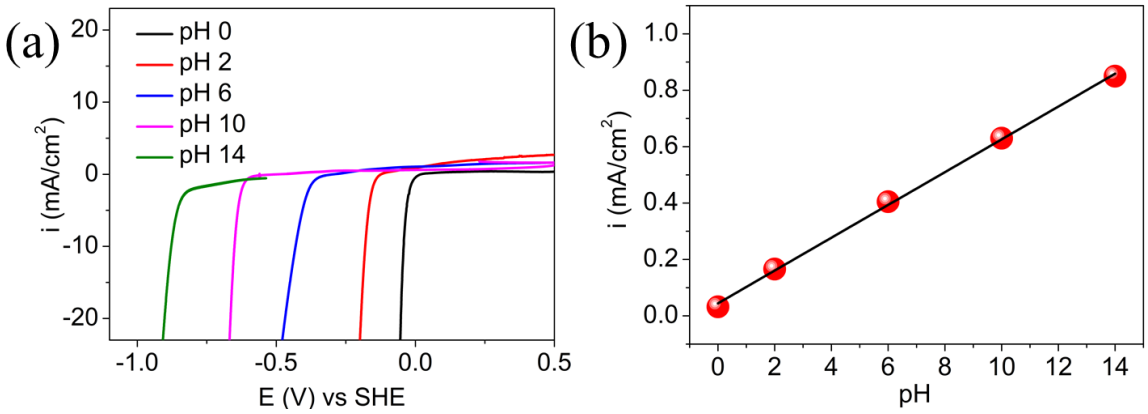

Figure 4: (a) Hydrogen evolution reaction (HER) in different pH solutions (pH 0 to pH 14). (b) Corresponding Pourbaix diagram for HER.

voltage in alkaline medium than in acidic medium. This justifies the choice of acidic medium for performing HER in the dual ion configuration. Figure 5a suggest that if HER is performed in pH 0 solution (as in OH^-/H^+ dual-ion configuration) instead of pH 14 solution, then the overall electrical potential for water splitting can be reduced from nearly 1.7 V to 0.9 V, indicating the advantages of OH^-

/H^+ dual ion gradient cell to make the process electricity effective. The photoelectrochemical response shows that for achieving a current density of 10 mA/cm^2, the required electrical driving force is 0.95 V for the OH^-/H^+ dual-ion configuration and the corresponding OH^-/OH^- symmetric ion cells required ~1.8 V for achieving the same rate, Figure 5b. At a fixed electrical driving force of 0.75 V, the photocurrent generated is 570 μA/cm^2 in case of OH^-/H^+ dual-ion cell which is nearly 10 times higher compared to OH^-/OH^- single ion configuration at that potential, Figure 5c.

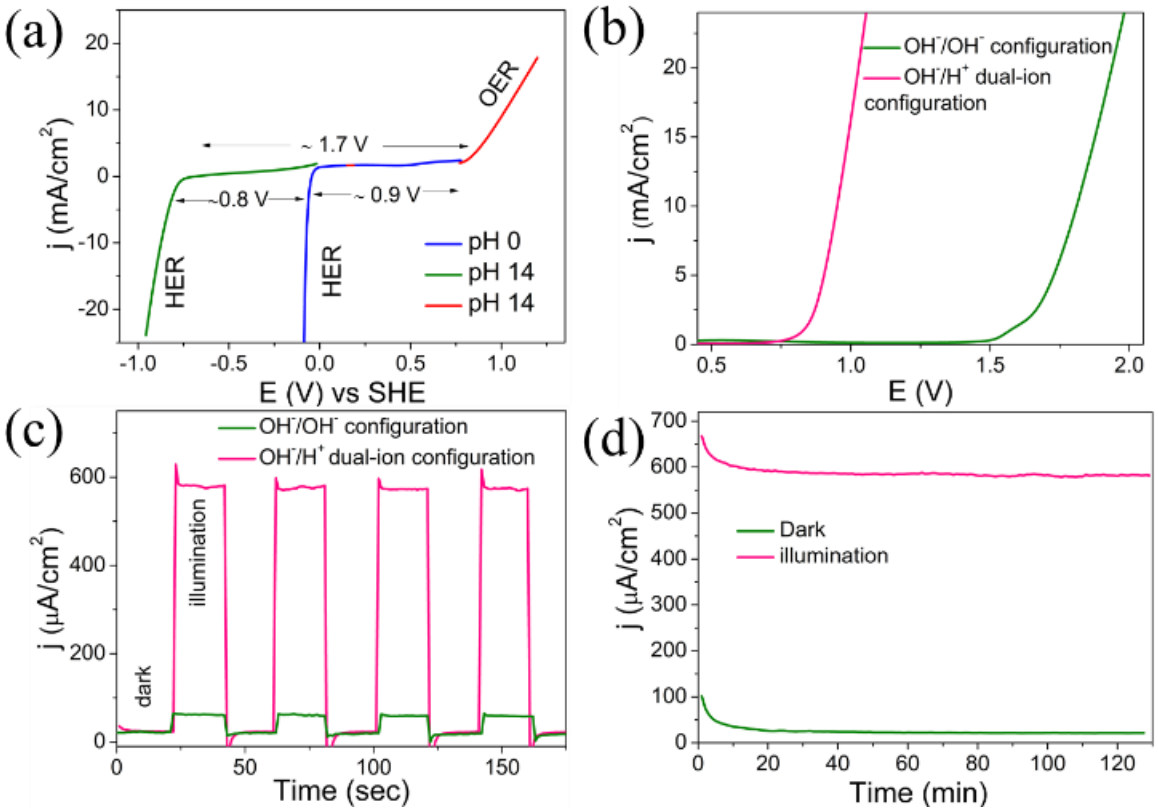

Figure 5: (a) Hydrogen evolution reaction (HER) in pH = 0 and pH = 14 electrolytes on a Pt electrode and oxygen evolution reaction (OER) on a α-Fe_2O_3 electrode in pH = 14 electrolytes. (b) Linear sweep voltammetry of α-Fe2O3 electrode in OH^-/H^+ dual-ion and OH^-/OH^-

configurations. (c) Transient photo-response in OH^-/H^+ dual-ion and OH^-/OH^- single ion configurations at 0.75 V and (d) stability of photocurrent in OH^-/H^+ dual-ion configuration at 0.75 V in the dark condition and on illumination.

Further, the steady state photocurrent in OH^-/H^+ dual-ion configuration at a fixed potential of 0.75 V is stable for 2 hours, Figure 5d. The change in pH in both compartment is monitored with time during photocurrent production and at and the pH changes were only marginal, Figure 6a. This could be due to the lower rate at which OH^- and H^+ ions are consumed at this relatively lower current of 570 $\mu A/cm^2$. The presence of oxygen in the anodic half-cell and the presence of hydrogen in the cathodic half-cell were further proved using in-situ electrochemical mass spectrometry, Figure 6b. Overall, the holes generated on the photoanode oxidised OH^- to oxygen at the semiconductor electrolyte interface, and on the counter electrode the electrons reduced the H^+ to hydrogen and in this process the overall electrical energy required for PEC water splitting got remarkably reduced due to the involvement of energy of neutralization as shown in equations 1 to 3.

Anodic Half-cell reaction

$$4h^+ + 4OH^-(aq) \rightarrow O_2(g) + 2H_2O \qquad E^o = -0.41\ V \quad ....(1)$$

Cathodic Half-cell reaction

$$4H^+(aq) + 4e^- \rightarrow 2H_2(g) \qquad E^o = 0.0\ V \quad .....(2)$$

$$4H^+(aq) + 4OH^-(aq) \rightarrow 2H_2(g) + O_2(g) + 2H_2O$$

$$E^o = -0.41\ V \quad .....(3)$$

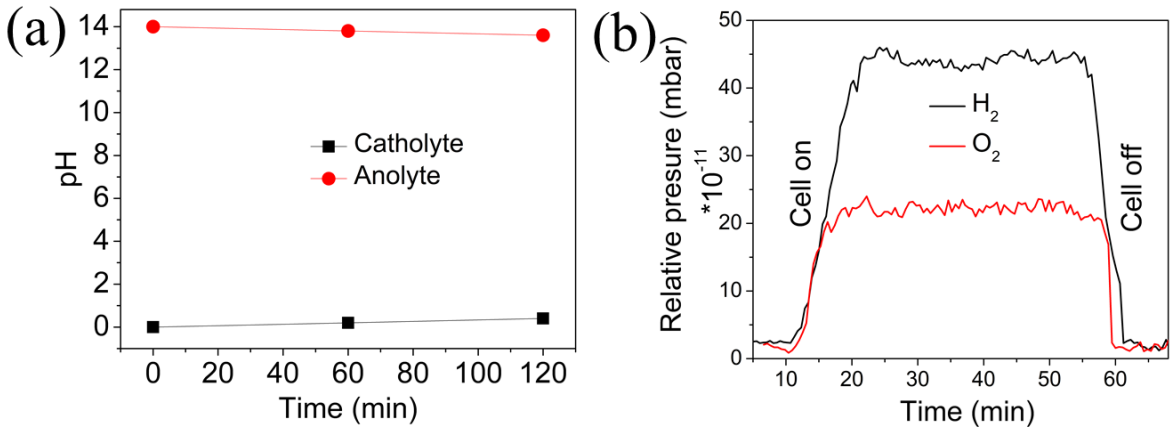

Figure 6: (a) pH change in the anodic and the cathodic half-cells during photo-current generation at 0.75 V for 2 hours. (b) In-situ electrochemical mass spectrometry showing the evolution of oxygen from the anodic half-cell and hydrogen from the cathodic half-cell during PEC water splitting.

4. Conclusion

We have demonstrated an electricity effective photo electrochemical water splitting in OH^-/H^+ dual-ion configuration which significantly lower the external electrical energy required for PEC water splitting by lowering the water reduction redox levels toward the conduction band of the semiconductor. This OH^-/H^+ dual ion energy assisted device demonstrated a photocurrent of ~570 $\mu A/cm^2$ at a remarkably low electrical bias of 0.75 V and the achieved rate is 10 times higher compared to a symmetric OH^-/OH^- single ion configuration at the same

applied bias. Further, the required electrical driving force for achieving a PEC water splitting current of 10 mA/cm^2 is 0.95 V in OH^-/H^+ dual-ion configuration which is only half that is required in an OH^-/OH^- symmetrical ion configuration.

5. References

[1] Maeda, K.; Domen, K. Photocatalytic Water Splitting: Recent Progress and Future Challenges. *J. Phys. Chem. Lett.* **2010**, *1*, 2655–26611.

[2] Sun, J.; Zhong, D. K.; Gamelin, D. R. Composite Photoanodes for Photoelectrochemical Solar Water Splitting. *Energy Environ. Sci.*, **2010**, *3*, 1252–1261.

[3] Kudo, A.; Miseki, Y.; Heterogeneous photocatalyst materials for water splitting. *Chem. Soc. Rev.*, **2009**, *38*, 253–278

[4] Dey, K. K.; Gahlawat, S.; Ingole, P. P; $BiVO_4$ optimized to nano-worm morphology for enhanced activity towards photoelectrochemical water splitting. *J. Mater. Chem. A,* **2019**, *7*, 21207-21221.

[5] Ye, S.; Ding, C.; Chen R.; Fan. F.; Fu. P.; Yin, H.; Wang, X.; Wang, Z.; Du, P.; Li C.; Mimicking the Key Functions of Photosystem II in Artificial Photosynthesis for Photoelectrocatalytic Water Splitting. *J. Am. Chem. Soc.* **2018**, *140*, 3250−3256.

[6] Yao, T.; An, X.; Han, H.; Chen, J. Q.; Li, C. Photoelectrocatalytic Materials for Solar Water Splitting. *Adv. Energy Mater.* **2018**, *8*, 1–36.

[7] Fujishima, A; Honda, K; Electrochemical Photolysis of Water at a Semiconductor Electrode *Nature* **1972**, *238*, 37–38.

[8] Wang, S; Chen, P; Yun, J; Hu, Y; Wang, L; Electrochemically-Treated $BiVO_4$ Photoanode for Efficient Photoelectrochemical Water Splitting. *Angew. Chem. Int. Ed.* **2017**, *56*, 8500–8504,

[9] Smith W.A.; Sharp D.I.; Strandwitzd N.C.; Bisquert J.; Interfacial band-edge energetics for solar fuels production: *Energy Environ. Sci.*, **2015**, *8*, 2851,

[10] Sivula, K., van de Krol, R. Semiconducting materials for photoelectrochemical energy conversion. *Nat. Rev. Mater*. **2016**, 15010.

[11] Smith,W.A.; Sharp,I.D.; StrandwitzdZ N. C.; Bisquert, J.; Interfacial band-edge energetics for solar fuels production. *Energy Environ. Sci.*, **2015**, *8*, 2851.

[12] Seger, B.; Tilley, S. D.; Pedersen, T.; Vesborg, P. C. K.; Hansen, O.; Gratzel, M.; Chorkendorff, Ib.: Silicon protected with atomic layer deposited TiO_2: conducting versus tunnelling through TiO_2; *J. Mater. Chem. A*, **2013**, *1*, 15089

[13] Laurence M. peter; Photoelectrochemistry: From Basic Principles to Photocatalysis. *Fundamentals and Perspectives*, **2016**, 1-28.

[14] Allen J. Bard; Photoelectrochemistry; *Science* **1980**, *207*, 139-144

[15] Mourad, E.; Coustan, L.; Lannelongue, P.; Zigah, D.; Mehdi, A.; Vioux, A.; Freunberger, S. A.; Favier, F.; Fontaine, O. Biredox Ionic Liquids with Solid-like Redox Density in the Liquid State for High-Energy Supercapacitors. Nature Materials **2016**, 16, 446–453.

[16] Kim J.Y, Magesh, G; Youn, D.H; Jang, J.W; Kubota, J; Domen. K; Lee. J. S; Single-crystalline, wormlike hematite photoanodes for efficient solar water splitting, *Sci. Rep. 2681*,1-8.

[17] Tayebi, M; Lee B.K.; Recent advances in $BiVO_4$ semiconductor materials for hydrogen production using photoelectrochemical water splitting; *Renew. Sustain. Energy Rev.* **2019**, *111*, 332-343.

[18] Khaselev O.; Turner J. A.; A monolithic photovoltaic-photoelectrochemical device for hydrogen production via water splitting; *Science* **1998**, *280*, 425-427.

[19] Anju, V. G.; Manjunatha, R.; Austeria, P. M.; Sampath, S. Primary and Rechargeable Zinc-Air Batteries Using Ceramic and Highly Stable TiCN as an Oxygen Reduction Reaction Electrocatalyst. *Journal of Materials Chemistry A* **2016**, *14*, 5258–5264.

[20] Jo, W.J.; Jang, J.W.; Kong, K.-j.; Kang, H.J.; Kim, J.Y.; Jun, H.; Parmar, K.; Lee, J.S. Phosphate doping into monoclinic $BiVO_4$ for enhanced photoelectrochemical water oxidation activity. *Angew. Chem.* **2012**, *124*, 3201–3205.

[21] Tacca.A.; Meda L.; Dr.; Marra, G.; Savoini, A.; Caramori, S.; Cristino. V.; Bignozzi,C.A.; Pedro,V.G.; Boix P.P.; Gimenez. S.;

Bisquert P.; Photoanodes Based on Nanostructured WO_3 for Water Splitting. *ChemPhysChem* **2012**, *13*, 3025 – 3034.

[22] Wang, G.; Wang, H.; Ling, Y.; Tang, Y.; Yang, X.; Fitzmorris, R.C.; Wang, C.; Zhang, J.Z.; Li, Y. Hydrogen-treated TiO_2 nanowire arrays for photoelectrochemical water splitting. *Nano Lett.* **2011**, *11*, 3026–3033.

[23] Makimizu Y.; Yoo. J., Poornajar, M.; Nguyen N. T.; Ahn, H.; Hwang I.; Kmentc S.; Schmuki P.; Effects of low oxygen annealing on the photoelectrochemical water splitting properties of a-Fe_2O_3, *J. Mater. Chem. A*, **2020**, *8*, 1315–1325.

[24] Mcdonald K.J.; Choi K.S.; Synthesis and photoelectrochemical properties of $Fe_2O_3/ZnFe_2O_4$ composite photoanodes for use in solar water oxidation. *Chem. Mater.* **2011**, *23*, 4863–4869.

[25] Makimizu Y.; Nguyen N. T.; Tucek, J.; Ahn H, Yoo J.; Poornajar, M.; Hwang, I.; Kment S.; Schmuki, P.; Activation of a-Fe_2O_3 for photoelectrochemical water splitting strongly enhanced by low temperature annealing in low oxygen containing ambient. *Chem. Eur. J.* **2020**, *26*, 2685 – 2692.

[26] Maiyalagan, T.; Alaje, T. O.; Scott, K. Highly Stable Pt À Ru Nanoparticles Supported on Three-Dimensional Cubic Ordered Mesoporous Carbon (Pt À Ru / CMK-8) as Promising Electrocatalysts for Methanol Oxidation. **2012**, 2630–2638.

[27] Das C.; Sinha N.; Roy P.; Transition Metal Non-Oxides as Electrocatalysts: Advantages and Challenges. *Small* **2022**, *18*, 1-61.

[28] Jun H.; Im B.; Kim, J. Y.; Im, Y., Jang, J.; Kim, E. S.; Kim, J. Y.; Kang, H. J., Hong S. J.; Lee J. S.; Photoelectrochemical water splitting over ordered honeycomb hematite electrodes stabilized by alumina shielding. *Energy Environ. Sci.*, **2012**, *5*, 6375–6382.

[29] Peter, L. M.; Wijayantha, K. G. U.; Tahir A. A.; Kinetics of light-driven oxygen evolution at α-Fe_2O_3 electrodes. *Faraday Discuss.*, **2012**, *155*, 309–322.

[30] Li, Y.; Liu, K.; Zhang, J.; Yang, J.; Huang, Y.; Tong, Y.; Engineering the Band-Edge of Fe2O3/ZnO Nanoplates via Separate Dual Cation Incorporation for Efficient Photocatalytic Performance: *Ind. Eng. Chem. Res.* **2020**, *59*, 18865–18872.

[31] Ding Y.; Cai P.; Wen Z.; Electrochemical neutralization energy: from concept to devices: *Chem. Soc. Rev.*, **2021**, *50*, 1495.

[32] Sur S.; Kottaichamy A. R.; Bhat Z. M.; Devendrachari M. C.; Thimmappa R.; Thotiy M. O.; A pH dependent high voltage aqueous supercapacitor with dual electrolytes. *Chem Phys Letts* **2018**, *712*, 160-164.

[33] Xu Y.; Cai P.; Chen K.; Ding Y.; Chen L.; Chen W.; Wen Z.; High-Voltage Rechargeable Alkali–Acid Zn–PbO_2 Hybrid Battery *Angew. Chem. Int. Ed.* **2020**, *59*, 23593–23597.

[34] Sur S.; Mondal R.; Thimmappa R.; Mukhopadhyay S.; Thotiyl M.O.; Aqueous OH^-/H^+ dual-ion gradient assisted electricity effective electro-organic synthesis of 2, 5-furandicarboxylic acid paired with hydrogen fuel generation. *J. Colloid Interface Sci. 630*, 477-483

[34] Sun F.; He D.; Yang K.; Qiu J.; Wang Z.; Hydrogen Production and Water Desalination with On-demand Electricity Output Enabled by Electrochemical Neutralization Chemistry. *Angew. Chem.Int. Ed.* **2022**, *61*, e202203929.

[35] Shinde P.S.; Go H.G.; Lee W.J.; Facile growth of hierarchical hematite (a-Fe2O3) nanopetals on FTO by pulse reverse electrodeposition for photoelectrochemical water splitting. *J. Mater. Chem.*, **2012**, *22*, 104.

Chapter 5

Aqueous OH^-/H^+ Dual-ion Gradient Assisted Electricity Effective Electro-Organic Synthesis Paired with Hydrogen Fuel Generation

Abstract

The OH^-/H^+ dual-ion gradient has a hidden electromotive force of 0.82 V under standard conditions; however, its non-redox nature completely prevents its direct interconversion as electrical driving force. We show by using organic molecules whose heterogeneous electron transfer is pH dependent, OH^-/H^+ dual-ion energy can be directly harvested as electrical driving force for performing simultaneous electro-organic synthesis and hydrogen fuel production in an electricity effective manner. To demonstrate this dual-ion gradient assisted electro-organic synthesis, 5-hydroxymethylfurfural (HMF) is chosen as the model molecule because of the immense techno commercial applications of its oxidized products. This dual-ion assisted device only required ~1 V to provide a current density of 50 mA/cm^2 and for achieving the same rate; the traditional state-of-the-art electrolytic cell required a doubling of the applied potential. The dual-ion gradient assisted device can convert biomass-derived HMF to economically important FDCA with ~90 % yield and ~87 % Faradaic efficiency with simultaneous H_2 fuel production at a potential as low as 1 V.

1. Introduction:

This Chapter discusses how OH^-/H^+ dual-ion gradient energy can be utilized for facile electro-organic synthesis. Environmentally friendly synthesis of fine reagents and chemicals is a challenge faced by chemists across the globe. [1–3] Electro-organic synthesis belongs to the class of green synthesis wherein electricity is used to drive complex organic reactions. [4–5] Due to minimal chemical waste generation in this technology, very high atom efficiency is often envisaged, and relatively affordable electricity is used as the oxidizer or reducer. [6–11] Moreover, if the source of electricity is renewable, a zero-carbon footprint can be achieved in organic synthesis. [12–13] Recently, coupling of oxidative electro-organic synthesis at the anode with reductive hydrogen evolution reaction at the cathode has emerged as an attractive strategy for the synthesis of value-added chemicals and hydrogen fuel generation. [14–16] Notably, this architecture for electro-organic synthesis still requires high input potential and we report how OH^-/H^+ dual-ion energy can be harvested for an electricity effective synthesis of value-added products and hydrogen fuel generation. Our thermodynamic calculation shows that nearly 0.82 V of hidden electrical energy can be available from OH^-/H^+ dual-ion gradients if the reaction is performed electrochemically. It should be noted that, OH^-/H^+ dual-ion energy is explored for a plethora of applications including urea oxidation, glucose oxidation, hydrazine fuel cell, desalination and much more [17-22]. To show that, the hidden electrical driving force

available with OH^-/H^+ dual-ion gradients can be harvested for electricity effective electrosynthesis, we have chosen 5-hydroxymethylfurfural (HMF) as the model molecule, as it is an important biomass-derived compound widely utilized as a precursor for the synthesis of various liquid fuels, fine chemicals and plastic. [23–27] HMF molecule typically contains one furan ring bearing one alcohol and one aldehyde group. Complete oxidation of HMF is a complex six-electron process as shown in Scheme 1. Various oxidative products of HMF oxidation include 2,5-diformylfuran (DFF), 5-hydroxymethyl-2-furancarboxylic acid (HMFCA), 5-formyl-2-furancarboxylic acid (FFCA) and 2,5-furandicarboxylic acid (FDCA) in a complex electrochemical pathway. [24, 28–31]

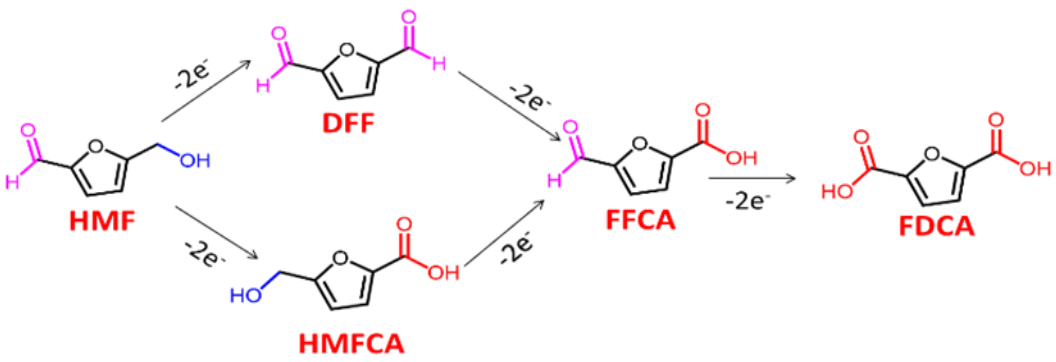

Scheme 1: Oxidative pathways of 5-hydroxymethylfurfural (HMF) to 2,5-furancarboxylic acid (FDCA).

Among these products, there is immense industrial interest in FDCA because of its potential to replace the petroleum-based terephthalic acid (PET) to synthesize renewable bio-based plastics. [32,33] In 1991,

Grabowski and co-workers reported electrochemical oxidation of HMF on Ni mesh, achieving an isolated yield of ~71% and a Faradaic efficiency of ~84% for FDCA production in pH 14 electrolytes. [34] After this seminal report, plethora of articles have appeared dealing with the design and engineering of various electrocatalysts like nanostructured Ni electrodes, Ni_2P, Ni_3S_2, NiFe layered double hydroxides etc. for HMF oxidation. [16,23,24] Notably, the primary aim of all these attempts were to lower the overpotential required for HMF electro-oxidation, [16,23,24] however, the required electrical driving force is still substantially higher to realize an electricity effective synthesis of FDCA. In this article, we show an electricity effective strategy for the electrochemical synthesis of FDCA during simultaneous hydrogen fuel production by employing the energy of OH^-/H^+ dual-ion gradient.

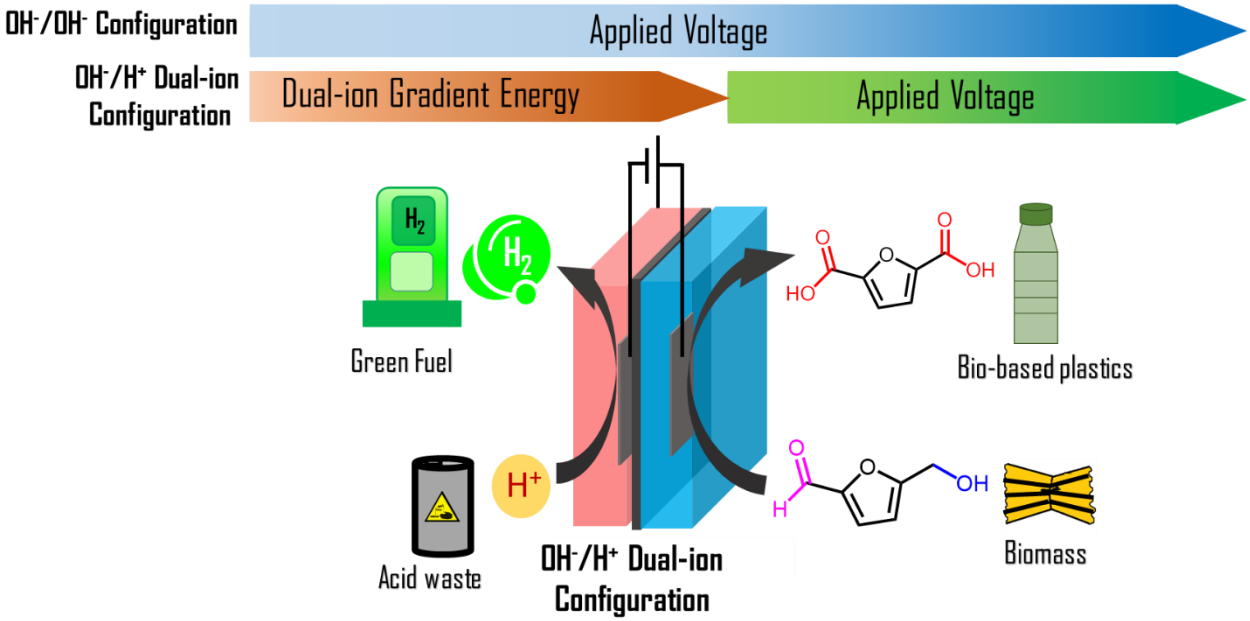

Scheme 2: Schematics of OH^-/H^+ dual-ion gradient assisted electro-organic synthesis of FDCA from biomass-derived HMF.

2. Materials and Methodologies:

2.1. Materials:

Potassium hydroxide (KOH), sulphuric acid (H_2SO_4), potassium phosphate dibasic (K_2HPO_4), potassium phosphate monobasic (KH_2PO_4), acetic acid (CH_3COOH), sodium acetate (CH_3COONa), potassium sulphate (K_2SO_4) and 5-hydroxymethylfurfural were used in the above experiments and these were acquired from Sigma-Aldrich India. Nafion 117 membrane was obtained from Fuel Cell Store, USA.

2.2. Experimental Procedure:

VMP 300 electrochemical workstation procured from Biologic, France was used to carry out all the electrochemical measurements. A three-electrode setup was used for carrying out the fundamental electrochemical transformations like HER and HMF oxidation. $Ag/AgCl/Cl^-$ electrode was used as the reference electrode, and a Pt disk was used as the counter electrode. A Pt (0.023 cm^2) and a Ni foam (1*1 cm^2) were used as working electrodes for HER and HMF oxidation respectively. Different pH solutions ranging from pH 0 (H_2SO_4), pH 4 (acetate buffer), pH 8, pH 12 (phosphate buffer) and pH 14 (KOH) were used for carrying out the pH dependent HER reaction. A two-compartment electrochemical cell was assembled to carry out the electro-organic synthesis wherein a Nafion 117 membrane was used for separating both the half-cells. H_2SO_4 solution (pH 0, 20 ml) and 10

mM HMF in KOH solution (pH 14, 20 ml) were used as catholyte and anolyte respectively. A Ni foam electrode (area: 4 cm^2) was used to drive HMF oxidation in the alkaline half-cell and a Pt electrodeposited Ti mesh (1.5 mg/cm^2) was used to carry out the HER in the acidic half-cell. The distance between two electrodes were ~1 cm and the process was carried out at room temperature (25°C) with continuous stirring at 30 rpm. ATR-FTIR spectra was acquired using Bruker Alpha II. A Bruker 400 MHz spectrometer was used for NMR analysis. High-resolution mass spectrometry (HRMS) was performed in WATERS Synapt G2 machine. UV-Vis spectroscopy was performed in SHIMADZU (UV-1900). A Hiden Analytical HR 40 was used to collect the in-situ electrochemical mass spectrometry data.

2.3. Statistical analysis:

All the measurements were performed five times each. Standard deviation (SD) is calculated by the following formula $\sigma(SD) = \sqrt{\sum_i \frac{(x_i - \overline{x})^2}{N-1}}$ where x_i are the values from the individual measurements, N is the total number of measurements and $\overline{x}$ is the mean value of the measurements. Error bars are included in the graphical plots. The error in each measurement is calculated by $\pm \frac{t\sigma}{\sqrt{N}}$, where t is the numerical factor for 95% confidence limit, which tends to $\sqrt{N}$ for N<10. So, every value is reported as $\overline{x} \pm \sigma$.

3. Results and Discussion:

The OH^-/H^+ dual-ion assisted organic synthesizer consists of an asymmetric electrolyte configuration as shown in Scheme 2. The anodic half-cell with a pH 14 electrolyte (KOH solution of HMF) is separated from the cathodic half-cell with a pH 0 electrolyte (H_2SO_4 solution) by a cation conducting Nafion 117 membrane.

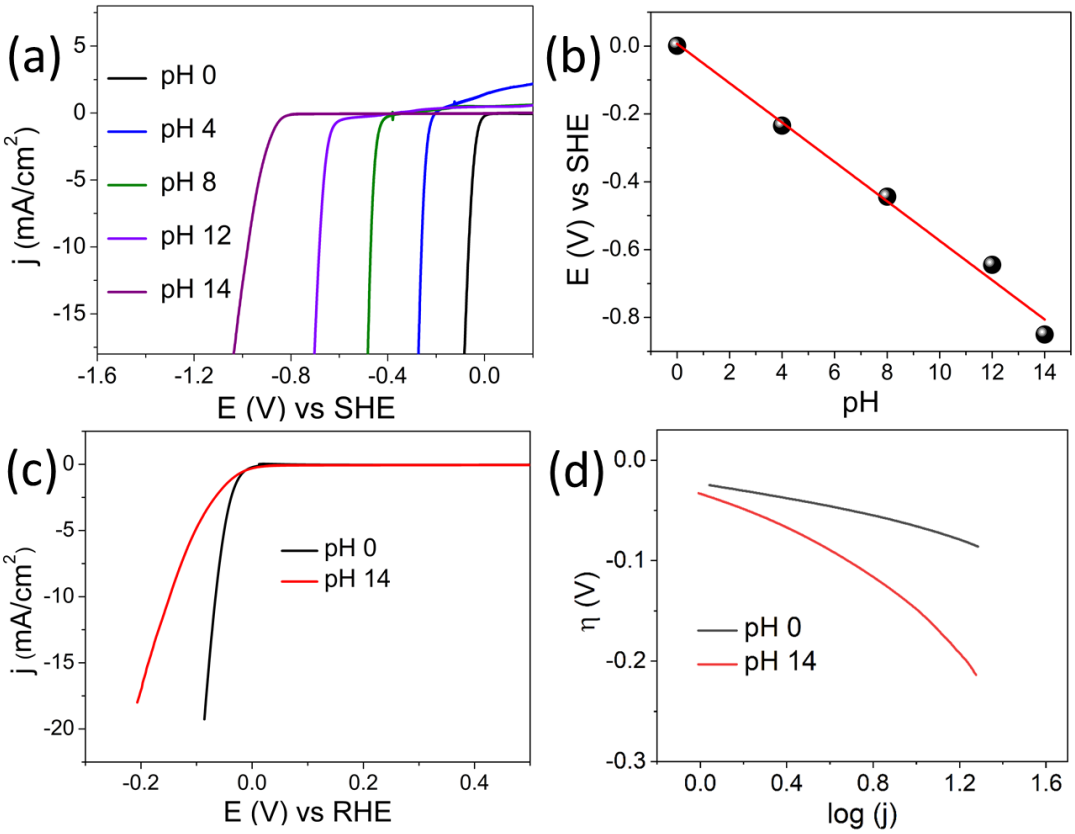

Figure. 1: (a) Hydrogen evolution reaction (HER) in different pH solutions (pH 0 to pH 14). (b) Corresponding Pourbaix diagram of HER. (c) Linear sweep voltammogram on Pt electrode in pH 0 and pH 14 solutions. (d) Corresponding Tafel plots for HER.

For a symmetric electrolytic cell without OH^-/H^+ gradient, both the compartments were filled with pH 14 solution (OH^-/OH^-). In the asymmetric configuration, an electrical driving force is applied between a platinum (Pt) mesh electrode (housed in the acidic electrolyte) and a nickel foam electrode (housed in the alkaline electrolyte) for hydrogen evolution reaction (HER) and HMF oxidationreaction respectively. In the dual-ion pH gradient configuration, hydrogen evolution reaction (HER) should be the cathodic half-cell reaction on the platinum based electrocatalyst in the absence of competitive electroactive species like O_2. Since HER is a pH-dependent electrochemical reaction, linear sweep voltammetry demonstrated a negative voltage shift when the alkalinity of the electrolytic solution is gradually increased, Figure 1a. The negative slope of ~60 mV/pH in the Pourbaix diagram suggests the equal number of protons and electrons are transferred in the electrochemical step as can be seen from Figure 1b. The activity for HER with the same platinum based electrocatalysts are found to be better in the acidic medium compared to the alkaline medium, Figure 1c, which is ascribed to the nature of the reacting species as it is well known to vary with the pH. [35] This is further supported by Tafel analysis in acidic and alkaline media wherein HER demonstrated a lower Tafel slope and a higher exchange current density in the former (Figure 1c, Figure 1d, and Table 1) indicating a favourable HER in the acidic medium.

Therefore, the free energy change of neutralization reaction ($\Delta G_{Neutralization}$) and the available electromotive force (E) depends on the OH^-/H^+ dual-ion gradient (ΔpH) of two electrolytes, Fig. 1a. As the

Table 1: Tafel slope for HER in acidic (pH=0) and alkaline (pH=14) medium on Pt.

	pH 0	pH 14
Tafel slope (mV/dec)	39	128

ΔpH increases, the $\Delta G_{Neutralization}$ becomes more negative, and E becomes more positive, Figure 2a. The anodic HMF oxidation reaction is probed in the half-cell mode on a Ni foam electrode in pH 14 solution which shows the onset of Ni (II) to NiOOH conversion starting at approximately 0.5 V vs SHE as shown in Figure 2b. [36] Ni was chosen for driving the HMF oxidation as it is known to catalyse the alcohol oxidation couple in mediating HMF oxidation is clear from the amplification of HMF oxidation current density after the introduction of HMF into the electrolyte, Figure 2b. [37,38] The electrochemical oxidation of HMF on Ni electrode is already established as shown in equations 1 to 3. [39,40] It is known that under open circuit condition, there is a thin layer of Ni $(OH)_2$ on the Ni electrode in the alkaline medium. [40–42] As per equations 1 to 3, the electrochemical oxidation of $Ni(OH)_2$ to NiOOH precedes the chemical oxidation of HMF. During this process NiOOH oxidises HMF thereby itself getting

reduced to $Ni(OH)_2$ making the electrochemical pathway a complex EC step. [41-45]

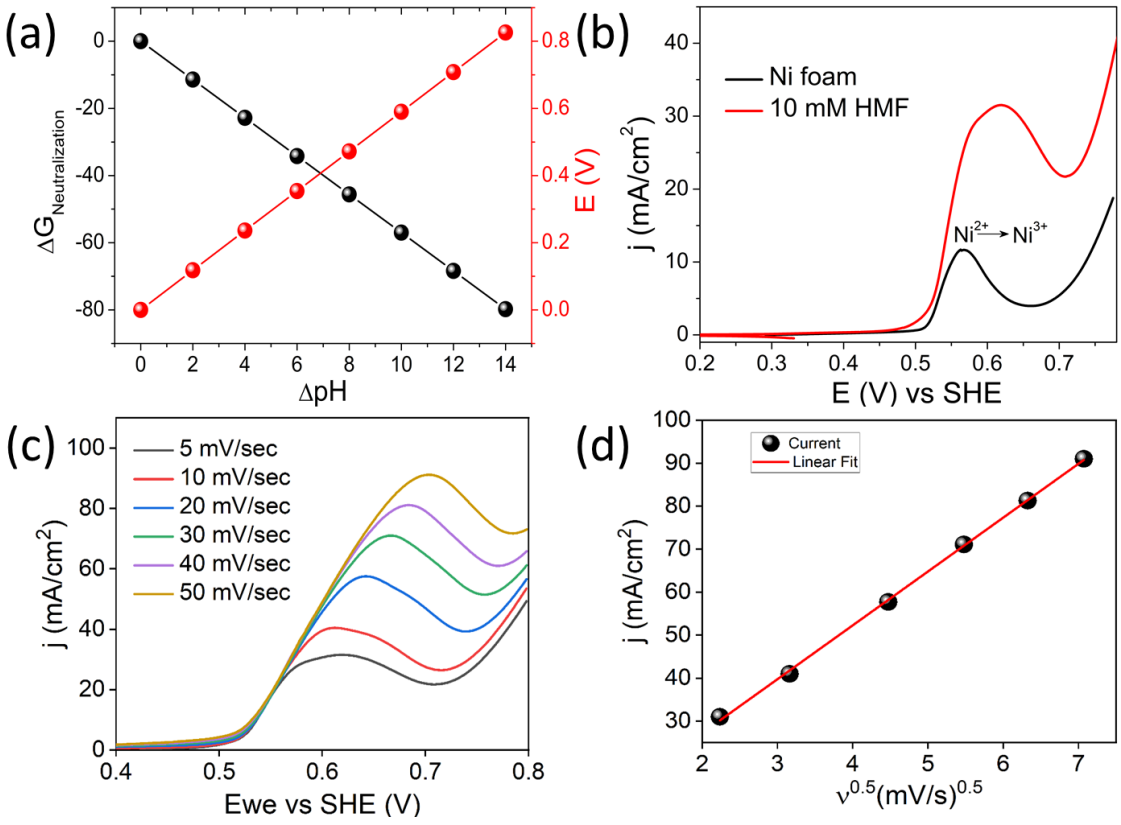

Figure 2: (a) Gibbs free energy change and potential plot with respect to OH^-/H^+ dual-ion gradients. (b) Linear sweep voltammogram (LSV) of a Ni foam electrode in pH 14 solution with and without HMF (10 mM) at 5 mV/sec scan rate. (c) Scan rate dependence plot of 10 mM HMF in pH 14 electrolyte on a Ni foam electrode and (d) the corresponding peak current density vs square root of scan rate.

$$OH^- + Ni(OH)_2 \leftrightarrow NiOOH + H_2O + e^- \quad (1)$$

$$R(CH_2OH) + 2NiOOH \leftrightarrow RCHO + 2Ni(OH)_2 \quad (2)$$

$$RCHO + 2NiOOH + H_2O \leftrightarrow RCOOH + 2Ni(OH)_2 \quad (3)$$

On the Ni foam electrode, the scan rate dependence study of HMF oxidation shows a linear increase in current with respect to square root of scan rate. This suggests that HMF oxidation on Ni foam electrode is a diffusion-controlled process at more positive potentials, Figure 2c, Figure 2d. Figure 3a suggests that, if HER is performed in acidic medium and HMF oxidation is performed in alkaline medium, the overall reaction will be assisted by OH^-/H^+ dual-ion gradient and the voltage required will be significantly lower than that required in a symmetric electrolyte configuration (OH^-/OH^-) without OH^-/H^+ dual-ion gradients (~0.5 V vs. ~1.3 V). The difference of ~0.8 V between the two systems is due to the involvement of OH^-/H^+ dual-ion gradient energy. To experimentally evaluate the contribution of electromotive force (EMF) derived from OH^-/H^+ dual-ion gradient, we have employed two identical Pt electrodes in asymmetric electrolytes with OH^-/H^+ dual-ion gradient as well as in symmetric electrolyte without pH gradient (OH^-/OH^-), Figure 3b.

Calculation 1

Symmetric Electrolyte (OH^-/OH^-)

Anodic Half: $HMF\,(aq) + 6OH^-\,(aq) \leftrightarrow FDCA\,(aq) + 4H_2O\,(l) + 6e^-$ $E^o = -0.65$ V

Cathodic Half: $6H_2O\,(l) + 6e^- \leftrightarrow 3H_2\,(g) + 6OH^-\,(aq)$ $E^o = -0.82$ V

$$HMF\,(aq) + 2H_2O\,(l) \leftrightarrow FDCA\,(aq) + 3H_2\,(g) \qquad E^o = -1.47 \text{ V} \ldots\ldots (1)$$

Asymmetric Electrolyte (OH^-/H^+)

Anodic Half: $HMF\ (aq) + 6OH^-\ (aq) \leftrightarrow FDCA\ (aq) + 4H_2O\ (l) + 6e^-$ $E^o = -0.65$ V

Cathodic Half: $6H^+\ (aq) + 6e^- \leftrightarrow 3H_2\ (g)$ $E^o = 0.0$ V

$HMF\ (aq) + 6OH^-\ (aq) + 6H^+\ (aq) \leftrightarrow FDCA\ (aq) + 3H_2\ (g) + 4H_2O\ (l)$ $E^o = -0.65$ V.....(2)

Equation (2) - Equation (1)

$HMF\ (aq) + 6OH^-\ (aq) + 6H^+\ (aq) \leftrightarrow FDCA\ (aq) + 3H_2\ (g) + 4H_2O\ (l)$ $E^o = -0.65$ V

$HMF\ (aq) + 2H_2O\ (l) \leftrightarrow FDCA\ (aq) + 3H_2\ (g)$ $E^o = -1.47$ V

$6H^+\ (aq) + 6OH^-\ (aq) \leftrightarrow 6H_2O\ (l)$ $E^o = 0.828$ V

Enthalpy changes during Neutralization

$\Delta H^0 = 6*H^0\ (H_2O) - 6*H^0(OH^-) - 6*H^0\ (H^+)$

$= 6*(285.83\ kJ) - 6*(-229.99\ kJ) - 6*0$

$= -\ 335.04\ kJ$

Entropy changes during Neutralization

$\Delta S^0 = 6*S^0\ (H_2O) - 6*S^0\ (OH^-) - 6*S^0\ (H^+)$

$= 6*\ (69.91) - 6*(-10.75) - 6*0$

$= 483.96\ JK^{-1}$

Free energy change during Neutralization

$\Delta G^0 = \Delta H^0 - T\Delta S^0$

$= -335.04\ kJ - (298\ K * 483.96\ JK^{-1})$

$= -479.26\ kJ$

$E^0 = -\Delta G^0/nF = \frac{-(-479.26)\ kJ}{6*96500\ C} = 0.82$ V

The EMF was ~0.8 V in asymmetric electrolyte with dual-ion pH gradients which is close to the thermodynamic potential for OH^-/H^+ reaction. This indicates that this energy of OH^-/H^+ reaction can be harvested as electromotive force in a pH gradient configuration to aid electro-organic synthesis. Current-Voltage curves for the asymmetric (OH^-/H^+) and symmetric (OH^-/OH^-) organic synthesizer show a lesser onset potential after the introduction of HMF molecules, which proves that HMF oxidation on the Ni electrode (Figure 4a,4b) precedes the oxygen evolution reaction (OER). Notably, the energy of OH^-/H^+ dual-ion gradient available in the asymmetric electrolyte configuration can be harvested for lowering the electrical driving force required for electro-organic synthesis, Figure 4c. The onset potential for asymmetric configuration with OH^-/H^+ dual-ion gradient starts nearly at 0.6 V whereas it is ~1.6 V for symmetric electrolyte configuration. To achieve the same current density of 50 mA/cm^2, an applied potential of nearly 1.0 V is required for asymmetric electrolyte configuration with OH^-/H^+ dual-ion gradient and in the traditional symmetric electrolyte configuration without OH^-/H^+ dual-ion gradient, the required voltage is nearly 2 V, Figure 4c. When electro-organic synthesis was performed at 1 V for both symmetric and asymmetric electrolyte configurations, Figure 4d, the

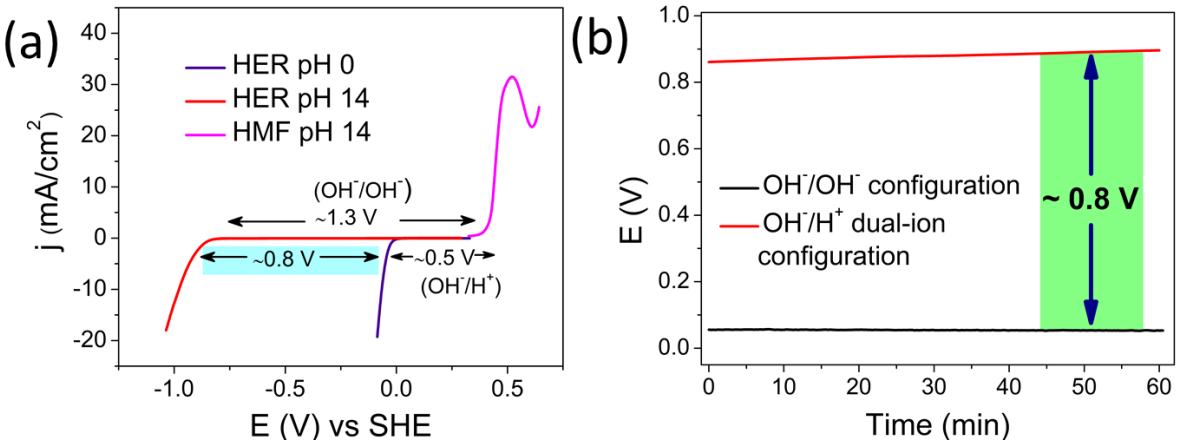

Figure 3: (a) LSVs for HER in pH 0 and pH 14 solution in comparison to LSVs for HMF oxidation reaction in pH 14 solution. (b) Open circuit voltage between two identical Pt electrodes in asymmetric OH^-/H^+ dual-ion configuration and symmetric OH^-/OH^- configuration for an hour.

current observed in the latter with OH^-/H^+ dual-ion gradient is substantially higher than that in the former. Apparently, in the asymmetric electrolyser with OH^-/H^+ dual-ion gradient, HMF oxidation is completed within an hour at 1 V which is why the current drifts to exclusive OER reaction after an hour of electrolysis, Figure 4d. The impedance analysis at 1 V in the frequency range of 100 kHz to 10 mHz shows that there is a significant drop in charge transfer resistance in the case of asymmetric electrolyte with OH^-/H^+ dual-ion gradients, Figure 5a. The impedance spectrum is fitted with equivalent circuit, where R_s represents the solution resistance, R_{ct} is charge transfer resistance of anode or cathode and Q is constant phase element

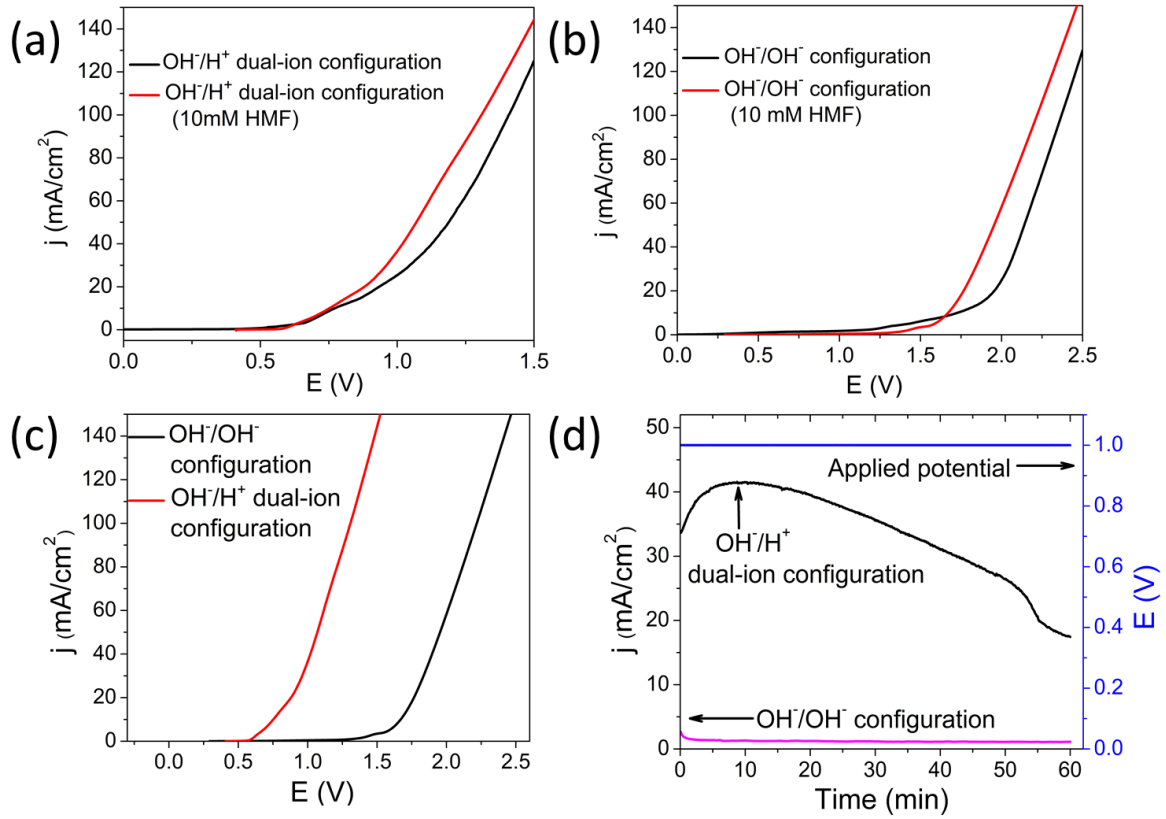

Figure 4: Linear sweep voltammogram in (a) OH^-/H^+ dual-ion configuration and (b) OH^-/OH^- configuration with and without 10 mM HMF at 5 mV/sec scan rate. (c) Current-Voltage curves for the OH^-/H^+ dual-ion asymmetric configuration and OH^-/OH^- symmetrical configuration. The anolyte is pH 14 electrolyte containing 10 mM HMF and catholyte is pH 0 electrolyte for the OH^-/H^+ dual-ion asymmetric configuration. (d) Chronoamperometry for symmetric (OH^-/OH^-) electro-organic synthesizer and asymmetric electro-organic synthesizer with OH^-/H^+ dual-ion gradient at 1 V driving force.

indicating double layer capacitance on the electrodes, Figure 6a. The fitting parameters are shown in Table 2. The gaseous species evolved in the cathodic half-cell is identified by in-situ electrochemical mass spectrometry, which shows the signal for hydrogen molecule, Figure

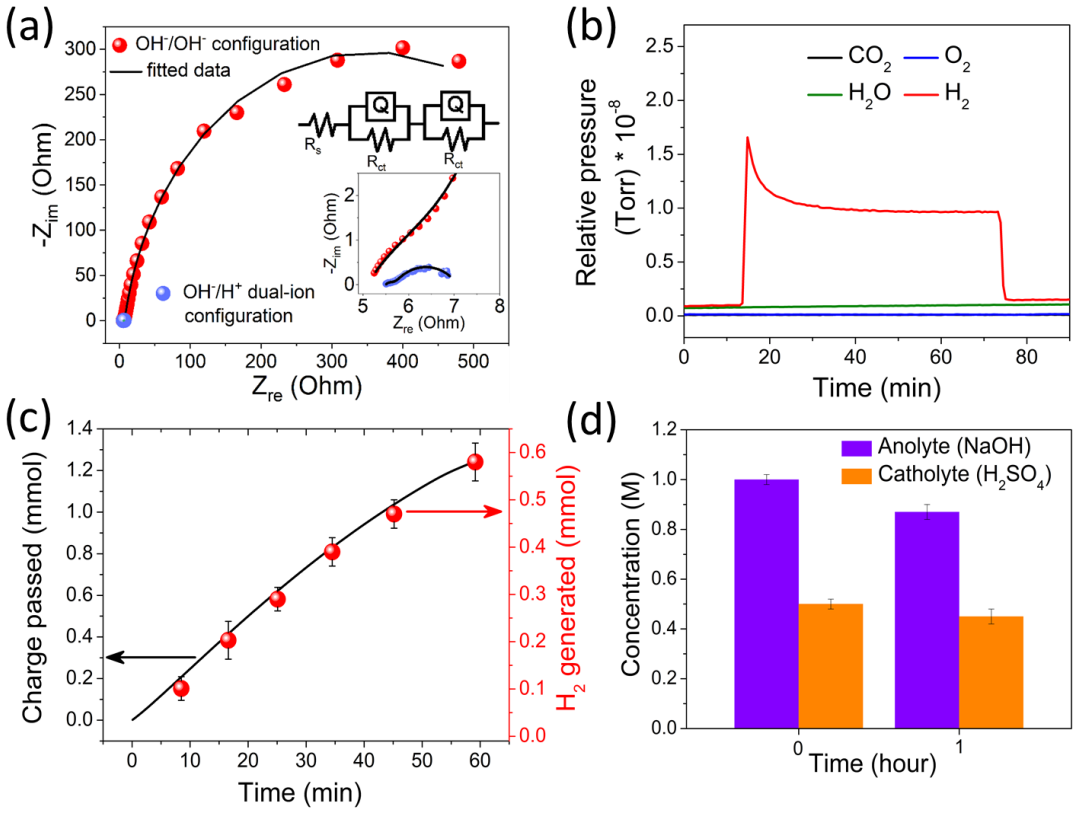

Figure 5: (a) Impedance spectra of symmetric cell and asymmetric cell at 1 V of applied potential in the AC frequency range of 100 kHz to 10 mHz with an AC excitation of 10 mV. Inset contain the equivalent circuit and zoomed high frequency region. (b) In-situ electrochemical mass spectrometry of evolved gaseous species in the cathodic half-cell of the OH^-/H^+ dual-ion gradient cell at a constant current density of 50 mA/cm^2. (c) Volume of H_2 generated in cathodic compartment and corresponding charge passed. For the OH^-/H^+ dual-ion asymmetric configuration, the anolyte is pH 14 electrolyte containing 10 mM HMF and catholyte is pH 0 electrolyte. (d) Changes in concentration of anolyte and catholyte during the electro-organic synthesis at an applied potential of 1 V.

Table 2: Fitting parameters of Impedance circuit.

	OH^-/H^+ dual-ion Electrolyte (Asymmetric)	OH^-/OH^- Electrolyte (Symmetric)
R_s	5.482	5.091
R_{ct}	1.183	2.639
Q (n = 1)	1.13	0.01227
Q (n = 0)	0.7348	0.8
R_{ct}	3.168	694.7
Q (n = 1)	0.2925	0.01564
Q (n = 0)	0.4368	0.8

5b. The hydrogen gas produced at the cathodic half-cell is quantified by the water displacement technique, which shows nearly 100 % Faradaic efficiency, Figure 5c. Although the current density decreases with the progress of the reaction (Figure. 4d), the total charge passed through the system is increasing with respect to time and hence the total amount of hydrogen produced is commensurate with the total charge passed, Figure 5c. In the OH^-/H^+ dual-ion gradient cell, the concentration changes of H^+ and OH^- in both half-cells were monitored,

which shows only a marginal change in concentration of H^+ and OH^- in both the half cells after an hour of electro-organic synthesis and the H_2 released at cathode is commensurate with the changes in concentration of H^+ ion in the cathodic half-cell, Figure 5d. However, when the cell is kept under idle conditions, the changes in concentration of H^+ and OH^- ions were negligible in both the half-cells for almost 30 hours, Figure 6a,b.

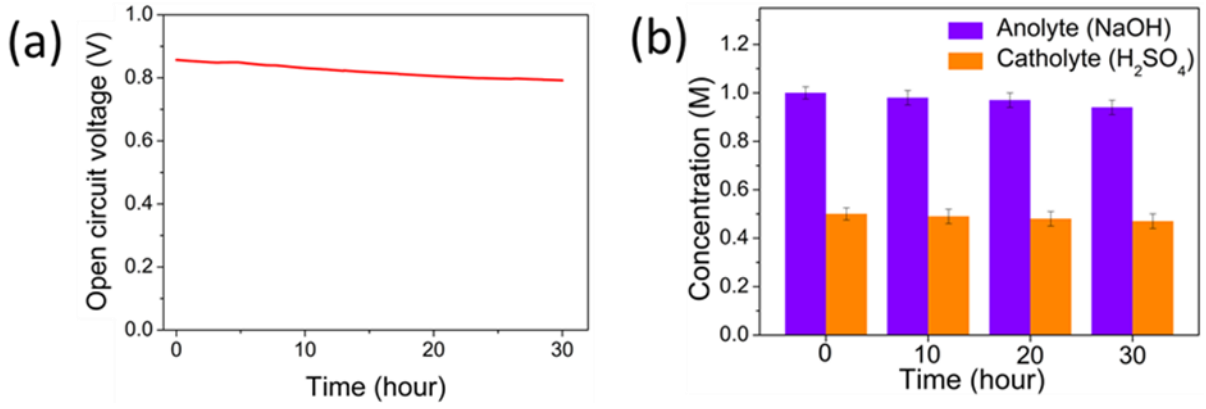

Figure 6: (a) Open circuit potential and (b) corresponding concentration changes in the anodic and the cathodic compartment as a function of time.

Thus, it is clear that OH^-/H^+ dual-ion acts as driving force in the overall reaction. The oxidized product in the anodic half-cell in the OH^-/H^+ dual-ion gradient cell is characterized by HRMS, ^{13}C-NMR, ^{1}H- NMR and FTIR spectroscopy. The HRMS spectrum in Figure 7 shows a single peak at 154.99 m/z ratio, which corresponds to the FDCA compound. FTIR spectra (Figure. 8a) shows the disappearance of the

broad O-H stretching peak in the range of 3200-3400 cm^{-1} (characteristics of HMF) in the product. [46] Secondly, a broad

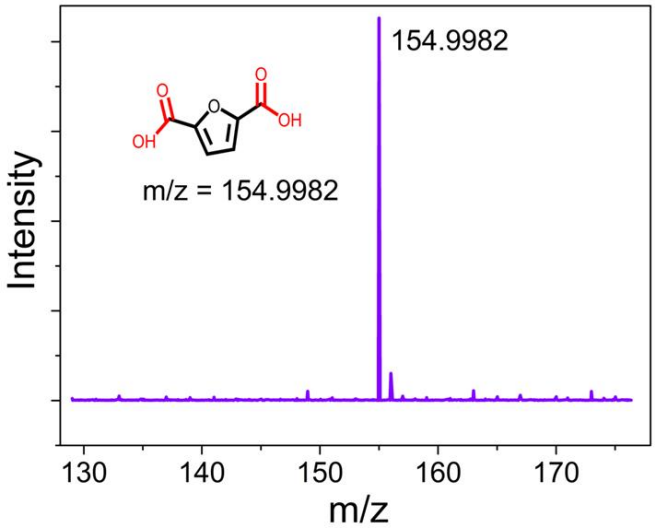

Figure 7: High Resolution Mass Spectra (HRMS) of the obtained product and the intense peak corresponds to FDCA.

carboxylic O-H stretching band appears by obscuring the C-H stretching in the region 3170 to 2350 cm^{-1} in the product, signaling the formation of FDCA. The ^{13}C-NMR spectrum (Figure 8b) of reactant shows peaks at (400 mHz (f1/ppm)) 178, 162, 152, 124, 110, and 56 ppm and product show the peaks at (400 mHz (f1/ppm)) 159, 147, and 118 ppm which clearly signal that HMF is converted to FDCA.The ^{1}H-NMR of the reactant (Figure 8c) shows the peaks at (400 mHz (f1/ppm)) 9.4(s, 1H), 7.4(d), 6.5(d), 5.5(t), 4.4(d)) and product shows a peak at (400 mHz (f1/ppm)): 7.25(d, 2H)) which further suggest that FDCA is the product after an hour of electrolysis. The peak corresponding to exchangeable acidic proton of carboxyl group was not observed in ^{1}H NMR probably due to trace amount of water present in the NMR solvent. After 1 hour of electrolysis, the colour of the anolyte

changes from light yellow to transparent, Figure 8d. All these are characteristics of FDCA suggesting its formation during electro-organic synthesis. Progress of the reaction is further monitored by ex-

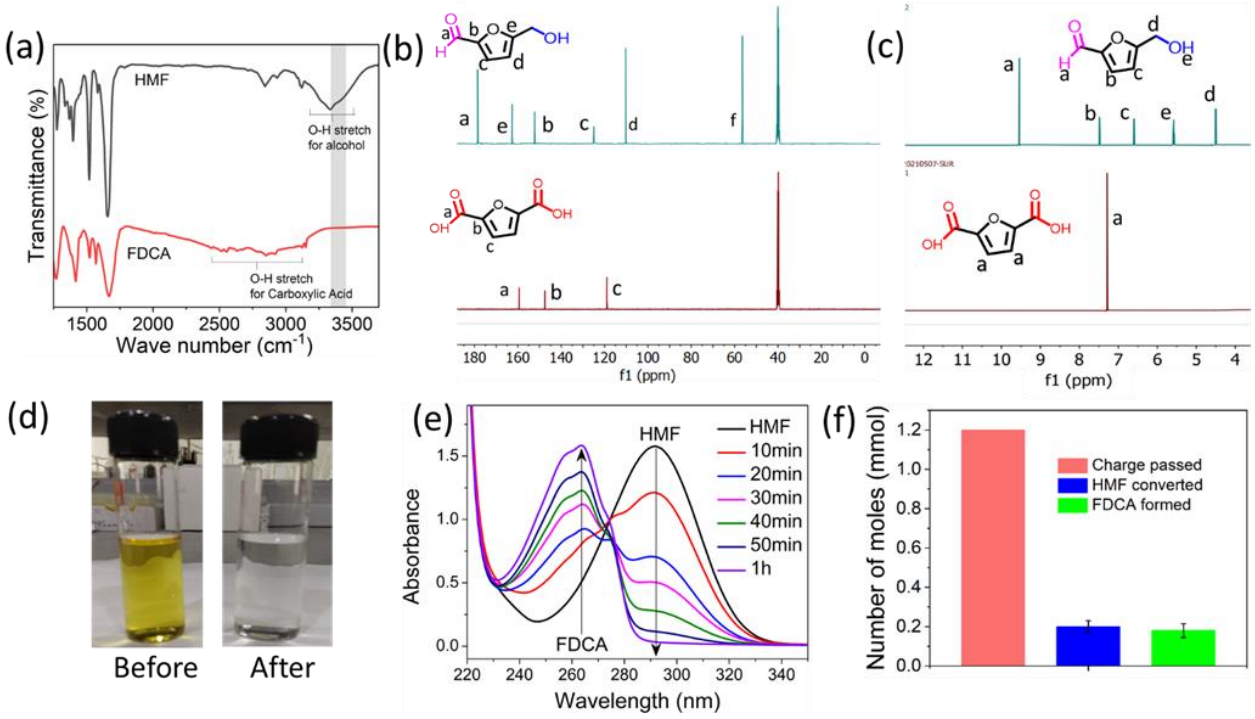

Figure 8: (a) FTIR spectrum of reactant (HMF) and product (FDCA). (b) 13C NMR spectra of the anolyte before and after one hour of electro-organic synthesis. (c) 1 H NMR spectra of the anolyte before and after one hour of electro-organic synthesis. (d) Photograph of anolyte before (yellow) and after (transparent) an hour of electrolysis. (e) Ex-situ UV– vis spectra of the anolyte with regular time interval during continuous electro-organic synthesis and (f) The amount of charge passed vs moles of HMF converted and moles of FDCA formed after one hour of HMF oxidation at a constant applied voltage of 1 V.

situ UV-VIS spectroscopy in the interval of 10 minutes, Figure 8e. It depicts a decrease in absorbance peak at ~294 nm (which corresponds to HMF) and an increase in absorbance peak at ~264 nm (which corresponds to FDCA). The final yield of FDCA was calculated by the absorption at 264 nm. Our asymmetric electrolyser with OH^-/H^+ dual-ion gradient shows a decent yield of 91 % (Figure 9a, b) within an hour at a remarkably low driving voltage of 1 V. Possible byproducts during HMF oxidation are 2,5-diformylfuran (DFF), 5-hydroxymethyl-2-furancarboxylic acid (HMFCA), 5-formyl-2-furancarboxylic acid (FFCA) etc.

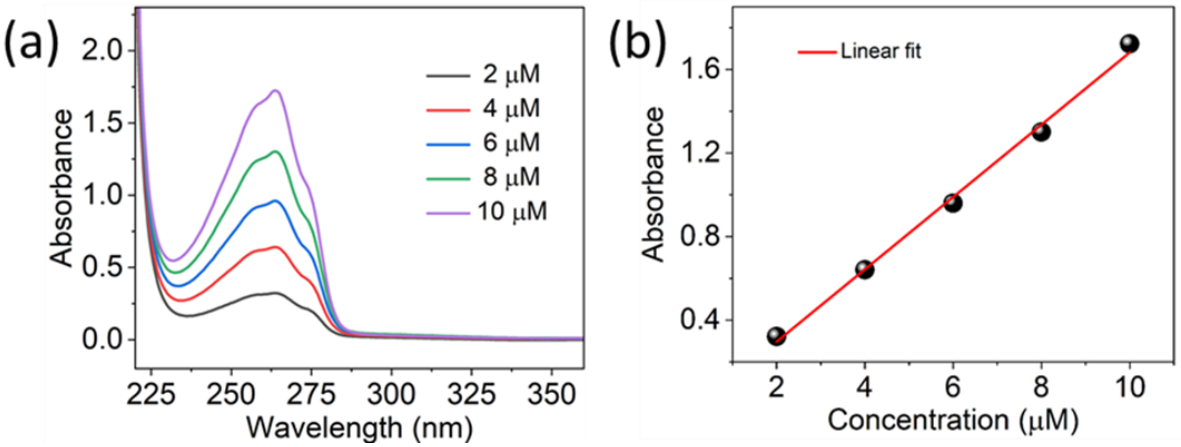

Figure 9: (a) UV-Vis spectra at various concentrations of FDCA and (b) the corresponding calibration plot.

Though these by-products formation are possible during the interconversion with OH^-/H^+ dual-ion assisted device, their concentrations were below the detection limit of the UV-Vis spectroscopy method, FTIR spectroscopy and NMR spectroscopy used

for product characterization. From the moles of FDCA formed (Fig. 3f) and the amount of charge passed (Fig. 2d) the Faradaic efficiency in the whole process was calculated, which is found to be nearly 87%, as demonstrated (Calculation 2). The slightly lower Faradaic efficiency is due to competing OER reaction during the HMF oxidation. Nevertheless, the strategy outlined here demonstrates that the energy available with OH^-/H^+ dual-ion gradient can be harvested for electricity effective electro-organic synthesis of complex reagents and chemicals during simultaneous hydrogen fuel generation.

Calculation 2

Yield calculation

$$\text{Product yield (\%)} = \frac{\text{moles of FDCA formed}}{\text{moles of HMF}} \times 100$$

$$\text{Product yield (\%)} = \frac{1.828 * 10^{-4}}{2 * 10^{-4}} \times 100$$

$$= 91.4\%$$

Faradaic efficiency calculation

$$\text{Faradaic efficiency (\%)} = \frac{\text{moles of FDCA formed}}{\text{equivalent charge passed}} \times 100$$

$$\text{Faradaic efficiency (\%)} = \frac{1.828*10^{-4}}{2.09*10^{-4}} \times 100$$

$$\text{Faradaic efficiency (\%)} = 87.4$$

4. Conclusions:

We have demonstrated how the hidden electromotive force due to OH^-/H^+ dual-ion gradient can be harvested for an electricity efficient electro-organic synthesis with simultaneous H_2 fuel production. This work helps to convert the biomass and acid waste to value-added products such as hydrogen fuel and FDCA in an electricity effective manner, which is an important step in the way towards achieving a sustainable energy network Assisted by OH^-/H^+ dual-ion gradient, FDCA could be synthesized with nearly 90 % yield and ~87 % Faradaic efficiency at an applied voltage as low as 1 V and for achieving the same rate, a conventional symmetrical cell required a doubling of applied potential.

5. References:

[1] Badalyan, A.; Stahl, S.S.; Cooperative electrocatalytic alcohol oxidation with electron-proton-transfer mediators, ***Nature.*** *2016*, **535,** 406–410.

[2] Wang, X.; Zhang, C.; Zhang, Z.; Gai, Y.; Li, Q.; Insights into the interfacial effects in Cu-Co/CeOx catalysts on hydrogenolysis of 5-hydroxymethylfurfural to biofuel 2,5-dimethylfuran, *Journal of Colloid and Interface Science.* **2022,** *615*, 19–29.

[3] Frontana-Uribe, B.A.; Little, R.D.; Ibanez, J.G.; Palma, A.; Vasquez-Medrano, R.; Organic electrosynthesis: A promising green methodology in organic chemistry, *Green Chem.* **2010,** *12*, 2099–2119.

[4] Wei, W.; Lyu, G.; Jiang, W.; Chen, Z.; Wu, S.; High-efficiency synthesis of 5-hydroxymethylfurfural and 2,5-diformylfuran from fructose over magnetic separable catalysts, *Journal of Colloid and Interface Science* **2021** *602*, 146–158.

[5] Delparish, A.; Uslu, A.; Cao, Y.; de Groot, T.; van der Schaaf, J.; Noël, T.; Fernanda Neira d'Angelo, M.; Boosting the valorization of biomass and green electrons to chemical building blocks: A study on the kinetics and mass transfer during the electrochemical conversion of HMF to FDCA in a microreactor, *Chem. Eng. J.* **2022,** *438*, 135393.

[6] Wiebe, A.; Gieshoff, T.; Möhle, S.; Rodrigo, E.; Zirbes, M.; Waldvogel, S.R.; Electrifying Organic Synthesis, *Angew. Chemie - Int. Ed.* **2018,** *57*, 5594–5619.

[7] Zhu, C.; Ang, N.W.J.; Meyer, T.H.; Qiu, Y.; Ackermann, L.; Organic Electrochemistry: Molecular Syntheses with Potential, *ACS Cent. Sci.* **2021**, *7*, 415–431.

[8] Bouchal, R.; Li, Z.; Bongu, C.; Le Vot, S.; Berthelot, R.; Rotenberg, B.; Favier, F.; Freunberger, S.A.; Salanne, M.; Fontaine, O.; Competitive Salt Precipitation/Dissolution During Free-Water Reduction in Water-in-Salt Electrolyte, *Angew. Chemie - Int. Ed.* **2020**, *59*, 15913–15917.

[9] Wazir, M.B.; Daud, M.; Safeer, S.; Almarzooqi, F.; Qurashi, A.; Review on 2D Molybdenum Diselenide (MoSe2) and Its Hybrids for

Green Hydrogen (H2) Generation Applications, *ACS Omega*, **2022**, *7*, 16856–16865.

[10] Jamshidi, M.; Nematollahi, D. Green Electrochemical Synthesis of N-Phenylquinoneimine Derivatives: Dual Action of 4-Morpholinoaniline and N-(4-Aminophenyl) Acetamide, *ACS Sustain. Chem. Eng.* **2017,** *5*, 9423–9430.

[11] Pollok, D.; Waldvogel, S.R.; Electro-organic synthesis-a 21st century technique, *Chem. Sci.* **2020**, *11*, 12386–12400.

[12] Rau, G.H.; Willauer, H.D.; Ren, Z.J.; The global potential for converting renewable electricity to negative-CO2-emissions hydrogen, *Nat. Clim. Chang.* **2018**, *8*, 621–625.

[13] Sgouridis, S.; Carbajales-Dale, M.; Csala, D.; Chiesa, M.; Bardi, U.; Comparative net energy analysis of renewable electricity and carbon capture and storage, *Nat. Energy*. **2019,** *4*, 456–465.

[14] You, B.; Liu, X.; Sun, Y.; Efficient H_2 Evolution Coupled with Oxidative Refining of Alcohols via A Hierarchically Porous Nickel Bifunctional Electrocatalyst, *ACS Catal*. **2017**, *7*, 4564–4570.

[15] Ding, Y.; Cai, P.; Wen, Z.; Electrochemical neutralization energy: From concept to devices, *Chem. Soc. Rev.* **2021**, *50*, 1495–1511.

[16] You, B.; Liu, X.; Jiang, N.; Sun, Y.; A General Strategy for Decoupled Hydrogen Production from Water Splitting by Integrating Oxidative Biomass Valorization, *J. Am. Chem. Soc.* **2016**, *138*, 13639–13646.

[17] Wang, G.; Chen, J.; Li, Y.; Jia, J.; Cai, P.; Wen, Z.; Energy-efficient electrolytic hydrogen production assisted by coupling urea oxidation with a pH-gradient concentration cell. *Chem. Commun*, **2018**, *54*, 2603-2606.

[18] Wang, G.; Wen, Z.; Self-supported bimetallic Ni–Co compound electrodes for urea- and neutralization energy-assisted electrolytic hydrogen. *Nanoscale*, **2018**, *10*, 21087–21095

[19] Zheng, D.; Li, J.; Ci, S.; Cai, P.; Ding, Y.; Zhang, M.; Wen, Z.; Three-birds-with-one-stone Electrolysis for Energy-efficiency Production of Gluconate and Hydrogen. *Appl. Catal. B*, **2020**, *277*, 119178-119204.

[20] Wang, G.; Chen, J.; Cai, P.; Jia, J.; Wen, Z.; A self-supported Ni–Co perselenide nanorod array as a high-activity bifunctional electrode for a hydrogen-producing hydrazine fuel cell. *J. Mater. Chem. A*, **2018**, *6*, 17763- 17770.

[21] Bhat, Z. M.; Pandit, D.; Ardo, S.; Thimmappa, R.; Kottaichamy, A. R.; Dargily, N. C.; Devendrachari, M. C.; Thotiyl, M. O.; An Electrochemical Neutralization Cell for Spontaneous Water Desalination. *Joule*, **2020**, *4*, 1730–1742.

[22] Sur, S.; Thimmappa, R.; Bhat, Z. M.; Dargily, N. C.; Mukhopadhyay, S.; Liu, X.; Cai, P.; Wen, Z.; Thotiyl, M. O.; Hybrid Alkali–Salt–Acid Electrochemical Device for Electricity-Efficient

Desalination and H2 Generation. *ACS Sustain. Chem. Eng.* **2022**, *10*, 10781–10788.

[23] Zhang, J.; Yu, P.; Zeng, G.; Bao, F.; Yuan, Y.; Huang, H.; Boosting HMF oxidation performance via decorating ultrathin nickel hydroxide nanosheets with amorphous copper hydroxide islands, *J. Mater. Chem. A.* **2021**, *9*, 9685–9691.

[24] Zhang, N.; Zou, Y.; Tao, L.; Chen, W.; Zhou, L.; Liu, Z.; Zhou, B.; Huang, G.; Lin, H.; Wang, S.; Electrochemical Oxidation of 5-Hydroxymethylfurfural on Nickel Nitride/Carbon Nanosheets: Reaction Pathway Determined by In Situ Sum Frequency Generation Vibrational Spectroscopy, *Angew. Chemie - Int. Ed.* **2019**, *58*, 15895–15903.

[25] Teong, S.P.; Yi, G.; Zhang, Y.; Hydroxymethylfurfural production from bioresources: Past, present and future, *Green Chem.* **2014**, *16*, 2015–2026.

[26] Sajid, M.; Zhao, X.; Liu, D.; Production of 2,5-furandicarboxylic acid (FDCA) from 5-hydroxymethylfurfural (HMF): Recent progress focusing on the chemical-catalytic routes, *Green Chem.* **2018**, *20*, 5427–5453.

[27] Motagamwala, A.H.; Won, W.; Sener, C.; Alonso, D.M.; Maravelias, C.T.; Dumesic, J.A.; Toward biomass-derived renewable plastics: Production of 2,5-furandicarboxylic acid from fructose, *Sci. Adv.* **2018**, *4*, 1–8.

[28] Lolli, A.; Maslova, V.; Bonincontro, D.; Basile, F.; Ortelli, S.; Albonetti, S.; Selective oxidation of HMF via catalytic and photocatalytic processes using metal-supported catalysts, *Molecules.* **2018**, *23*, 2792.

[29] Schlemmer, W.; Nothdurft, P.; Petzold, A.; Riess, G.; Frühwirt, P.; Schmallegger, M.; Gescheidt-Demner, G.; Fischer, R.; Freunberger, S.A.; Kern, W.; Spirk, S.; 2-Methoxyhydroquinone from Vanillin for Aqueous Redox-Flow Batteries, *Angew. Chemie.* **2020**, *132*, 23143–23146.

[30] Liu, W.J.; Dang, L.; Xu, Z.; Yu, H.Q.; Jin, S.; Huber, G.W.; Electrochemical oxidation of 5-hydroxymethylfurfural with NiFe layered double hydroxide (LDH) nanosheet catalysts, *ACS Catal.* **2018**, *8*, 5533–5541.

[31] Vuyyuru, K.R.; Strasser, P.; Oxidation of biomass derived 5-hydroxymethylfurfural using heterogeneous and electrochemical catalysis, *Catal. Today.* **2012**, *195*, 144–154.

[32] Cha, H.G.; Choi, K.S.; Combined biomass valorization and hydrogen production in a photoelectrochemical cell, *Nat. Chem.* **2015**, *7*,328–333.

[33] Taitt, B.J.; Nam, D.H.; Choi, K.S.; A Comparative Study of Nickel, Cobalt, and Iron Oxyhydroxide Anodes for the Electrochemical Oxidation of 5-Hydroxymethylfurfural to 2,5-Furandicarboxylic Acid, *ACS Catal.* **2019**, *9*, 660–670.

[34] Grabowski, G.; Lewkowski, J.; Skowroński, R.; The electrochemical oxidation of 5-hydroxymethylfurfural with the nickel oxide/hydroxide electrode, *Electrochim. Acta.* **1991**, *36*, 1995.

[35] Mansingh, S.; Das, K.K.; Parida, K.; HERs in an acidic medium over MoS2 nanosheets: From fundamentals to synthesis and the recent progress, *Sustain. Energy Fuels.* **2021**, *5*, 1952–1987.

[36] Kawashima, K.; Márquez-Montes, R.A.; Li, H.; Shin, K.; Cao, C.L.; Vo, K.M.; Son, Y.J.; Wygant, B.R.; Chunangad, A.; Youn, D.H.; Henkelman, G.; Ramos-Sánchez, V.H.; Mullins, C.B.; Electrochemical behavior of a Ni_3N OER precatalyst in Fe-purified alkaline media: The impact of self-oxidation and Fe incorporation, *Mater. Adv.* **2021**, *2*, 2299–2309.

[37] Bender, M.T.; Lam, Y.C.; Hammes-Schiffer, S.; Choi, K.S.; Unraveling Two Pathways for Electrochemical Alcohol and Aldehyde Oxidation on NiOOH, *J. Am. Chem. Soc.* **2020**, *142*, 21538–21547.

[38] Jud, W.; Salazar, C.A.; Imbrogno, J.; Verghese, J.; Guinness, S.M.; Desrosiers, J.; Kappe, C.O.; Cantillo, D.; Electrochemical Oxidation of Alcohols Using Nickel Oxide Hydroxide as Heterogeneous Electrocatalyst in Batch and Continuous Flow, *Org. Process Reasearch Dev.* **2022**, *26*, 1486-1495.

[39] Fleischmann, M.; Korinek, K.; Pletcher, D.; J. Chem. Soc., *Perkin Trans.* **1972**, *2*, 1396-1403.

[40] Trafela, Š.; Zavašnik, J.; Šturm, S.; Rožman, K.Ž.; Formation of a $Ni(OH)_2$/NiOOH active redox couple on nickel nanowires for formaldehyde detection in alkaline media, *Electrochim. Acta.* **2019**, *309*, 346–353.

[41] Latsuzbaia, R.; Bisselink, R.; Anastasopol, A.; van der Meer, H.; van Heck, R.; Yagüe, M.S.; Zijlstra, M.; Roelands, M.; Crockatt, M.; Goetheer, E.; Giling, E.; Continuous electrochemical oxidation of biomass derived 5-(hydroxymethyl) furfural into 2,5-furandicarboxylic acid, *J. Appl. Electrochem.* **2018**, *48*, 611–626.

[42] Guzman, R. S. S.; Vilche, J. R.; Arvia, A. J.; The potentiodynamic behaviour of Ni in KOH. *J. Of, A. Electrochemistry*, **1978**, *8*, 67–70.

[43] Boggs, B.K.; King, R.L.; Botte, G.G.; Urea electrolysis: Direct hydrogen production from urine, *Chem. Commun.* **2009**, 4859–4861.

[44] Fan, W.; Verrier, C.; Queneau, Y.; Popowycz, F.; 5-Hydroxymethylfurfural (HMF) in Organic Synthesis: A Review of its Recent Applications Towards Fine Chemicals, *Curr. Org. Synth.* **2019**, *16*, 583–614.

[45] Holzhäuser, F.J.; Janke, T.; Öztas, F.; Broicher, C.; Palkovits, R.; Electrocatalytic Oxidation of 5-Hydroxymethylfurfural into the Monomer 2,5-Furandicarboxylic Acid using Mesostructured Nickel Oxide, *Adv. Sustain. Syst.* **2020**, *4*, 2–6.

[46] Zhang, L.; Luo, X.; Qin, Y.; Li, Y.; A novel 2,5-furandicarboxylic acid-based bis (cyclic carbonate) for the synthesis of biobased non-isocyanate polyurethanes, *RSC Adv.* **2017**, *7*, 37–46.

Declaration: This work has been published in the following journal:

Journal of Colloid and Interface Science 630 (2023) 477–483

Chapter 6

Conclusion

In this thesis, the energy of classical neutralization reaction or OH^-/H^+ dual-ion gradient energy is utilized in an unconventional pathway to improve the performance metrics of state of the art electrochemical devices. To achieve this target, we have constructed an OH^-/H^+ dual-ion gradient electrolyte system, where direct acid alkali chemistry is chemically decoupled by an ion conducting membrane. The first part of the thesis report how this OH^-/H^+ dual-ion gradient energy can be harvested to enhance the voltage window of aqueous supercapacitors to nearly 2 V which is beyond the conventional limits of 1.23 V by arresting the parasitic water splitting reaction. This strategy improved the energy density of an aqueous supercapacitor nearly by 230 % without compromising its power capability. The second part of the thesis discusses how the OH^-/H^+ dual-ion gradient energy can be harvested to decrease the input potential required in electrolytic devices such as electrodilaysis cells, PEC water splitting device and electrochemicall cells for electroorganic synthesis. In Chapter 3, the OH^-/H^+ dual-ion gradient energy is efficiently tapped in electrodialysis cells for electricity effective desalination and the methodology offers potential practical applications to desalinate real saline solutions with negligible chances for water contamination. In Chapter 4, the hidden electromotive force of OH^-/H^+ dual-ion gradient is harnessed to decrease the external electrical bias required in photo electrochemical water splitting using hematite based photo anodes. As the conduction band of hematite electrode lies below the reduction potential of water reduction, a minimum electrical bias of 1.5 V is required to shift the conduction band above the water reduction level. This required potential can be decreased by nearly 50 % by harvesting the OH^-/H^+ dual-ion gradient energy. In Chapter 5, the OH^-/H^+ dual-ion gradient energy is employed to substantially lower the required electric potential

in electroorganic synthesis. By employing this strategy, HMF oxidation to value added products could be conducted at a voltage of nearly 1 V which is almost half of the electrical bias required in conventional electroorganic synthesis. mainly contribute to the overall required potential of the total electro organic synthesis. Taken together, OH^-/H^+ dual-ion gradient energy provides plethora of opportunities in the domain of electrochemistry wherein it can be employed to amplify the voltage output of galvanic devices and to decrease the voltage input in electrolytic devices. The work outlined in the thesis deciphers that introduction of OH^-/H^+ dual-ion gradient energy to electrochemical systems can also integrate additional functionality which is otherwise challenging with state of the art of electrochemical devices. It is to be noted that, OH^-/H^+ dual-ion gradient energy can be utilized to make low voltage water electrolyzer and high voltage fuel cells and a combination of both in a tandem configuration can lead to electrical efficiency greater than 1.

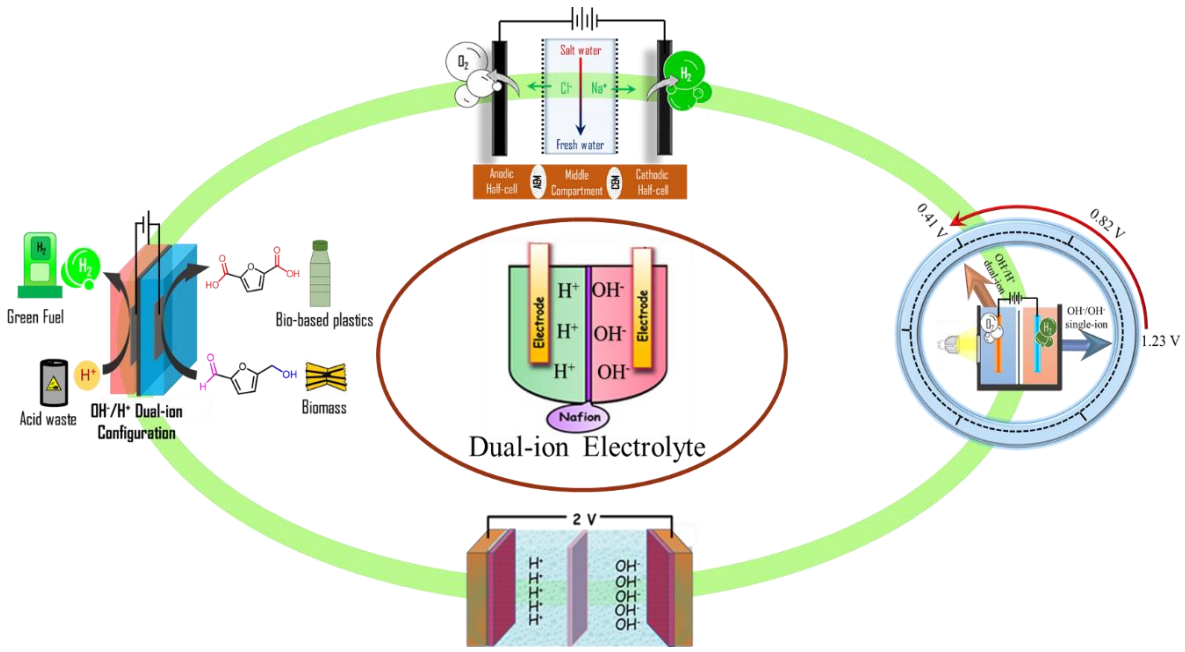

List of Publication

1. **Sur, S.;** Thimmappa, R.; Bhat, Z. M.; Dargily, N. C.; Mukhopadhyay S.; Cai, P.; Wen, Z*.; Thotiyl, M.O.* Hybrid Alkali−Salt−Acid Electrochemical Device for Electricity Efficient Desalination and H_2 Generation. **ACS Sustain. Chem. Eng**. **2022**, *10*, 10781–10788.

2. **Sur, S.;** Mondal R.; Thimmappa R.; Mukhopadhyay S.; Musthafa O.T. Aqueous OH^-/H^+ Dual-ion Gradient Assisted Electricity Effective Electro-Organic Synthesis of 2,5-Furandicarboxylic Acid Paired with Hydrogen Fuel Generation**. J. Colloid Interface Sci. 2022**, *630*, 477-483.

3. **Sur, S.**; Kottaichamy, A.K.; Bhat, Z.M.; Devendrachari, M.C.: Thimmappa, R.; Thotiyl, M.O.* A pH dependent high voltage aqueous supercapacitor with dual electrolytes. **Chem. Phys. Lett. 2018**, *712* 160–164.

4. **Sur, S.**; Mondal R.; Thotiyl M. O.; OH^-/H^+ Dual-ion Energy Assisted Electricity Effective Photoelectrochemical Water Splitting (Under Revision)

5. Dewan, A.: **Sur, S.**; Narayanan, R.; Thotiyl, M.O.* MOF-Derived Carbon Embedded NiO for an Alkaline Zn **ChemElectroChem, 2022**, *9*, 1-9.

A pH dependent high voltage aqueous supercapacitor with dual electrolytes

Author:
Soumodip Sur,Alagar Raja Kottaichamy,Zahid Manzoor Bhat,Mruthyunjayachari Chattanahalli Devendrachari,Ravikumar Thimmappa,Musthafa Ottakam Thotiyl

Publication: Chemical Physics Letters

Publisher: Elsevier

Date: 16 November 2018

Journal Author Rights

Please note that, as the author of this Elsevier article, you retain the right to include it in a thesis or dissertation, provided it is not published commercially. Permission is not required, but please ensure that you reference the journal as the original source. For more information on this and on your other retained rights, please visit: https://www.elsevier.com/about/our-business/policies/copyright#Author-rights

BACK CLOSE WINDOW

Hybrid Alkali–Salt–Acid Electrochemical Device for Electricity-Efficient Desalination and H2 Generation

Author: Soumodip Sur, Ravikumar Thimmappa, Zahid Manzoor Bhat, et al

Publication: ACS Sustainable Chemistry & Engineering

Publisher: American Chemical Society

Date: Aug 1, 2022

PERMISSION/LICENSE IS GRANTED FOR YOUR ORDER AT NO CHARGE

This type of permission/license, instead of the standard Terms and Conditions, is sent to you because no fee is being charged for your order. Please note the following:

- Permission is granted for your request in both print and electronic formats, and translations.
- If figures and/or tables were requested, they may be adapted or used in part.
- Please print this page for your records and send a copy of it to your publisher/graduate school.
- Appropriate credit for the requested material should be given as follows: "Reprinted (adapted) with permission from {COMPLETE REFERENCE CITATION}. Copyright {YEAR} American Chemical Society." Insert appropriate information in place of the capitalized words.
- One-time permission is granted only for the use specified in your RightsLink request. No additional uses are granted (such as derivative works or other editions). For any uses, please submit a new request.

If credit is given to another source for the material you requested from RightsLink, permission must be obtained from that source.

BACK CLOSE WINDOW

Aqueous OH−/H+ dual-ion gradient assisted electricity effective electro-organic synthesis of 2,5-furandicarboxylic acid paired with hydrogen fuel generation

Author: Soumodip Sur,Ritwik Mondal,Ravikumar Thimmappa,Sanchayita Mukhopadhyay,Musthafa Ottakam Thotiyl

Publication: Journal of Colloid and Interface Science

Publisher: Elsevier

Date: 15 January 2023

Journal Author Rights

Please note that, as the author of this Elsevier article, you retain the right to include it in a thesis or dissertation, provided it is not published commercially. Permission is not required, but please ensure that you reference the journal as the original source. For more information on this and on your other retained rights, please visit: https://www.elsevier.com/about/our-business/policies/copyright#Author-rights

BACK CLOSE WINDOW